NANOGAP BREAK JUNCTIONS AND SOLID-STATE MICROPORES AS ELECTRONIC BIOSENSORS

by

AZHAR ILYAS

Presented to the Faculty of the Graduate School of

The University of Texas at Arlington in Partial Fulfillment

of the Requirements

for the Degree of

DOCTOR OF PHILOSOPHY

THE UNIVERSITY OF TEXAS AT ARLINGTON

December 2013

ACKNOWLEDGEMENTS

I would never have been able to complete my dissertation without the guidance of my committee members, help from friends and support from my family members.

I would like to express my deepest gratitude to my advisor, Dr. Samir M. Iqbal, for his gracious mentorship, excellent guidance, tremendous motivation, and providing me with outstanding atmosphere for doing research. Without his encouraging words, thoughtful criticism, time and attention during busy semesters, this study would not have been possible. He always showed me by example and kept me motivated through his wisdom, knowledge and commitment to work. I am grateful to Dr. Young-tae Kim, Dr. Kytai T. Nguyen for helping me to develop my background in biology and providing guidance at different stages of my research projects. Special thanks to Dr. Donald Butler, and Dr. Robert Magnusson for reviewing my dissertation and being on my doctoral committee.

I would also like to thank my colleagues and friends Waseem Asghar, Yuan Wan, Arif Iftakher, Motasim Bellah, Ahmed Shahid, Muhymin Islam, Muhammad Raziul Hasan, Nuzhat Mansur, Waqas Ali, Chaudhary Amir Arafat, Wintana Kahsai, Uyen Pham, Joseph Billo, and Mohammud Noor for sharing their enthusiasm and thoughtful feedback on my research projects. I would also like to acknowledge the staff members at Nanotechnology Research and Education Center, and Characterization Center for Materials and Biology (C^2MB) for providing me technical help and trainings whenever needed.

Finally, I would like to thank my parents, brothers, sisters and my wife who always supported me and encouraged me with their best wishes. Above all, I am indebted to Allah Almighty for endowing me with health, patience and knowledge to complete this work.

November 07, 2013

ABSTRACT

NANOGAP BREAK JUNCTIONS AND

SOLID-STATE MICROPORES AS

ELECTRONIC BIOSENSORS

Azhar Ilyas, PhD

The University of Texas at Arlington, 2013

Supervising Professor: Samir M. Iqbal

Cancer has been the top ranked fatal disease for the last several decades. Most of the cancers remain silent at its earlier stage and are usually diagnosed at advanced and incurable phase. Early detection of cancer can have immediate and far reaching impact on better prognosis of cancer patients. Diseases are initially expressed at molecular and cellular scale and identification of these deadly diseases at such small scales would be a great step toward early detection. The study of biological molecules and diseased cells require efficient fabrication techniques to develop sensing devices with molecular size entrapment. Bio-nanotechnology and BioMEMs promise to fabricate devices not only down to the cellular scale but also down to the size of the biological molecules, such as proteins, bacteria and virus.

The overall goal of this research is to develop robust and highly sensitive electronic biosensors for identification of cancer at molecular and cellular level. The dissertation study focuses on 1) Development of nano-electrode break junction sensors for selective capture of Epidermal Growth Factor Receptor (EGFR) cancer biomarker 2) Development of solid-state micropore device for biomechanical discrimination of cancer cells from a biopsy sample 3) Development of multi-channel micropore sensor for efficient detection of Circulating Tumor

Cells (CTCs) from whole blood in a high throughput fashion 4) Synthesis of PLGA porous nanoparticles for controlled drug delivery systems. All of these solid-state biosensors were fabricated using standard silicon processing techniques. Surface functionalization was also performed to immobilize RNA aptamers on the surface. Break junctions with nanogap separation provide a platform for direct investigation of biological molecules in a simple and reliable manner. Solid-state micropores make use of biophysical properties of cells to indicate the physiological state of cells without using any cell staining. Multi-channel micropore device offers a novel approach for CTC detection from whole blood where parallel recognition of tumor cells makes it a rapid processing system. A novel approach to synthesize PLGA porous nanoparticles using water soluble salts as extractable porogen offers a simple and straightforward strategy to prepare porous nanoparticles. These biocompatible and biodegradable nanoparticles with porous surface topography can be used as efficient nanovehicles for controlled drug delivery systems.

TABLE OF CONTENTS

LIST OF ILLUSTRATIONS

Figure Page

LIST OF TABLES

Table Page

CHAPTER 1

INTRODUCTION

Nanotechnology has rapidly emerged among other fields of science and engineering. Evolution and development of this field over the last few years has convinced researchers and scientists that it can sustainably overturn the existing technical models. Miniaturization of the probes, ultrasensitive interfaces, characterization and prediction of the pathologic tendency of diseased cells are the essential enabling aspects of nanotechnology. Recent advancements in fabricating nanoscale devices and nano-object mediated modalities allowed nano-scale probing where detection and characterization of biological entities, their development and interactions, is carried out at molecular level. The state of the art in microfabrication and nanotechnology has facilitated us with instruments, techniques and skills to examine the presence or absence of a particular disease biomarker at molecular and cellular scale. Bio-nanotechnology broadly encircles cross-cutting research in engineering and biology. Much of current research focuses on the integration of biomedical engineering, nanoscience and nanotechnology, with particular focus towards their application in diverse areas like nanomanufacturing of break junctions for molecular diagnostics, chip-based recognition of cancer cells and site-specific controlled drug delivery systems.

1.1 Structure of Dissertation

The overall goal of this work is to develop simple but highly sensitive and reliable sensors for electronic detection of EGFR cancer biomarker, electrophysiological analysis of cancer cells for cancer diagnosis, rapid detection of circulating tumor cells (CTCs) and synthesis of porous PLGA nanoparticles from simple salts. This dissertation is divided into 7 chapters. The breakdown of chapters is given below:

1.1.1 Introduction (Chapter 1)

This chapter is meant to explain the significance of bio-nanotechnology in life sciences. It also intends to introduce the reader with the drive and objective behind the entire research work.

1.1.2 Background and Literature Review (Chapter 2)

Chapter 2 reviews the literature about the current methods to manufacture nanogap break junctions and its limitation, recent developments in molecular diagnostics, state of art in biopsy sample analysis and its downsides, current biosensors for cancer cell detection and their limitation, properties of circulating tumor cells (CTCs), conventional methods to synthesize porous nanoparticles and significance of porous particles in drug delivery systems.

1.1.3 Nanogap Break Junctions for Molecular Detection of Cancer (Chapter 3)

Break junctions have emerged as an important tool to investigate electrical transport properties of molecules. Selective probe molecules are immobilized between the contact structures with nanometer sized separation. Different process flows are employed for break junction manufacturing. All approaches either suffer from time consuming e-beam writing of the whole device or low yield that results from stochastic nature of electromigration process. We have deployed a new class of break junction fabrication using Focused ion beam (FIB) scratch followed by electromigration. The approach results into elegant, rapid and controlled high-yield nano-manufacturing of break junctions at exact locations with very narrow distribution of the gaps (between electrodes).

The break junctions are then employed as biological transducer to detect an important cancer biomarker Epidermal Growth Factor Receptor (EGFR). EGFR is a cell surface protein and its over-expression is recognized in several types of cancers. The silicon dioxide (SiO_2) surface between the nano-electrodes was functionalized with RNA aptamers which selectively bind to EGFR protein biomarker. The selectivity was demonstrated by the mutated non-

selective aptamers. The gold electrodes with nanometer sized separation give two orders of magnitude increase in current when selective capture of EGFR occurs. The surface chemistry for immobilization of RNA aptamers was verified by optical detection. Chapter 3 covers the fabrication process for nano-manufacturing of break junctions and explains the use of these nano-electrodes as an electronic sensor for molecular diagnostics.

1.1.4 Biomechanical Discrimination of Cancer Cells using Solid-state Micropores (Chapter 4)

Biomechanical properties (size, shape, stiffness, viscosity, deformability) of cells change significantly in unhealthy cells and can be used to indicate the physiological state of the cells. Cancer cells differ from normal cells in various aspects including size, shape, cellular functions and its biophysical properties. Although biopsy samples are the most valuable sources for cancer diagnosis but the analysis schemes are limited. High turnaround time, need for stains, lack of quantitative metrics and failure to recognize diseased cells when these are very few in number, are the major challenges in contemporary clinical pathology. We have developed a solid-state micropore sensor to discriminate cancer cells based on its biomechanical properties. The detection scheme utilized single solid-state micropore as the biological transducer which translated the cell's viscoelastic behavior into electrical signals. As a model, bladder cancer cells and normal urothelial cells were investigated. The approach didn't require any staining, functionalization or availability of any biomarkers but relied on merely cellular mechanical properties. Temporal measurements of the ionic current were recorded across the micropore. Cancer cells gave distinctive pulse signals while passing through the micropore and showed one order of magnitude faster translocation time as compared to normal cells due to their softer nature. The statistical analysis of each single cell present in the probed sample demonstrated its capability to identify cancerous cells when they were very few in number. Chapter 4 covers the micropore fabrication process, assembly of micropore sensor and its capability and potential to identify cancer cells using elasticity as the discrimination factor.

1.1.5 Parallel Recognition of Cancer Cells Using Micropore Array Assembly (Chapter 5)

Circulating tumor cells (CTCs) are thought to detach from the primary tumor, squeeze through the surrounding tissues and enter circulatory system. These cells spread through blood circulation to secondary tissues and accumulate to build up a secondary tumor. Early detection and accurate enumeration of CTCs in the peripheral blood is critically important to improve the survival rate of cancer patients. Several detection schemes have been employed for the isolation and quantification of CTCs but are mainly limited by low throughput or use of fluorescent tags for cell quantification. Modern electrical microfluidic systems offer label-free detection of pathogens but flow of cells in a single line makes it low throughput strategy. Similarly, single solid-state micropore device has to face high processing time for single cell analysis. We have developed a multi-channel micropore sensor that utilizes multiple micropores for parallel recognition of CTCs from blood sample. Red blood cells are lysed to reduce the cell concentration and increase the detection efficiency. Tumor cells are larger in size than leukocytes and give a characteristic pulse signal. The approach offers rapid processing of blood samples and efficient identification of cancer cells. Label free chip-based detection makes our device a simple and reliable detection system. Chapter 5 explains the device design, electrical measuring setup and CTC detection experiments.

1.1.6 Synthesis of Porous PLGA Nanoparticles for Drug Delivery Systems (Chapter 6)

Biodegradable micro/nanoparticles made of poly(lactic-co-glycolic acid) (PLGA) have emerged as promising drug delivery vehicles. These are widely used as carriers in controlled and targeted drug delivery applications. The controlled and targeted release coupled with therapeutic mechanisms significantly impacts the quality of the drug by eliminating the potential of both under and overdosing. PLGA based porous nanoparticles overtake the major challenges faced by nonporous particles like drug stability and accelerated polymer degradation due to autocatalytic effects. Moreover, pore characteristics have significant impact on drug release and

by controlling pore morphology, it is possible to design highly controlled drug release systems but synthesis of porous particles is relatively complex. We have developed leaching of water-soluble salts as a novel approach to synthesize porous PLGA nanoparticles. Bovine serum albumin (BSA) has been used as model drug and loaded into porous and non-porous nanoparticles. The physical characterization of porous and non-porous nanoparticles was performed to study the size distribution and colloidal stability. The *in vitro* drug release study was also carried out to observe the comparative release behavior over the same period of time. The porous nanoparticles showed an enhanced release of drug owing to the leaky features on the surface of nanoparticles which allowed easy release of drug. The release behavior can be optimized by simply varying the porosity which is a direct function of the porogen concentration. Chapter 6 covers the synthesis process of porous and nonporous PLGA nanoparticles and explains their drug release activities in details.

1.1.7 Future Research Directions (Chapter 7)

Chapter 7 covers the future directions and potential use of developed electronic biosensors. It also contains the scope of further work that could supplement/complement current work.

CHAPTER 2

BACKGROUND AND LITERATURE REVIEW

2.1 Break Junction Biosensors for Molecular Detection

2.1.1 Molecular Electronics

The ability to measure the electrical conductivity of a single molecule is highly significant in science and industrial communities and rooted the evolution of molecular electronics. Development of a realistic platform for direct investigation of biological species at molecular scale has always been of keen interest for researchers. Several approaches have been deployed for single molecule detection. Mainly these are categorized as lateral device structures (LDS) and vertical device structures (VDS). VDS involves a conductive substrate with molecular layer deposition on top of it whereas the conductive probe provides the second contact to make a metal-molecule-metal structure. Scanning tunneling microscopy (STM) was the first and foremost device of this kind and made a great impact in the field of molecular electronics. Figure 2.1 demonstrates a schematic sketch of STM used to study electron transport properties of molecules. An LDS contains a pair of metal contacts with nanometer-sized separation and probes selective to target molecules are immobilized between the contact structures. Devices of this kind that contain a thin metal strip, in which a nanoscale gap is produced by some technique, are known as break-junctions.

2.1.2 Break Junctions

Break junctions are composed of a pair of electrodes with nanometer sized separation (nanogap). Break-junctions have been used to study the electrical transport properties of single molecules entrapped in the nanoscale opening between the contact structures [1, 2]. The target

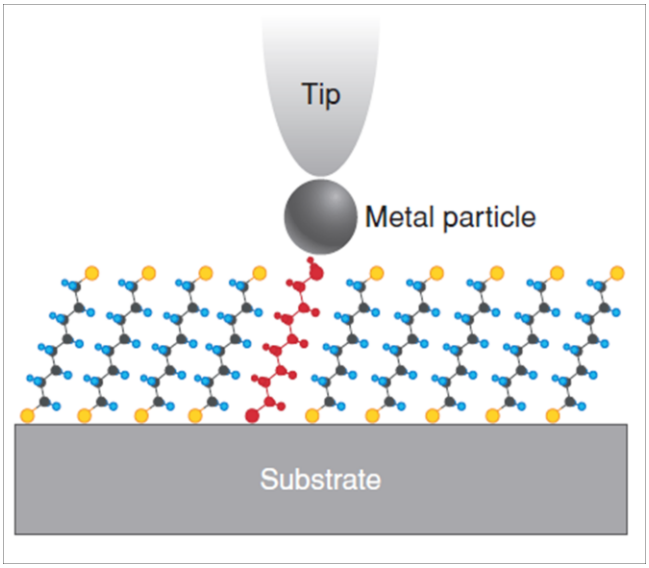

Figure 2.1 Scanning tunneling microscopy (STM) represents a vertical device structure to measure the conductance of molecule with one end attached to the metal substrate and other end with the conducting tip. Reprinted with permission [3], copyright (2007).

molecules are captured by the probes immobilized between the nano-electrodes. The break-junctions are fabricated by introducing a nanogap between two thin metal lines [4-6]. The nanoscale separation is the most important element of the break-junctions as this area is functionalized with probing molecules to get the target molecule attached at this site. Selective capture of the target molecule bridges the two electrodes and makes a metal-molecule-molecule structure. When a voltage is applied across the metal contacts, current starts flowing through the molecules bridging the gap between them as shown in Figure 2.2 [3]. The amplitude of the current is correlated to electrical conductivity of target molecules. Break junctions provide the simplest platform to study electron transport properties of single molecules but entail with efficient fabrication techniques.

Fabrication of metal electrodes with nanoscale gap has been a challenge and extensive efforts have been made to manufacture nanogap break junctions. Most of these techniques either involve the serial process of E-beam writing or mechanical fracture of already patterned

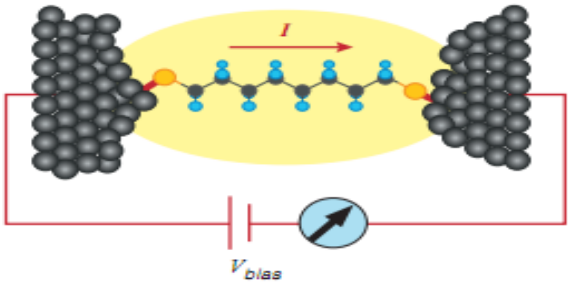

Figure 2.2 Schematic of nanoelectrodes to study electrical conductivity of molecule covalently attached to metal conatacts. Reprinted with permission [3], copyright (2007).

electrodes. E-beam writing gives high yield but serial process makes it a very low throughput technique. Mechanically controlled break junctions are either fractured under external force or electromigration. In case of externally applied force, a bridge of thin metal strip is suspended over flexible substrate [7]. The junctions can be introduced by bending the flexible substrate as shown in Figure 2.3. In electromigration technique, a high current is allowed to pass through the thin metal line under the application of external electric field. It produces a high current density which kicks off heavy electron flow. The momentum of the electron is transferred to the charged defect in the metal line. The transferred momentum keeps growing and electromigration occurs when it effectively pushes the metal atoms in the direction of electron flow and results into making of break-junctions as shown in Figure 2.4 [8].

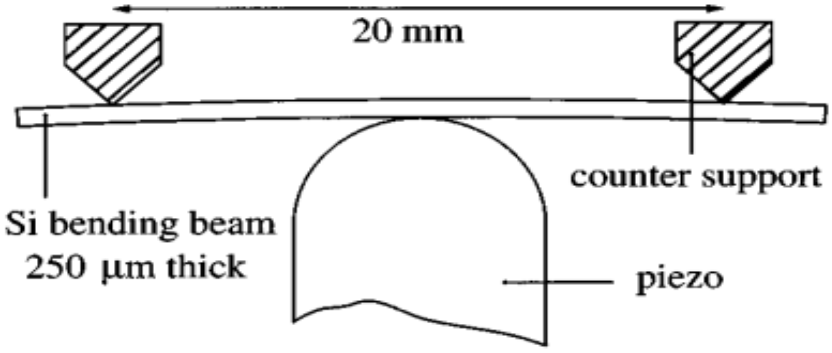

Figure 2.3 Controlled mechanical bending to induce break-junctions. Reprinted by permission from American Institute of Physics: Applied Physics Letters [7], copyright (1995)

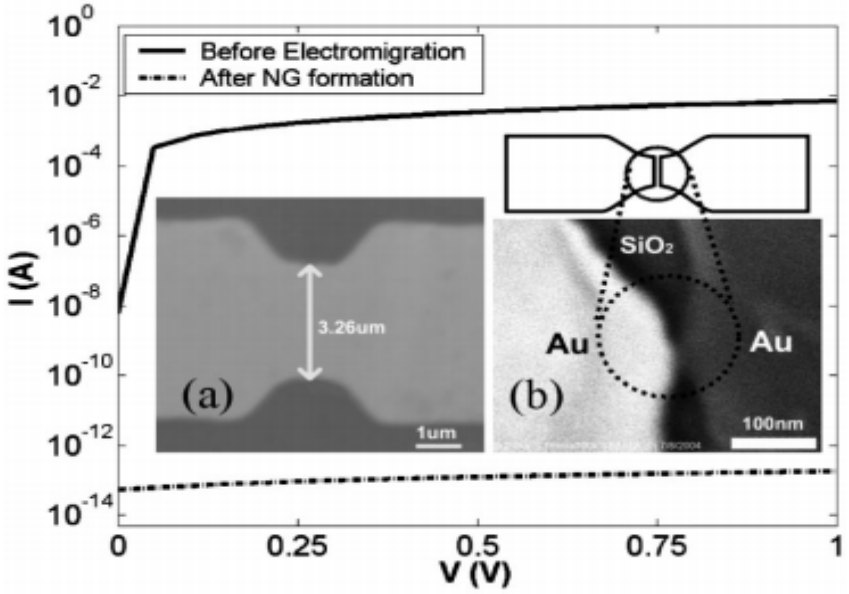

Figure 2.4 SEM micrograph of metallic strip (a) Before electromigration. (b) After electromigration which gave break junction with nanoscale separation. Reprinted by permission from American Institute of Physics: Applied Physics Letters [8], copyright (2005)

2.1.3 Fabrication of Break-junctions

Several fabrication schemes have been deployed to manufacture metallic break junctions with nanometer sized separation. The fabrication processes with their pros and cons are explained in the following sub sections.

2.1.3.1 E-Beam Writing for Fabrication of Break Junctions

E-beam lithography is widely involved in nanomanufacturing of break junctions. In one of such fabrication processes, oxidized silicon (Si) wafer was used to deposit 60 nm thick layer of silicon nitride using low pressure chemical vapor deposition (LPCVD) technique. E-beam lithography was employed to define a pattern of few mm long and 100-150 nm wide slit. The pattern was transferred to underlying layer of silicon dioxide using reactive ion etching with SF_6

plasma. The wet chemical etching of oxide using hydrofluoric acid underetched the nitride film and gave two overhanging silicon nitride structures as shown in Figure 2.5 [9]. Thin layer of Au was sputtered across the slit which divides the gold strip into two parts with 100 nm separation. Carbon nanowire was grown on the overhanging beam structures using e-beam exposure. Carbon nanowires started growing from the edge of gold film towards the gap. The growth of carbon nanowires could be discontinued at any time to get a break-junction of specific nanogap. This method of using electron beam deposition gave break junctions with a gap of 4 nm as shown in Figure 2.6. This approach provides higher yield and precise control over nanogap but has to go through slow linear scan of electron beam which turns it into an extremely low throughput process.

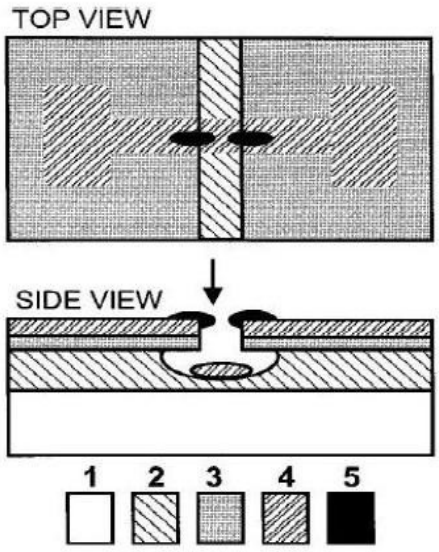

Figure 2.5 Schematic view of nanogap break-junctions made through e-beam writing. (1) Si wafer (2) Silicon dioxide (3) Siilcon nitride (4) gold (5) carbon nanowires. Reprinted by permission from American Institute of Physics [9], copyright (1997)

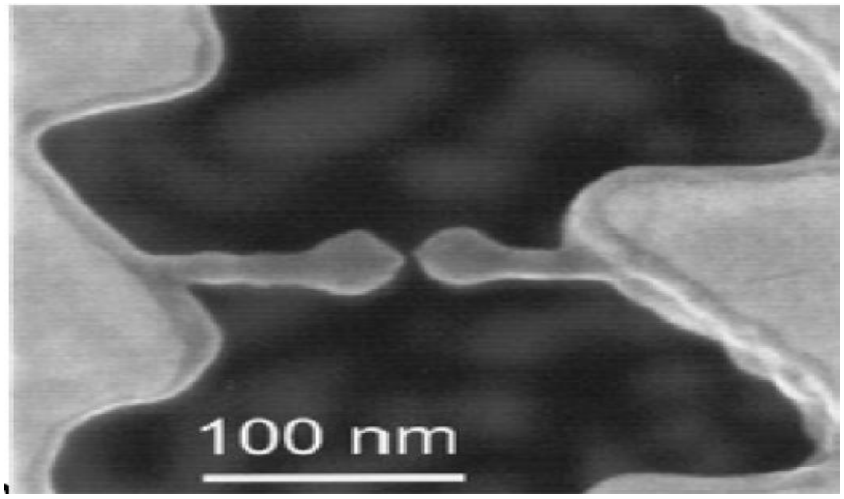

Figure 2.6 SEM micrograph of a break junction with about 4nm gap fabricated with e-beam deposition. Reprinted by permission from American Institute of Physics [9], copyright (1997)

2.1.3.2 Mechanically Controlled Manufacturing of Break Junctions

Break-junctions can be fabricated by microfabrication process where external force is used to crack the metal line and obtain break junction [7]. In one of such processes, e-beam lithography was used to define gold patterns on a Si wafer with 400 nm thick oxide layer. Conventional photolithography was used to deposit thick layer of Al on whole of the wafer except a particular region centered around the smallest feature in gold patter. Silicon dioxide was etched using dry etching where both the metallic layers worked as the etch masks. The Al was removed using simple wet etching and then anisotropic wet chemical etching of Si was carried out to make triangular pit in the Si wafer. It resulted into the final device that had two cantilever beams connected by 100 nm wide gold wire. Finally, a controlled force is applied on the backside to create a fracture in gold wire, giving thin metal line with a small nanogap. This method incorporates two major drawbacks. E-beam writing is a slow process which reduces the

throughput and mechanical breakage decreased the yield. Figure 2.7 shows the two devices hanging over triangular pit before fracture.

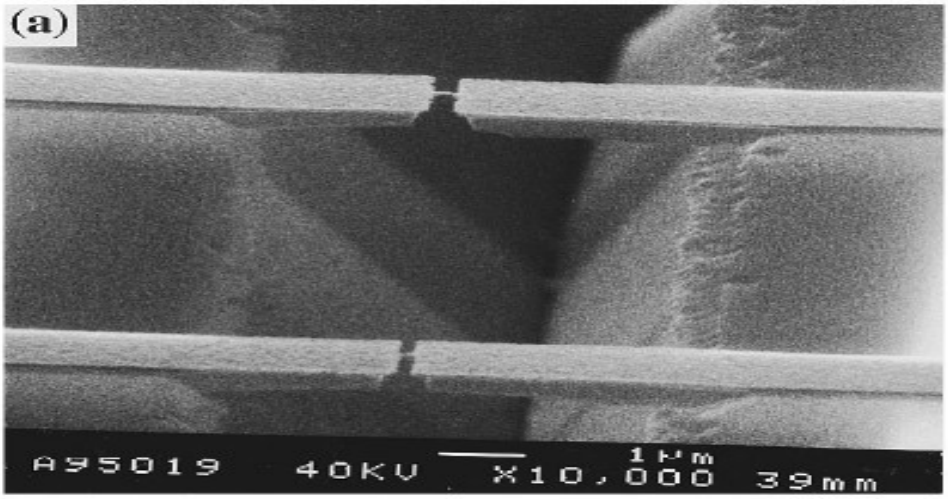

Figure 2.7 Figure shows the two devices hanging over the etched cavity in Si before breaking the connecting wire to get the break junction. Reprinted by permission from American Institute of Physics: Applied Physics Letters [7], copyright (1995)

2.1.3.3 Electromigration to Fabricate Break Junctions

Electromigration can also be used to induce fracture in the thin metallic strip to manufacture break junctions. Since electromigration occurs at the point of most resistance, so Park et al. used shadow evaporation of gold to intentionally create a locus of highest resistance in the nanowire. E-beam lithography was used to create a 200 nm long suspended resist bridge, 400 nm above the oxide surface. Metallic nanowires were introduced by evaporating 3.5 nm of chrome film followed by 10 nm gold at an angle of $\pm 15^{o}$ with respect to the substrate normal [10]. The angled deposition gave a shadowed deposition of the Au. Then, 3.5 nm of chrome followed by thick layer of gold (80 nm) were deposited straight down to oxide surface. Conventional photolithography was used to ensure a connection with the nanowire and alignment of thick gold contact pads. The break junction was generated using electromigration.

A sweeping voltage was applied across the two Au pads which resulted into flow of electric current. At certain threshold voltage, sudden drop in current was observed that indicated the nanowire breakage. The ohmic current changed to tunneling current when the connected gold line is ripped into two electrodes with nanometer breach. The break-junctions would mostly form at regions where two shadow-evaporated electrodes overlapped because the thin metal layer formed the most resistive locus in this region. Figure 2.8 shows SEM micrograph of a particular break-junction before and after electromigration occurs [10].

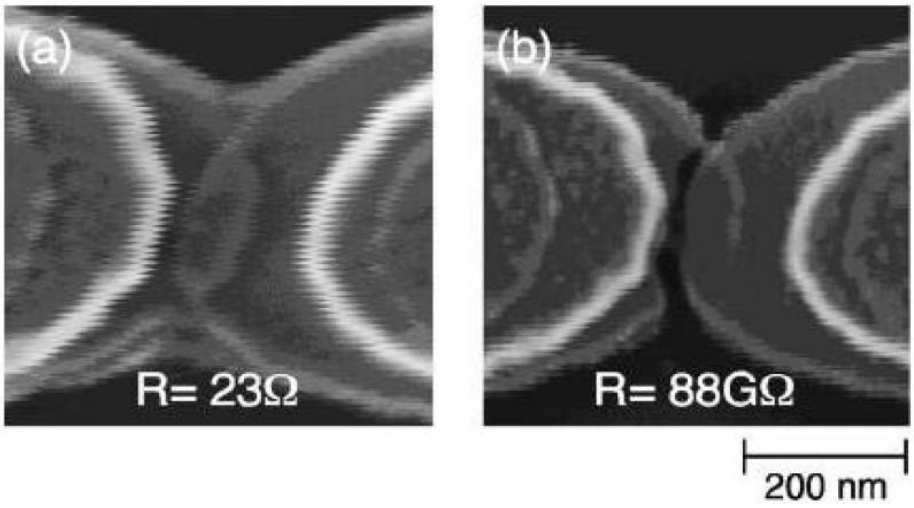

Figure 2.8 SEM micrograph of a representative break-junction (a) before and (b) after electromigration. Reprinted by permission from American Institute of Physics: Applied Physics Letters [10], copyright (1999)

2.1.3.4 Combination of SAM and E-beam Lithography for Break Junction Fabrication

Recently a combination of self assembled molecular (SAM) and electron beam lithography has been deployed to fabricate break junctions with nanoscale separation. In this method, oxidized Si wafer was used to define first electrode using E-beam lithography followed by metal deposition and lift-off on the silicon dioxide surface as shown in Figure 2.9 [11]. Then,

the multilayer films composed of a functional mercaptoalkanoic acid and a coordinated copper ion were deposited layer by layer to get a defect free SAM resist layer on top of metal electrode. Next, the second electrode was defined using the E-beam lithography followed by metal deposition. The second electrode was patterned such that it crossed the first electrode at right angle. Fianally, the SAM resist layer was removed using resist stripper. Photoresis removal left behind two metal electrodes separated by nanoscale gap. This process gave higher yield of nanogap electrodes but involves slow process of E-beam lithography.

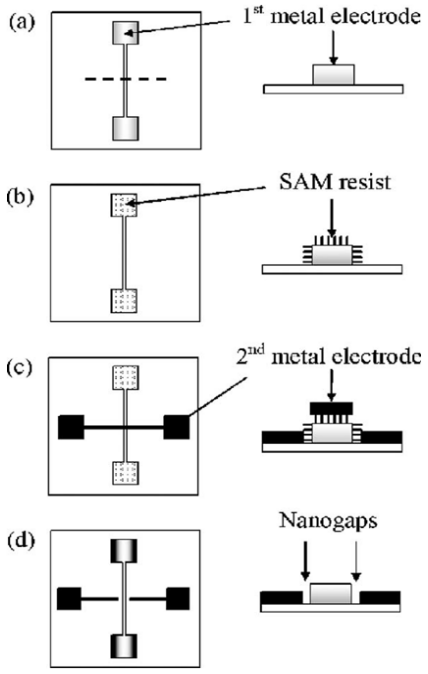

Figure 2.9 Schematic of process flow for break junction manufacturing (a) First metal electrode using EBL and sputter coating (b) Layer by layer deposition of SAM (c) Second electrode is defined using EBL (d) Resist removal to get nanogap electrodes. Reprinted by permission from American Institute of Physics: Applied Physics Letters [11], copyright (2006)

2.1.3.5 Step Junctions with Nanogap Separation

Electrodes with nanoscale gap can also be fabricated using conventional microfabrication techniques. In this process, positive slope of the developed pattern edge in the positive

photoresist was transferred to corresponding negative slope in the deposited metal layer after the lift-off process. The negative slope of metal feature worked as a shadow for the second thinner metal layer. This sequel deposition of metallic films gave a nanoscale gap, denoted as step junction, between the two metal electrodes. The schematic drawing demonstrating the fabrication process for step junction is shown in Figure 2.10 [12].

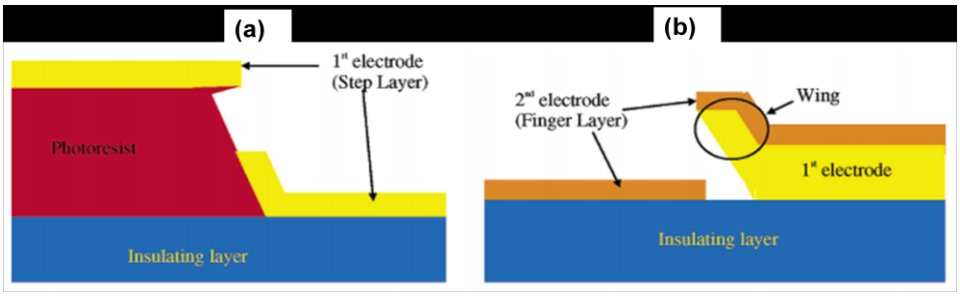

Figure 2.10 Schematic representation of the fabrication process for step junctions. (a) First electrode/step layer deposited on positive slope resist pattern. (b) Second thinner electrode layer/finger layer deposited after the lift-off process. Reprinted by permission from American Chemical Society: Nano Letters [12], copyright (2004)

2.1.4 Aptamers

Antibodies have been widely used for surface functionalization to selectively bind to the target molecule. Antibody based detection devices are not much compatible with field-deployable or point-of-care devices because in order to retain their functionality, the buffer solution needs to be maintained within specific range of temperature, humidity and ionic strength [13]. Low ionic strength is needed to overcome the surface Debye screening but it causes poor interaction between the target and the surface probes [13]. Aptamers have been recognized as a new class of recognition elements used for selective binding to a broad range of target molecules. Aptamers are as selective and sensitive as antibodies but exceedingly

stable over changing temperature, humidity and ionic concentration which makes it a strong candidate to replace antibodies [14].

Aptamers are short single-stranded nucleic acid oligomers (ssDNA or RNA) which have a specific and complex three-dimensional structure. The shape of the aptamers is defined by the loops, bulges, pseudoknots and the hairpins. Depending upon their 3-D structures, aptamers can specifically fit to a particular target. A wide range of targets including single molecules and large proteins or even the entire organisms can find their structure compatible with aptamers as shown in Figure 2.11 [15]. The aptamers bind to the target molecules owing to their well-fitting structure and several other interactions, which reveal that aptamers can be used to develop a variety of biosensors with high detection sensitivity and selectivity [16].

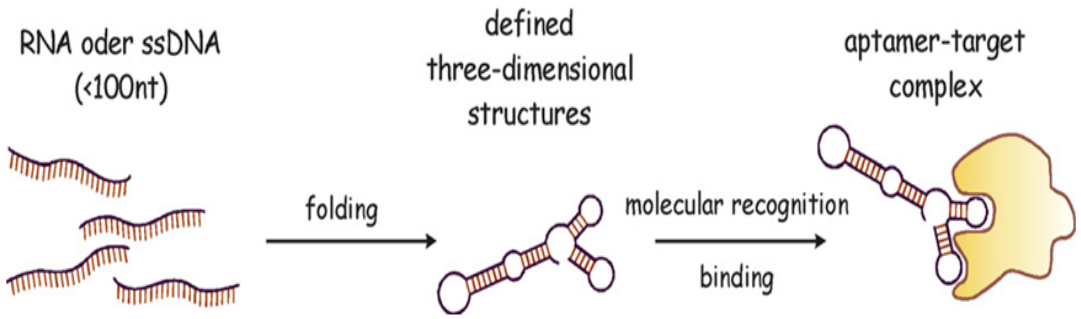

Figure 2.11 Representation of aptamer binding to a given target Reprinted by permission from Elsevier: Biomolecular Engineering [15], copyright (2007)

2.1.5 Preparation of Aptamers

Aptmers have gained tremendous attention in industrial and scientific communities due to their *in vitro* preparation unlike the antibodies. Aptamers are mostly isolated through an artificial process based on Systematic Evolution of Ligands by EXponential enrichment (SELEX), which is an iterative selection process as explained in Figure 2.12. In this process,

target-specific aptamers are isolated by repeating successive steps until the aptamer is finally selected.

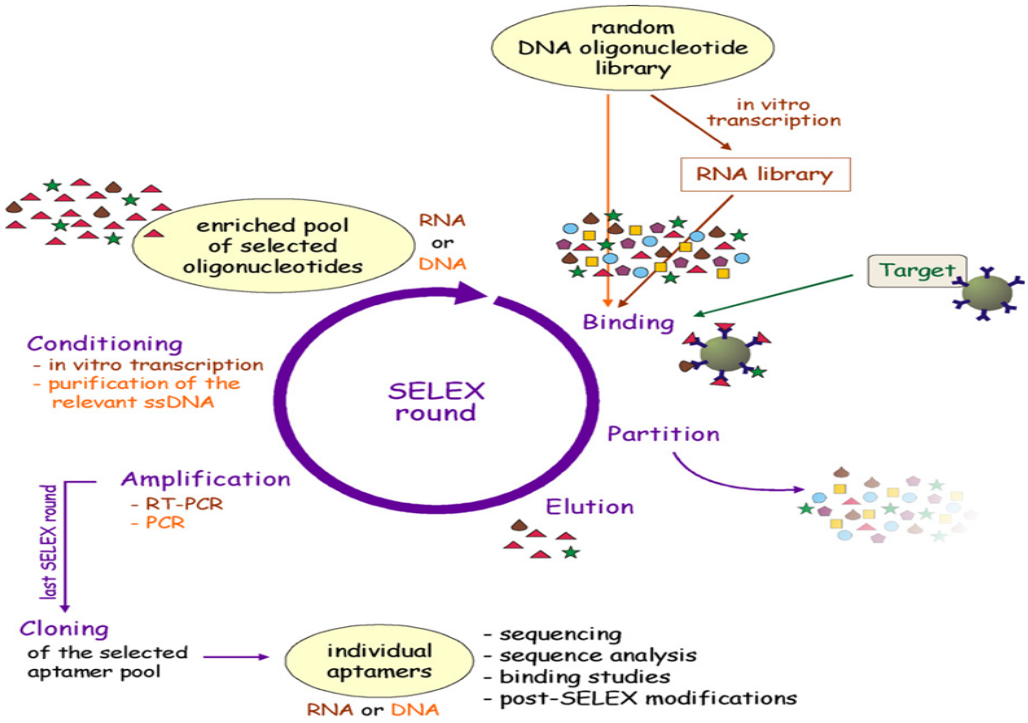

Figure 2.12 Process flow for isolating an aptamer through SELEX process Reprinted by permission from Elsevier: Biomolecular Engineering [15], copyright (2007)

The SELEX process starts by incubating the target molecule into a random DNA oligonucleotide library that contains a large number of ssDNA fragments with different sequences. For RNA aptamer selection, the library has to be converted to RNA library before starting the SELEX process. After incubation, the binding complexes are separated from the unbound and weakly bound oligonucleotides. The target-bound oligonucleotides are eluted and amplified by PCR for DNA aptamers or RT-PCR for RNA aptamers. Relevant ssDNA from the PCR products (DNA SELEX) or by *in vitro* transcription (RNA SELEX) are used to prepare a new oligonucleotide pool. This new pool of selected oligonucleotide is used for incubation of the

target for the binding reaction in the second SELEX round. This process of selecting and amplifying target-specific oligonucleotides is typically repeated for 6 to 20 times to obtain a highly selective aptamer for the given target. The last SELEX round is stopped after the amplification procedure. Iterative cycles of selection and amplification gradually reduce the number of oligonucleotides in the pool by selecting those oligonucleotides which are more specific and have high affinity for the target.

Unlike antibodies, aptamer selection process doesn't rely on induction of an animal immune system. A revolutionary aspect of the SELEX technology is the preparation of aptamers for non-immunogenic and toxic targets also, which would not have been possible in a living organism [17]. Moreover, aptamers for specific region of the target can also be produced which is complicated for antibodies because animal-immune system has natural epitopes on target molecules [17]. Capability to select ligands beyond natural systems, enhanced chemical stability and high reproducibility has enabled aptamers to emerge as a rival to antibodies in molecular diagnostics.

2.1.6 Aptamer-based Biosensors for Molecular Detection

A large number of label-based and label-free detection schemes have been deployed for identification of various protein molecules using aptamers. The design of the sensing platform gernarlly depends upon the detection mode of aptamer-target pair. In case of labeled detection, a secondary molecule (organic, inorganic or radioactive) binds to the target and reveals the presence of the target molecules. Biosensors with optical detection make use of fluorescent tags to interrogate the presence of target molecules. Electrochemical aptasensors probe the electron transfer features of redox moieties tethered to the aptamers immobilized on a conducting surface [16]. Aptamers undergo conformational transition upon binding to their target molecules and form definite 3-dimenstional structures. The electron transport study indicates the formation of aptamer-target complex. In one of such electrochemical biosensor, redox-active

methylene blue (MB) labeled anti-thrombin aptamer was employed, which folded its flexible single stranded chain when bound to thrombin [18]. In the absence of target molecule, the aptamer remains relatively unfolded and allows the attached MB to colloid with the electrode and electron transfer occurs. But when the anti-thrombin aptamer is selectively bound to thrombin, it folds to a 3-demensional conformation and prohibits MB from any electron transfer communication with the gold electrode as shown in Figure 2.13 [18].

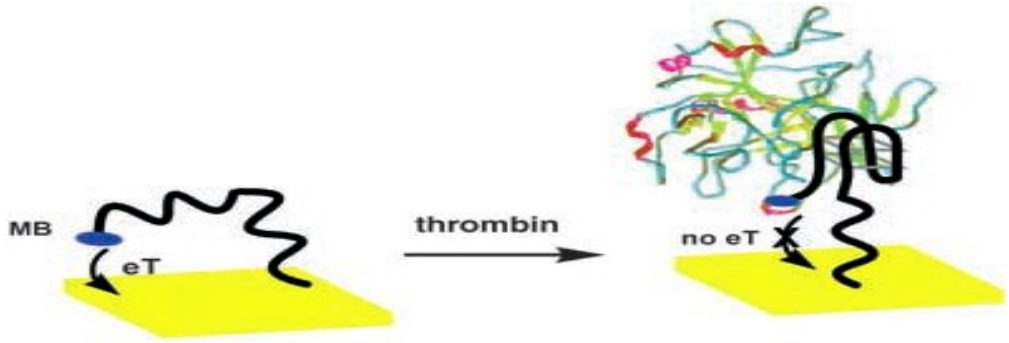

Figure 2.13 Electrochemical aptamer-based sensor that restrains electron transfer on aptamer-target binding. Reprinted by permission from John Wiley and Sons: Angewandte Chemie [18], copyright (2005)

In this sensing format, the signal is reduced upon binding to the target molecule so it is a negative signal detection approach which has certain limitation. The major drawback in such sensing scheme is to get false positives due to degraded aptamer or redox tag because it is very difficult to distinguish between the signals coming from authentic analyte binding and contaminants that have possibly degraded the aptamer. Therefore, a positive signal scheme where presence of target increases the single strength rather decreasing is considered more convincing.

A variety of sensing platforms have been developed where aptamer selectively binds to the target and an increase in signal strength is observed. Different types of fabrication schemes have been used to get electrodes with molecular dimension that include break junctions, carbon

nanowires, single walled and double walled carbon nanotubes. All of these devices work on the same principle that selective capture of target molecule causes a change in resistance which is detected by the sensing setup to point out the presence of the target molecule. Direct investigation of the target at single molecule level is the eventual aim of these electronic biosensors. In one of such aptamer-based biosensors, single-walled carbon nanotubes (SWNTs) have been used to capture and study the *I-V* characteristics from a single target molecule. SWNTs with nanometer separation were coupled with DNA aptamers which were highly selective to thrombin [19]. When the target molecule (thrombin) binds to the aptamer, a change in conductance occurs and *I-V* characteristics demonstrate the target detection by single-molecule device [19]. Figure 2.14 shows the schematic drawing of the device and its detection scheme. This device represents the state of the art strategy to detect single molecule of protein but has to undertake complex fabrication process for single-walled carbon nanotubes.

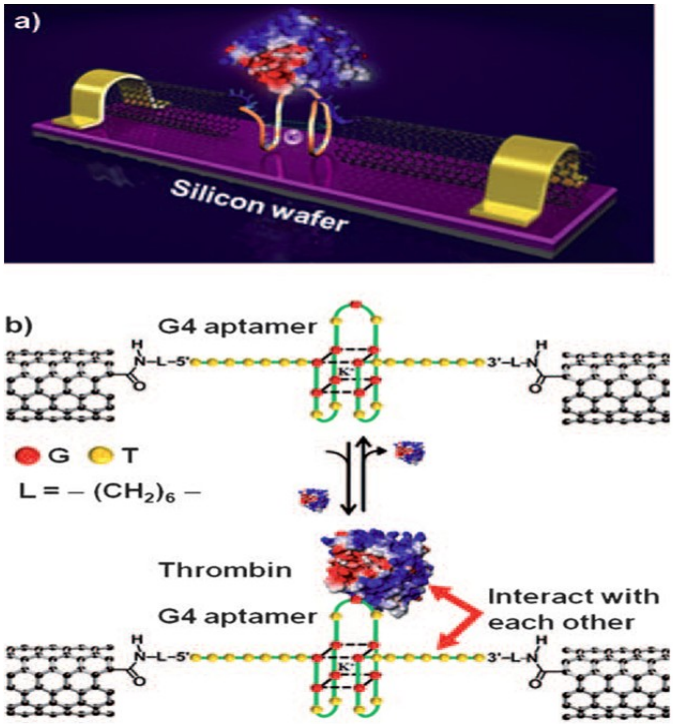

Figure 2.14 (a) Schematic representation of the sensing platform (b) Schematic drawing to show the detection mechanism by single molecule device. Reprinted by permission from John Wiley and Sons: Angewandte Chemie International Edition [19], copyright (2011)

2.2 Solid-state Micropore for Molecular Cell Biology

2.2.1 Molecular Cell Biology

Cell is the fundamental unit of life and performs numerous functions that indicate life. Cells can grow, reproduce, respond to stimuli and interact with each other. The study of cells, their structures, shapes, physiological properties, transportation, life cycle, interactions with their microenvironment and their constituents, is undertaken by molecular cell biology. It is an interdisciplinary science that integrates biophysics, biochemistry, physiology, molecular biology, computer science and engineering. The learning of similarities and differences between various cell types, cell growth, morphology, cell's alterations, molecular architecture and biomechanical properties are the hallmarks of this science discipline. The study is carried out at both microscopic and molecular level. Optical and electron microscopes are the major research tools used in molecular cell biology. Electron microscope provides a much higher resolution than optical microscope but requires that cell be fixed and sectioned, with all cell movements frozen in time. Thus, living cells cannot be images by electron microscopy [20].

Various technical constraints restrain studies on intact animal and plant cells. Though intact organs removed from animals can be chemically treated to preserve their physiological integrity and functions but even the isolated organs are complex enough to pose several challenges for molecular cell biologists. Therefore, experimental studies are typically carried out on individual cells isolated from an organism.

2.2.2 Cell Culture

The process of maintaining the isolated cells in laboratory under controlled conditions that facilitate their survival and growth is called cell culture. The cells are cultured in an artificial environment which provides a suitable surface or medium with essential nutrients, growth factors, hormones and ideal conditions of temperature, humidity and gaseous atmosphere. Most of the cells are anchorage-dependent which require a solid or semi-solid substrate for their

growth while others can be cultured floating in the medium, known as “adherent culture” and “suspension culture” respectively. The cultured cells offer several advantages over intact organisms in cellular and molecular biology. Cells of a single specific type can be grown and the effects of drugs and toxic compounds on the cells can be studied [20]. It is also used for drug screening by precisely monitoring the cell’s response to the prospective drugs. Cell culture has facilitated biologists with the study of cell alterations in the presence of any carcinogenic agent or virus. The major benefit of cell culture is to grow a batch of clonal cells which provide highly consistent results. Several biological compounds like vaccines are produced on large scale from such cultured cells due to their steady and reproducible outcome [21].

2.2.3 Cell Morphology and Cytoskeleton

Cell morphology refers to the shape and appearance of cells under microscope. The cultured cells are generally classified as fibroblast-like (elongated in shape), epithelial-like (polygonal in shape) or lymphoblast-like (spherical in shape) based upon their contour in culture medium. The morphology of cells is strongly coupled with the physiological state and functions of the cell. Regular inspection of cell culture to examine any morphological alterations is critically important to confirm the healthy status of cells and notice any signs of contamination.

Several diseases like cancer alter the morphological and functional characteristics of the cells. Cancer cells are marked by their rapid growth, irregular size and shape with larger nucleus, genomic alterations and increased cell mobility. These characteristics can be used as biological markers for identification of these diseased cells. The shape of the cell, its mechanical rigidity and important cellular functions are governed by a complex three-dimensional polymer network, known as cytoskeleton [22]. Transmission electron microscope (TEM) micrograph representing cell’s cytoskeleton is shown in Figure 2.15. Cytoskeleton can surprisingly withstand an enormous external pressure and preserves the cell’s integrity [23]. It not only provides the structural framework to the cell but also plays an essential role in cell division,

locomotion and transport of intracellular particles [23]. Changes to cellular functions or morphology of diseased cells are mirrored in their cytoskeleton and cause cytoskeletal alterations. Cancer transforms the cell's cytoskeleton from a rigid and moderately ordered structure to a flexible and more asymmetrical formation [24]. Cancer cells are marked for enhanced motility and replication which stems from the flexible cytoskeletal structure. Changes to cytoskeletal content and configuration alter the overall mechanical properties of cell so stiffness of cell can indicate its state [22].

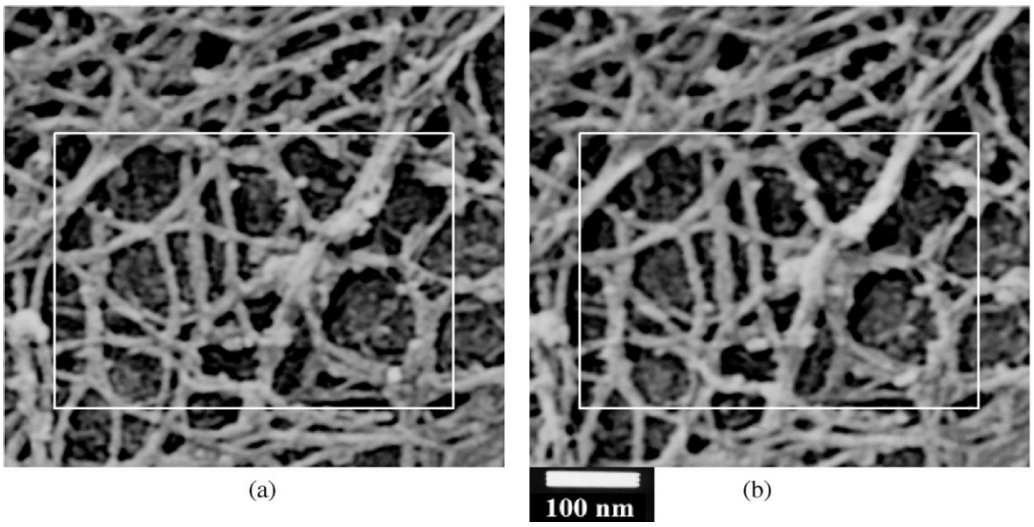

Figure 2.15 TEM micrograph of cell's cytoskeleton at tilt angles of $\pm 10^{o}$. (a) The image taken from left side and (b) right side can be combined to construct 3D images using this stereo image technique. Reprinted by permission from Elsevier: Journal of Biomechanics [25], copyright (2000)

2.2.4 Biopsy

The procedure to collect a tissue or cells sample from the suspicious locale for cancer is called biopsy. Cancer cells from the primary tumor can be collected through open surgical biopsy or image-guided interventions which obtain the tissue sample from the exact area but involve increased risk of procedural complications and longer recovery time [26]. Needle biopsy

is more commonly used clinical procedure that incorporates fine needle aspiration (FNA) and core biopsy. FNA uses a very fine needle of 22-gauge (22G) and a syringe to take out a small amount of fluid and very small tissue sections from the tumor whereas core needle biopsy uses a little larger needle (usually 16G or 19G) to obtain a small tissue segment for histology and immunohistochemical analysis [27]. Minimally invasive needle-biopsy provides better patient compliance, fewer complications, lower cost, faster recovery time and speedy analysis but may lead to misdiagnosis due to inaccurate sample collection [26]. Primary and metastatic solid tumors are composed of tumor cells and health normal cells like endothelial cells, fibroblasts and immune/inflammatory cells [28]. Low grade cancer and inaccurate sample collection by needle biopsy can give a normal cell enriched sample with very few cancer cells. Diagnosing cancer by looking at such samples is highly time consuming, technically challenging and more liable to misdiagnosis. Cytology and immunohistochemistry make use of stains (colored dyes) but these are also limited by high turn-around time, semiquantitative results, expensive and complicated procedural steps.

2.2.5 Cancer Cell Detection Models

Several detection schemes have been employed to identify cancer cells. The design of the model depended upon the selection of the marker which was used for cancer cell identification. Pathologists observe the size and shape of the cell, size and shape of nucleus and arrangement of cells to conclude their diagnosis on cytology. A variety of detection systems (immunohistochemistry, flow cytometry, surface functionalization) make use of antibodies or aptamers to selectively bind to certain antigens present on cancer cells for their detection. Flow cytometer is a widely used microfluidic device that uses a laser beam to screen the investigated sample. The sample is treated with special antibodies which are selective to the tumor cells and analysis of scattered beam indicates the presence of the cancer cells. Recently, some detection schemes are based on measuring the rigidity of cells to discriminate the cancerous cells from

the healthy ones. The state of art stiffness measuring systems are scanning force microscope and microfuidic optical stretcher.

2.2.5.1 Scanning Force Microscopy

In this method, the mechanical properties of cells are investigated by using the scanning force microscope (SFM). Lekka et al. used a home-built scanning force microscope to compare the elasticity of cancer cell lines and their complementary normal cell lines and found that cancer cells were much softer than their normal counterpart [29]. In this method, the young's modulus was determined to calculate the elasticity of the cells. All different types of cell lines were grown on separate clean and hydrophilic glass coverslips. After the cells formed an adherent monolayer, the sample was taken for measurement under SFM. The cells were not fixed or dried. Silicon nitride cantilever tip was lowered exactly at the center of a representative cell to eliminate surrounding influence. The interaction between the probing tip and cell surface was recorded to assess the force vs cell indentation. Figure 2.16 shows the schematic for SFM.

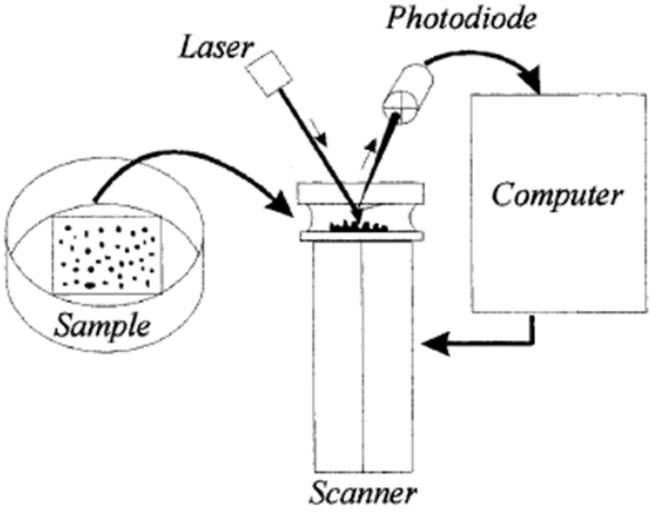

Figure 2.16 Schematic representation for the experimental setup used for measuring the elasticity of living cells. Reprinted by permission from Springer: European Biophysics Journal [29], copyright (1999)

2.2.5.2 Microfluidic Optical Stretcher

In this strategy, optical deformability of cells is measured to evaluate the cell's stiffness. The cells suspended in liquid are allowed to pass through a two-beam laser setup as shown in Figure 2.17 [22]. The measuring system is optimized to serially trap and stretch single suspended cell by optically induced surface forces. Two counter propagating divergent laser beams induce surface forces and the distribution of these forces on the surface of cell is optimized for sequel trap and deformation of a single suspended cell. This method provides a way to quantify cell's rigidity in rapid succession through microfluidic delivery and doesn't need any cell modification [22].

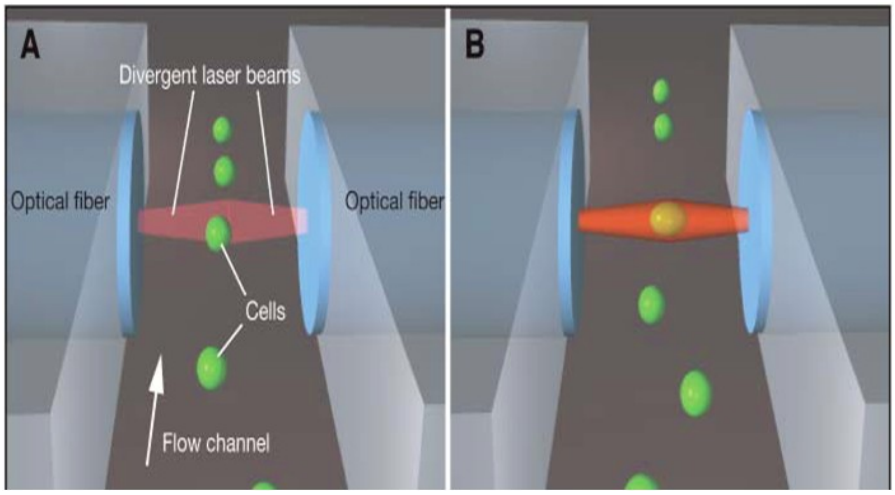

Figure 2.17 Two beam laser setup for measuring optical deformability of cells (a) cell trapped (b) stretched under optically induced surface forces. Reprinted by permission from Elsevier: Biophysical Journal [22], copyright (2005)

The images for trapped and stretched cells were analyzed to calculate the deformation produced in the suspended cell. This method also revealed that cancerous cells are more flexible than normal cells as shown in Figure 2.18. Metastatic cancer cells were found to be even more flexible because they had to squeeze through the surrounding tissue matrix to get into circulatory systems and travel to form secondary tumor in another part of the body [30].

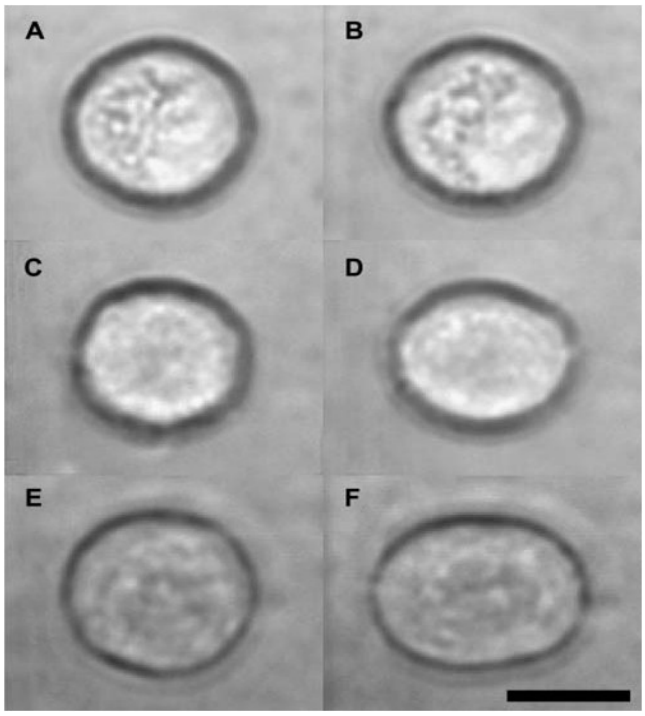

Figure 2.18 The left column shows micrographs cell trapped under low incident power (100 mW). The right column shows micrographs for stretched cells under higher power (600 mW). Cancer cells (C to D) are more flexible than noncancerous cells (A to B) whereas metastatic cancer cells (E to F) are even more deformable. Reprinted by permission from Elsevier: Biophysical Journal [22], copyright (2005)

2.2.6 Solid-state Micropore Sensors

Solid-state micropores have been employed in a wide range of sensor applications owing to their chemical and thermal stability, mechanical strength and capability to be used in Lab-on-a-chip settings. These have been used for patch clamp measurements, electroporation, stability of lipid bilayers, bacterial activities monitoring, size based discrimination, cell enumeration and electric characterization of cells [31-36]. The micropores have also been deployed for determining the deformability of red blood cells (RBCs) where individual microscopic images of RBCs were processed to evaluate the cell's deformation while passing

through the micropore [37]. In this study they employed rectangular microscale slits and circular micropores to study the deformation of RBCs while passing through them and concluded that the cells were more obstructed by circular micropores [37]. Hence, circular micropores are exceptionally sensitive to mark the micro-organism passing through them.

2.2.7 Micropore Fabrication Techniques

Several methods have been used to manufacture micropores in a simple, rapid and controlled environment. A few fabrication processes with their advantages and disadvantages have been described below.

2.2.7.1 Heated Tip for Micropore Drilling in Teflon

A heated probe tip has been used to drill a micropore in Teflon [33]. In this method, a heated Tungsten wire was used to fabricate micropores in low-melting Teflon film (ETFE). Ag/AgCl plate with a small hole was glued to 12 μm thick ETFE film. A cover glass was used to hold the film and electrochemical polished Tungsten tip was positioned at the center of the hole in Ag/AgCl plate by using a microscope as shown in Figure 2.19. The tip was moved down to pierce a hole in the ETFE film at the point of contact between the tip and the cover glass. The process was characterized using similar Tungsten tips at different temperatures. It was noticed that moderate temperature gave optimum drilling of micropore without harming the Teflon film as shown in Figure 2.20. Similarly, electrochemical process was also optimized to study the effect of the heated probe tip. Although this is a simple and quick approach to fabricate micropores but is limited by the material characteristics. This strategy cannot be used to drill micropores in materials with high melting point or high rigidity. Therefore, solid-state micropores cannot be fabricated using this process.

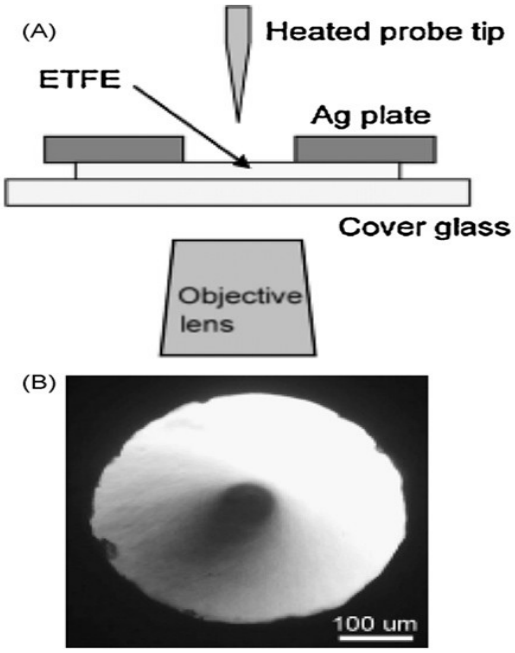

Figure 2.19 Schematic representation of the fabrication process (B) Placing the heated tip in the middle of the opening in Ag/AgCl plate. Reprinted by permission from Elsevier: Biosensors and Bioelectronics [33], copyright (2009)

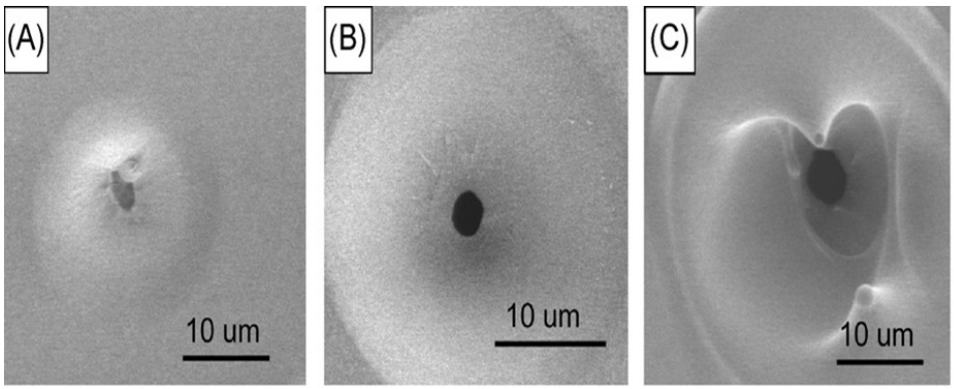

Figure 2.20 Characterization of the fabrication process where SEM micrographs show micropore fabricated by using (A) Nonheated tip (B) Moderately heated tip (C) Extremely heated tip. Reprinted by permission from Elsevier: Biosensors and Bioelectronics [33], copyright (2009)

2.2.7.2 Micropore Fabrication using Deep Reactive Ion Etching (DRIE)

Conventional photolithography followed by deep reactive ion etching (DRIE) can be used to fabricate solid-state micropores. Pantoja et al. has used this process to manufacture silicon chip-based micropore devices [38]. Figure 2.21 demonstrates the process flow for the fabrication of micropores. Optical lithography was used to define 2 μm circles on the silicon substrate and DRIE was employed to etch the silicon down to 20-40 μm. The photresist was stripped off and wafer was inverted for backside processing. Larger circles (1 mm in diameter), centered on the 2 μm wells, were defined and DRIE was used to etch them down all the way to meet the 2 μm wells. Finally, silicon dioxide was deposited to electrically isolate the two sides of the wafer. The oxide deposition reduced the size of the micropore and process could be varied to decrease the diameter down to nanopores. This method is limited by the complex fabrication process involving DRIE and may result in asymmetrical circular periphery of the fabricated micropores.

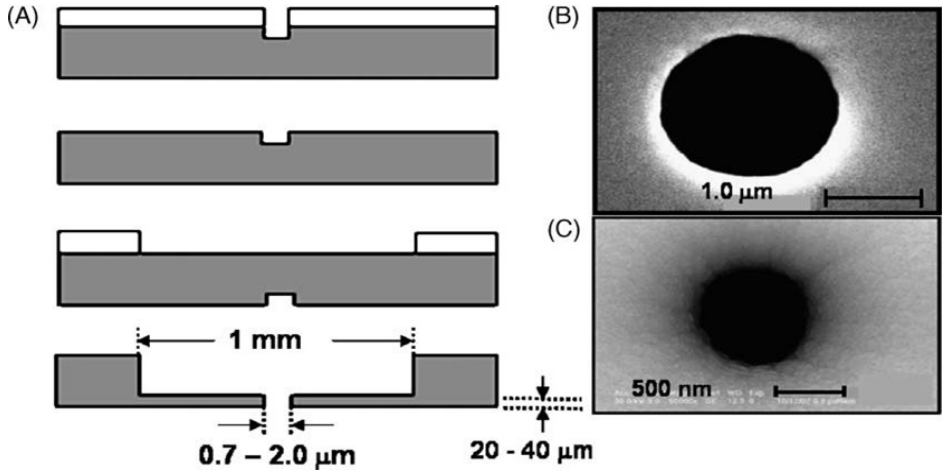

Figure 2.21 Fabrication of micropores (A) Process flow showing step by step progress in fabrication (B) SEM micrograph of the micropore (C) SEM micrograph of nanopore obtained by varying the oxide deposition process. Reprinted by permission from Elsevier: Biosensors and Bioelectronics [38], copyright (2004)

2.2.7.3 Anisotropic Etching of Silicon for Micropore Fabrication

Solid-state micropores can also be synthesized using anisotropic wet chemical etching of silicon. Chang et al. made use of this technique to fabricate solid-state micropores [35]. In this process, a double side polished silicon wafer with (100) orientation was used to grow 300 nm thick oxide layer. Optical lithography was used to pattern square window on the back of the wafer in order to etch silicon using tetramethyl- ammonium-hydroxide (TMAH) anisotropic etchant. It etched the silicon all the way throughout the thickness of the wafer at an angle to make a V-groove cavity as shown in Figure 2.22. The oxide was stripped off to get the micopore on the front side of the wafer. The wafer was oxidized again to grow a conformal layer of silicon dioxide. The opening square window size can be manipulated to get a micropore of desired size. The major drawback of this process is the absence of circular contour of the fabricated micropore. Moreover, a wafer defect may lead to different micropore size than intended, so the process lacks in control over the final micropore opening.

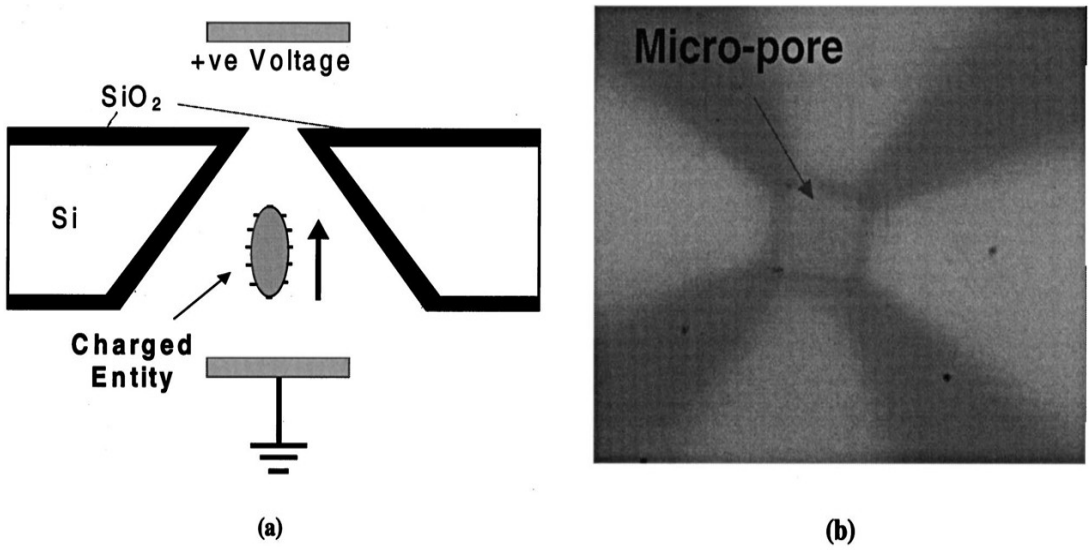

Figure 2.22 Micropore for electrical characterization (a) Cross sectional view of the micropore and electrical setup (b) Optical micrograph of the micropore obtained through TMAH etching of Si. Reprinted by permission from AIP Publishing LLC: Journal of Vacuum Science & Technology B [35], copyright (2002)

2.2.7.4 Ion and Electron Beam Sculpting for Micropore Drilling

The state of art in micropore fabrication is to use an ion/electron beam to drill micropores in thin films. Researcher at Harvard University introduced this technique for drilling nanopores in silicon nitride thin films using argon ion beam [39, 40]. They revealed that ions bombarded on the thin films result into surface erosion and surface diffusion. Surface erosion leads to the opening of the pore whereas surface diffusion roots the pore shrinking due to material transport. Since then ion beam sculpting has been extensively used for drilling pores in thin films [41-43]. In this process, the ion or electron beam is focused on a small area of free-standing membrane. The beam intensity melts the surface locally and drills a pore in the membrane. Li et al. used feedback controlled ion beam sculpting process for drilling a nanopore in silicon nitride thin membrane [40]. In this process, a bowl shaped cavity at one side of the membrane was created followed by ion bombardment which sputtered SiN layer by layer until a 60 nm pore was opened as shown in Figure 2.*23.*

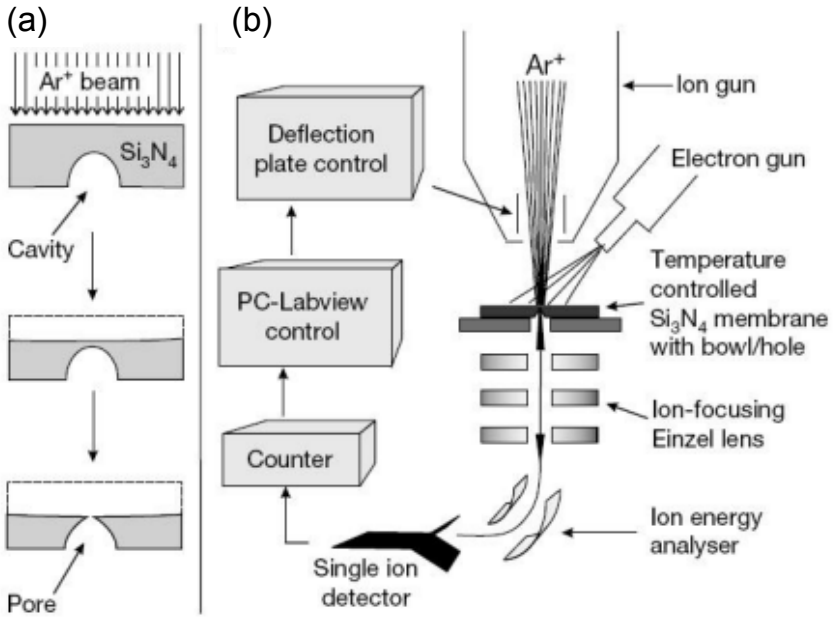

Figure 2.23 Ion beam sculpting process. (a) Schematic representation of drilling a nanopore in silicon nitride membrane (b) Feedback controlled ion beam sculpting method. Reprinted by permission from Nature Publishing Group: Nature [40], copyright (2001)

Typically all the ion beam sculpting processes require a free-standing thin membrane in oxide or nitride. Thin oxide membranes can be obtained by using anisotropic wet chemical etching of silicon. The etchants used for directional etching of silicon include tetramethyl-ammonium-hydroxide (TMAH), potassium hydroxide (KOH), ethylenediamine-pyrocatechol-water (EDP), and hydrazine-water solutions [44]. Some of the etchants are not CMOS compatible, for example, KOH etching turns out potassium ions (K^+) which can annihilate the device performance because K^+ are fast diffusers in Si. Therefore, TMAH is the widely used etchant for anisotropic wet chemical etching of silicon [45-47].

2.2.8 Tetramethyl-ammonium-hydroxide (TMAH) Etching

TMAH etches (100) silicon wafer at an angle of 54.7^o forming an inverted pyramid in silicon. A variety of MEMS devices, diaphragms, structures and cantilevers are fabricated using directional etching of silicon. While etching, TMAH gives excessive OH^- ions which are required to form water soluble silicate complex for silicon etching. The overall chemical reaction is given in Equations 2.1.

$$\left(CH_3\right)_4 NOH \rightarrow \left(CH_3\right)_4 N^+ + OH^- \qquad (2.1)$$

The hydroxide etching of Si take places in series of chemical reactions starting with the oxidation of Si surface and then chelation process forms water soluble product that is desorbed into bulk solution [46]. The chemical reactions involved in hydroxide etching of Si are shown in Equations 2.2-2.5

$$Si+2OH^- \rightarrow Si\left(OH\right)_2^{++} +4e^- \qquad (2.2)$$

$$Si(OH)_2^{++} + 4OH^- \rightarrow SiO_2(OH)_2^{--} + 2H_2O \qquad (2.3)$$

$$4H_2O + 4e^- \rightarrow 4OH^- + 2H_2 \qquad (2.4)$$

The overall redox reaction is expressed as

$$Si+2OH^- + 2H_2O \rightarrow SiO_2\left(OH\right)_2^{--} +2H_2 \qquad (2.5)$$

The Si etch rate of TMAH is affected by the temperature of the solution and the concentration of TMAH used for etching as shown in Figure 2.24. It shows that etch rate increases with temperature but higher concentration results in lower etch rate [46].

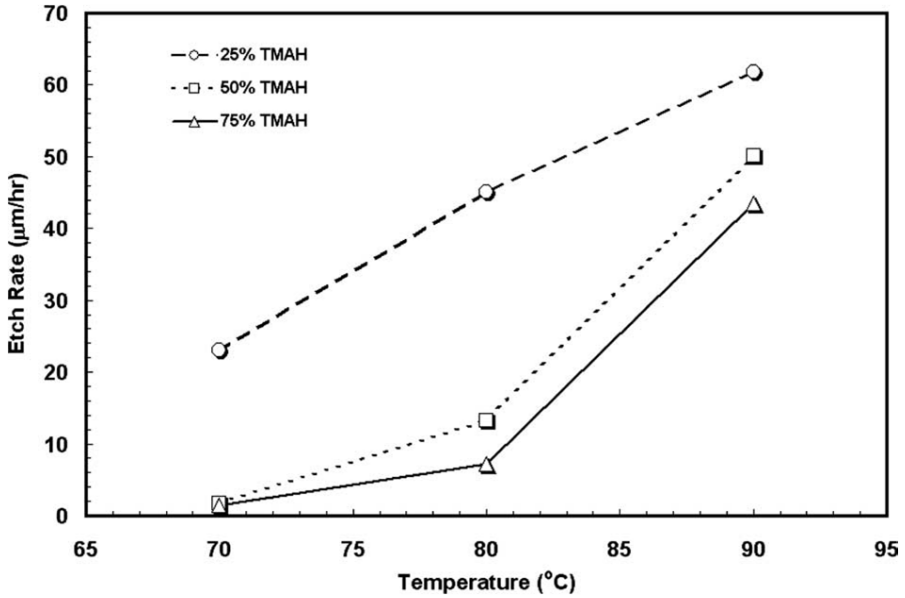

Figure 2.24 Etch rate of Si (100) at different TMAH concentrations vs solution temperature. Reprinted by permission from Elsevier: Microelectronic Engineering [46], copyright (2005)

The etch rate increases as the concentration of TMAH increases from 2% to 4% and decreases with further increase in TMAH concentration. *P*-type Si is etched slightly slower than n-type Si [48]. Figure 2.25 demonstrates the effect of TMAH concentration and solution temperature on the etch rate of TMAH. Isopropyl alcohol (IPA) is found to be very affective additive to reduce the roughness of Si surface etched in TMAH solution but decreases the etch rate of Si as shown in Figure 2.26. The reduced etch rate by IPA addition is assumed to result from the physical adsorption of IPA ions onto Si surface which blocks the contact of hydroxyl ions with Si surface. It slows down the chemical activity which results in lower etch rate [47]. The smooth Si surface is believed to result from less aggressive Si etching after IPA addition [47]. Addition of IPA in KOH solution has also been found to increase the surface smoothness.

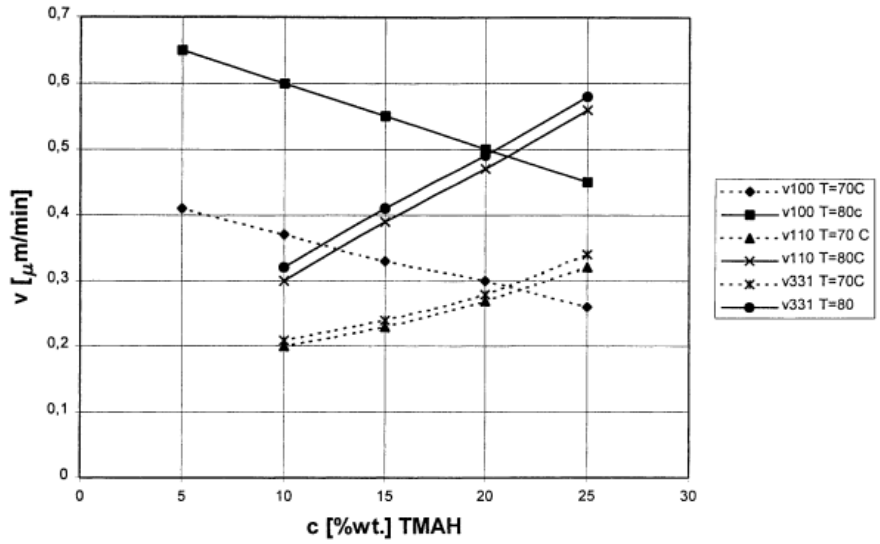

Figure 2.25 Etch rate of Si (h k l) planes in TMAH solution with respect to TMAH concentration, T = 80 ^{o}C: Solid lines, T = 70 ^{o}C: Dotted lines. Reprinted by permission from Elsevier: Sensors and Actuators A: Physical [47], copyright (2001)

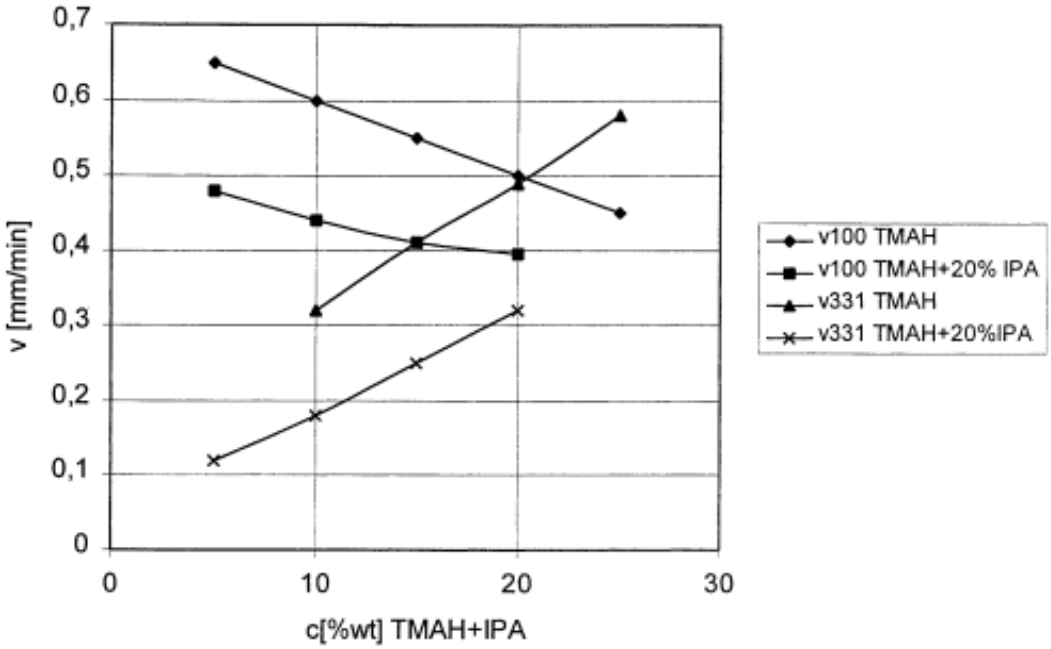

Figure 2.26 Comparison of etch rate of Si (h k l) planes in TMAH and TMAH+IPA solution at 80 ^{o}C [47]. It shows that etch rate is decreased by addition of IPA into TMAH solution. Reprinted by permission from Elsevier: Sensors and Actuators A: Physical [47], copyright (2001)

2.3 Micropores for Circulating Tumor Cells (CTCs) Detection

2.3.1 Carcinogenesis

The process, by which normal cells are transformed to cancer cells, is called carcinogenesis. Cancer cells divide and grow uncontrollably which is induced by some gene modifications (DNA mutations). Single gene defect doesn't cause cancer but several mutations lead to cancer development which explains the delayed onset of cancer [49]. Mutations in oncogenes increase the production of proteins that stimulate cell proliferation, and mutations in tumor-suppressor genes result in the loss of proteins that inhibit cell proliferation and induce apoptosis. Several mutations in these two types of genes lay the foundation for uncontrolled cell proliferation that leads to cancer [49]. Most relevant characteristic of cancer is the uncontrolled cell proliferation that needs signals for cell proliferation and the synthesis of macromolecules like proteins and nucleic acids as shown in Figure 2.27. DNA mutations provide the base for cell proliferation signals whereas building blocks for biosynthesis of these macromolecules are provided by the glycolysis process [49]. The upregulation of glycolysis results from the increased cellular uptake of glucose and oxygen from the blood vessels. But the presence of oxygen is known to cause glycolysis-inhibition (Pasteur Effect). It suggests that cell proliferation in the presence of oxygen is possible only after cancer cell make some alterations to oxygen metabolism. This variation in the metabolism of oxygen (dysoxic metabolism) is a frequent aspect of cancer cells and plays an important role in carcinogenesis [50].

It is widely recognized that cancer is caused by DNA alterations and can be treated by reversing or targeting these alterations [50-52]. A complex set of genetic alterations is not easy to target or reverse. Since cancer cells also develop an alteration in the metabolism of oxygen which doesn't involve genetic complexity so should be a more reliable and easy target for cancer therapy as explained in Figure 2.28 [49].

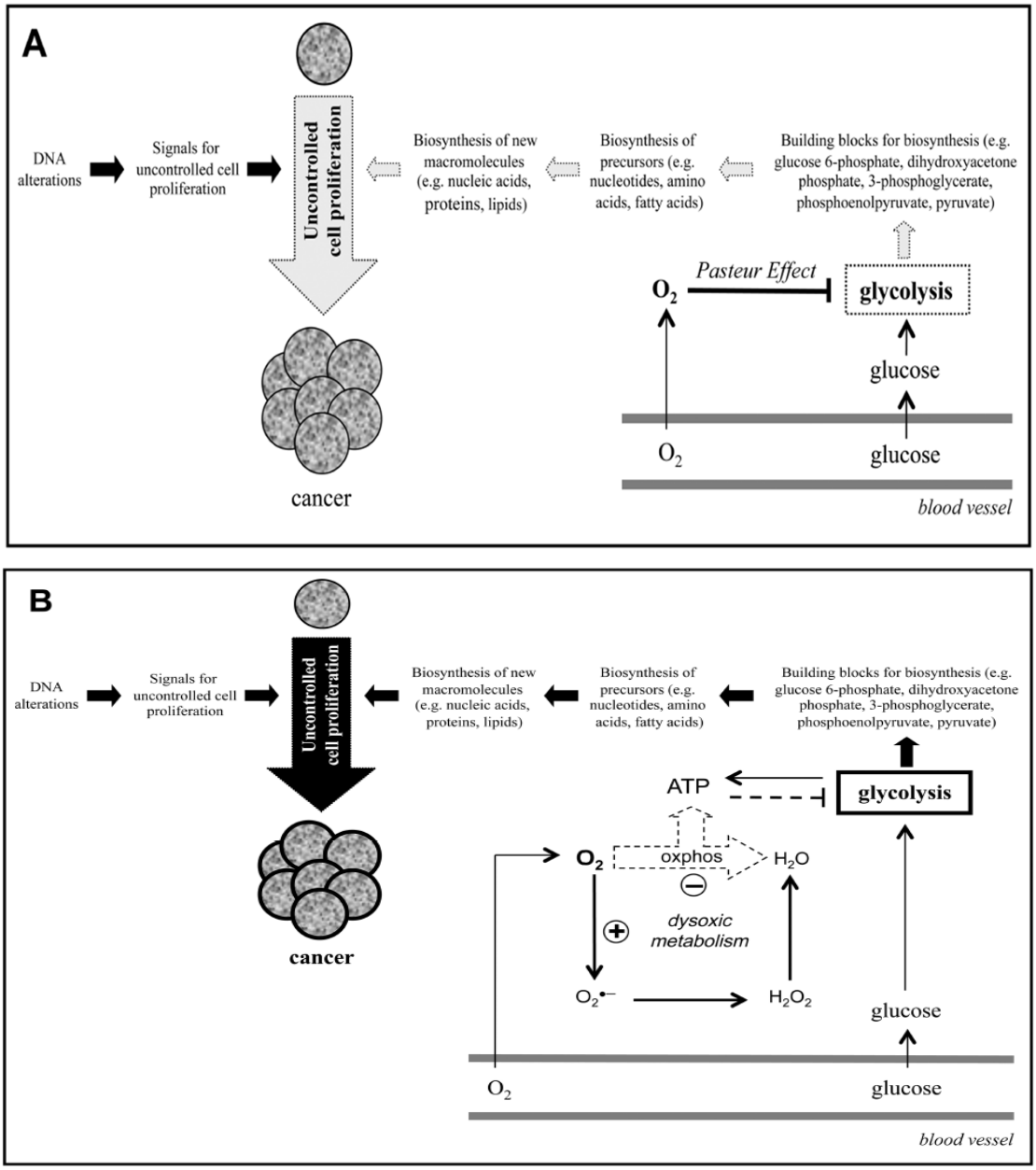

Figure 2.27 Uncontrolled cell proliferation for cancer development requires DNA mutations and (A) Nutrients from the blood for biosynthesis of macromolecules (B) Cancer alters the oxygen metabolism to activate glycolysis in the presence of oxygen. Reprinted by permission from Elsevier: Microelectronic Engineering [49], copyright (2010)

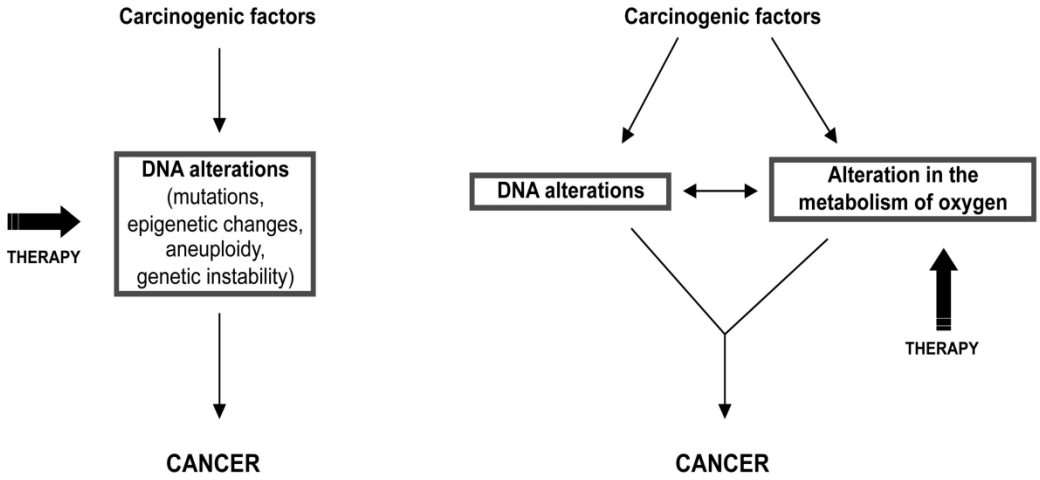

Figure 2.28 Alterations to DNA and oxygen metabolism interact to develop cancer. Instead of targeting (A) complex DNA alterations (B) oxygen metabolism alteration is simple and reliable. Reprinted by permission from Elsevier: Sensors and Actuators A: Physical [49], copyright (2010)

2.3.2 Tumor Invasion and Metastasis

Cancer is marked by uncontrolled cell proliferation, tumor formation and invasion to nearby parts of the body. Cancer cells can migrate from the original site to a distant part of the body to grow secondary tumor and this process of transmission of cancerous cells is called metastasis. A complicated series of tumor-host-interactions are carried out before a metastatic colony is established as explained in Figure 2.29. Primary tumor cells get access to host blood vessels and lymphatics in result to their local invasion. They enter the blood stream and are carried to remote organs to initiate a metastatic colony followed by angiogenesis [53].

Metastasis is the major cause of deaths for cancer patients but its mechanism is still not completely understood [54]. Metastasis involves numerous molecular interactions within tumor's microenvironment during primary tumor progression to the growth of macrometastases. The invasive tumor has to interact with extracelluar matrix at many stages during metastasis. It

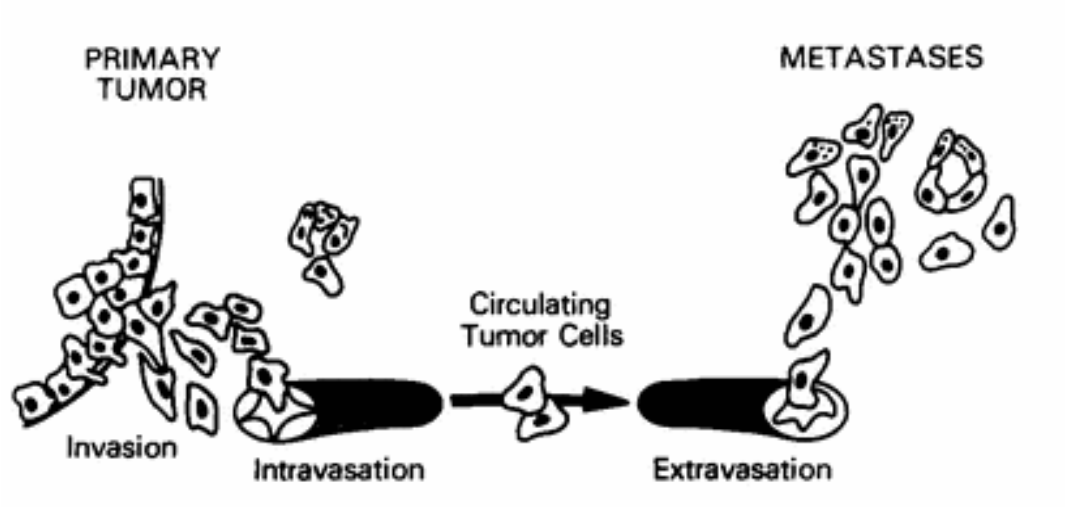

Figure 2.29 Schematic demonstration of multistep tumor-host-interactions during metastasis. Reprinted by permission from Springer: Springer eBook [53], copyright (1989)

plays an important role during invasive tumor progression. Tumor cell invasion of extracelluar matrix has been illustrated in Figure 2.30. It starts with specific binding to the matrix followed by local degradation of matrix and the binding components due to the secreted hydrolytic enzymes. The third step is the locomotion of tumor cell into the matrix region modified by proteolysis.

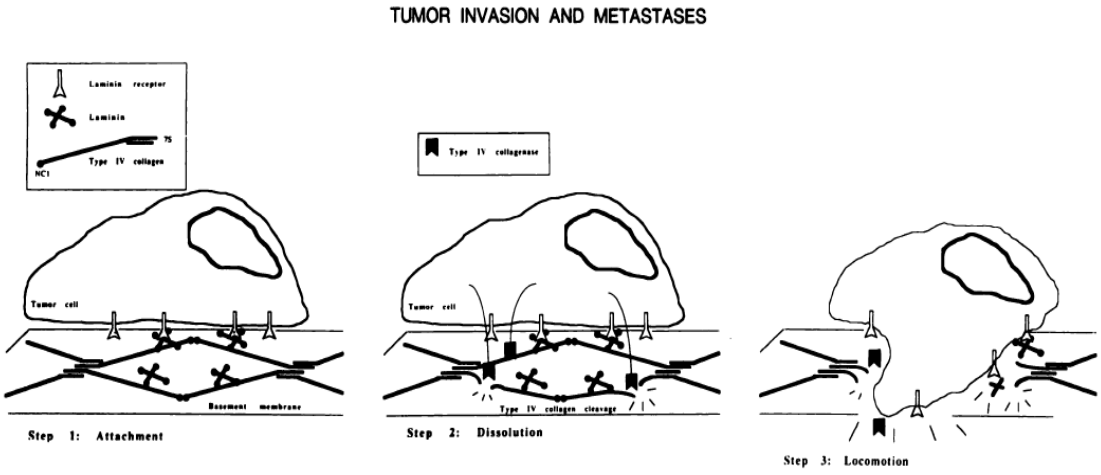

Figure 2.30 Tumor cell invasion of extracellular membrane. Reprinted by permission from American Association for Cancer Research: Cancer Research [55], copyright (1986)

Epithelial cells which play very important structural and functional role in body organs are attached with each other by cell-to-cell adhesion molecules (cadherins). They are also extensively attached to cell-to-extracellular matrix (ECM) junctions by cell-to-ECM adherent molecules (integrins). Cadherins and integrins rely on rigid structure (cytoskeleton) so normal epithelium cells are rigid and immobile. Whereas mesenchymal cells like leukocytes and fibroblasts, have very flexible organization. Tumor cell invasion involves transition from epithelial to mesenchymal cells (EMT). This transition is marked by degradation of cell-to-cell adhesion, decline in E-cadherins expression, decrease of epithelial markers (cytokeratin) and increase of mesenchymal markers (vimentin). Mesenchymal-like cancer cells show high motility and can easily intravasate and extravasate by traversing basement membrane, interstitial gaps and endothelial barriers. After entering blood vessels (intravasation), circulating tumor cells (CTC) go through apoptosis or circulate as isolated CTC and cannot proliferate in the blood vessels. After reaching the target, the cancer cells reverse to epithelial-like ells through mesenchymal to epithelial transition (MET) so that they can again start cell proliferation which is hallmark of cancer [56, 57]. Figure 2.31 shows all these steps involved in tumor invasion and metastasis.

2.3.3 Circulating Tumor Cells (CTCs)

When Cancer cells detach from the primary tumor and enter the circulatory system, they are called circulating tumor cells (CTCs). The CTCs flow in the peripheral blood vessels with other cells. CTCs may lead to subsequent growth of additional tumors in secondary tissues. The presence of CTC was first discovered by Ashworth in 1869 [58]. CTCs are critically important in clinical diagnostics. Detection and exact quantification of CTCs not only help early diagnosis but also improve prognosis for cancer patients. In several reports, the presence of CTCs is responsible for most of the cancer-related deaths [59, 60]. The number of CTCs in per ml of blood is also associated with the survival rate of cancer patients so precise enumeration of CTCs can indicate the therapeutic efficacy and improve the survival rate of cancer patients. In

one report, breast cancer patients who had less than 5 CTCs per 7.5 ml of blood survived for 7 months on average; whereas patients with 5 or more CTCs per 7.5 ml of blood could survive for only 2.7 months. The overall survival periods in these two groups were 10.1 month and 18 months respectively [61]. Several types of cancers (renal, breast, prostate) have been recognized to have CTCs in patient's peripheral blood [62-68].

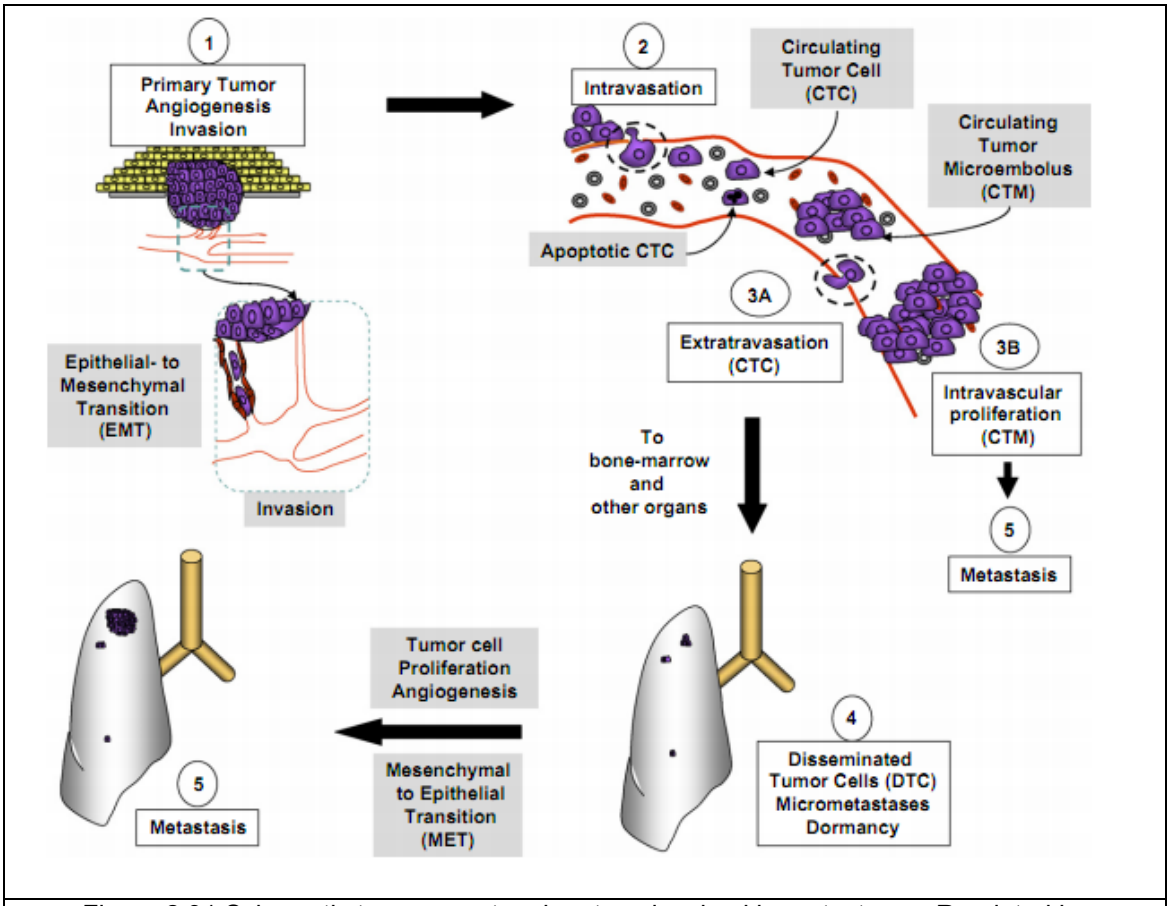

Figure 2.31 Schematic to represent major steps involved in metastases, Reprinted by permission from Elsevier: Cancer Letters [69], copyright (2007)

2.3.4 CTCs Detection Schemes

Extensive efforts have been made for efficient detection of circulating tumor cells (CTCs) from the peripheral blood [69-73]. Efficient detection and precise quantification of CTCs is highly challenging since the CTCs are very low in number ranging 1–100 per ml of peripheral

blood [74-79]. Whereas 1 ml of blood contains an average of approximately 10^6 white blood cells (WBCs) and 10^9 red blood cells (RBCs) [80]. Current CTC detection models are either limited by the low throughput or the use of fluorescent tags for cell quantification. Some of the methods are laboratory dependent and require expensive equipment. Figure 2.32 illustrates the current approaches for CTC isolation and detection [81]. Most frequently used detection methods for the isolation and characterization of CTCs have been briefly described in the following sections.

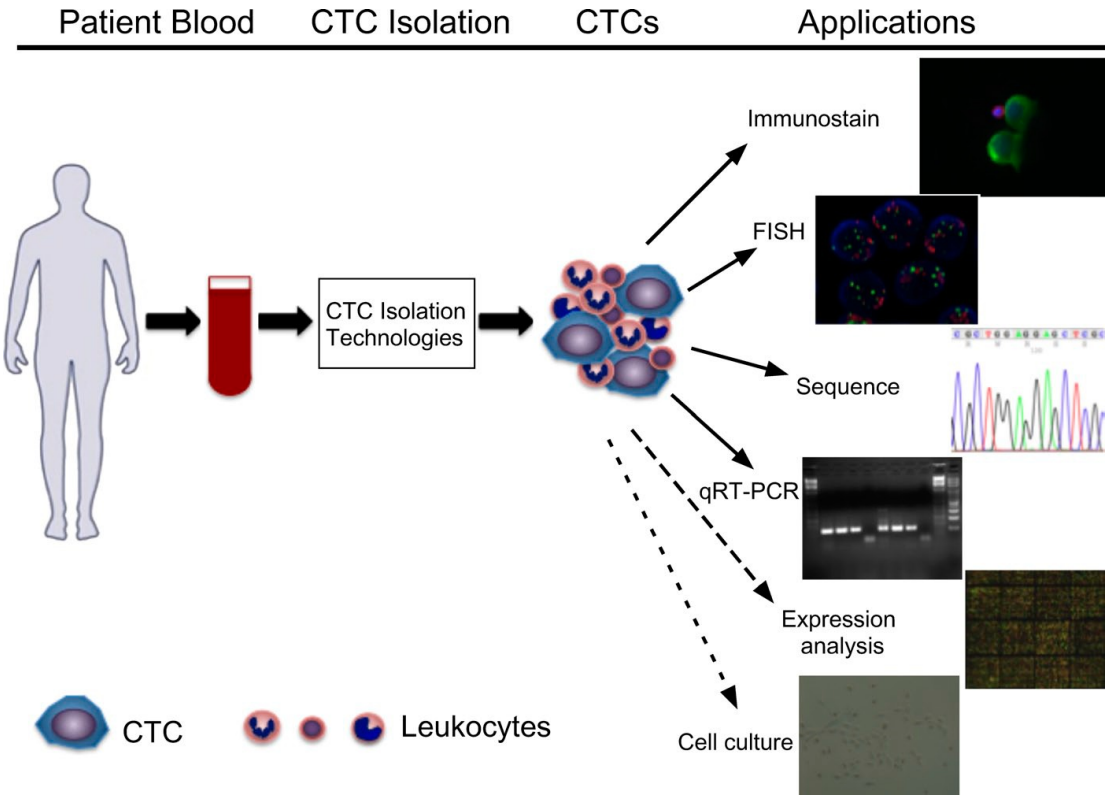

Figure 2.32 Current CTC detection technologies. The peripheral blood from cancer patients is processed by different techniques to isolate CTCs and then various biomarkers are exploited for CTC detection. Printed with permission by The Rockfeller University Press: The Journal of Cell Biology [81], copyright (2011)

2.3.4.1 Immunomagnetic Detection

In immunomagnetic detection systems, magnetic particles (beads or ferrofluids)-bound antibodies are mixed with whole blood or isolated mononuclear cells [82-85]. The mononuclear cells are usually isolated using density gradient and centrifugation. Target cells get attached to the beads due to the specific binding of antibodies and are retrieved using a magnetic field. A large number of leukocytes are still present with the target cells collected from whole blood. CTCs are recognized by cellular morphology, irregular size and shape of nucleus, over-expression of cytokeratins and lack of CD45 expression [86]. Some immunomagnetic systems recognize leukocytes by including negative selection of leukocytes with anti-CD45 antibody combined with positive selection of epithelial cells specific antibodies like EpCAM and cytokeratins [86]. Immomagnetically enriched epithelial cells solution may contain non-malignant epithelial cells and may drop the malignant tumor cells which do not express epithelial antigens. Figure 2.33 shows cancer cells isolated from whole blood using immunomagnetic beads.

2.3.4.2 CellSearch method

The CellSearch^{TM} assay is a commercially recognized system for CTC detection. In this method, ferrofluids coated with EpCAM antibody are used for immunomagnetic isolation of epithelial cells. After separation and immobilization, cells are labeled with different dyes including fluorescent nuclear dye (DAPI), a fluorescent antibody (anti-CD45) specific to leukocytes and fluorescent antibodies for cytokeratin specific to epithelial cells [87]. Finally the sample is analyzed using a Cell-Spotter Analyzer which is a fluorescent microscope used for epithelial cells differentiation from other cell types based on fluorescent colors [88]. Keratin reactivity is typical of epithelial cells whereas CD45 is a common antigen for leukocytes.

Antibodies specific to these two antigens are collectively used for mutually exclusive expression in diagnostics where anti-CD45 is used for negative selection of CTCs [89].

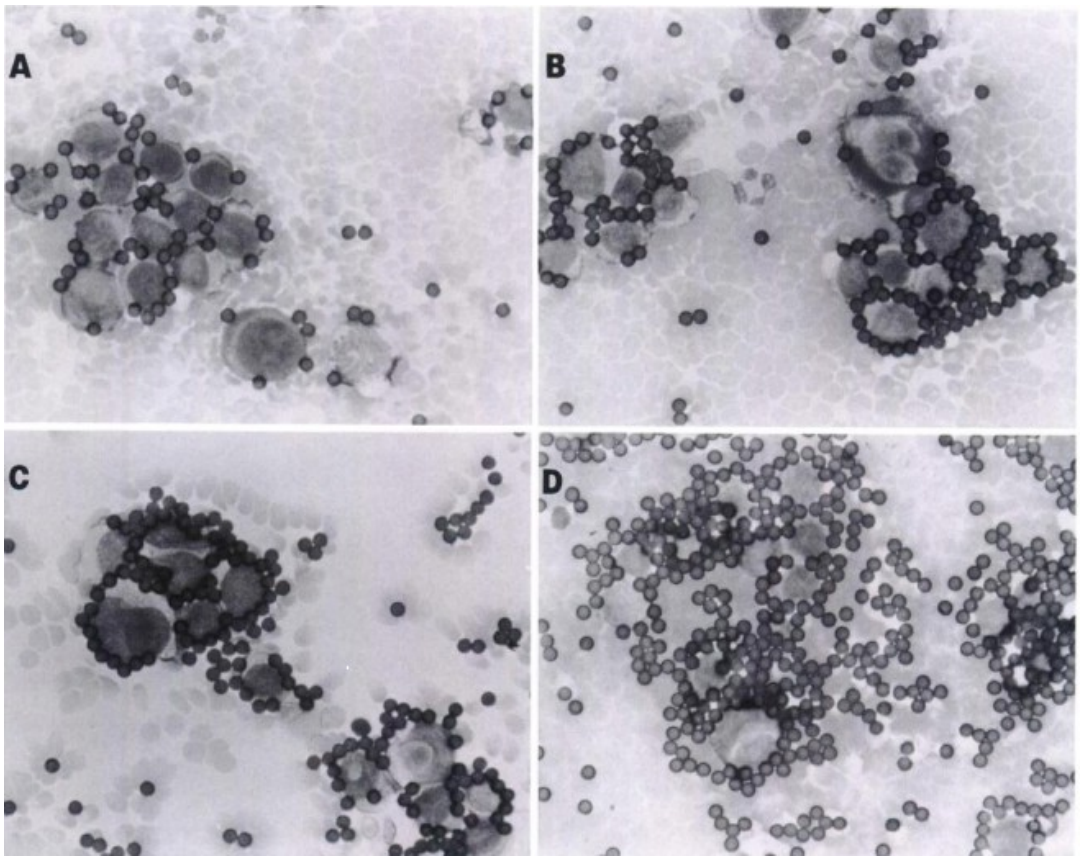

Figure 2.33 Varying concentrations of magnetic beads (increasing for A-D) incubated in whole blood carrying cancer cells. The beads bind to tumor cells. Reprinted with permission by American Association for Cancer Research: Cancer Research [85], copyright (1993)

2.3.4.3 Reverse Transcription Polymerase Chain Reaction (RT-PCR)

RT-PCR is a molecular diagnostic method that makes use of ribonucleic acids (RNA) for CTC detection. In this method, sample is first enriched with epithelial cells followed by extraction of RNA. Reverse transcript of RNA is used to get complementary DNA which is amplified by polymerase chain reaction (PCR) to get the diagnostic PCR product for tumor cell identification

as shown in Figure 2.34. RT-PCR is highly sensitive and can recognize one cancer cell from 1-10 million normal cells [70]. The salient feature of this technique is its sensitivity which is considered extremely high as compared to other CTC detection systems. But this extreme sensitivity induces the tendency for false positives resulted from physical contaminations. Moreover, the approach doesn't provide quantifiable data for the blood samples [90, 91].

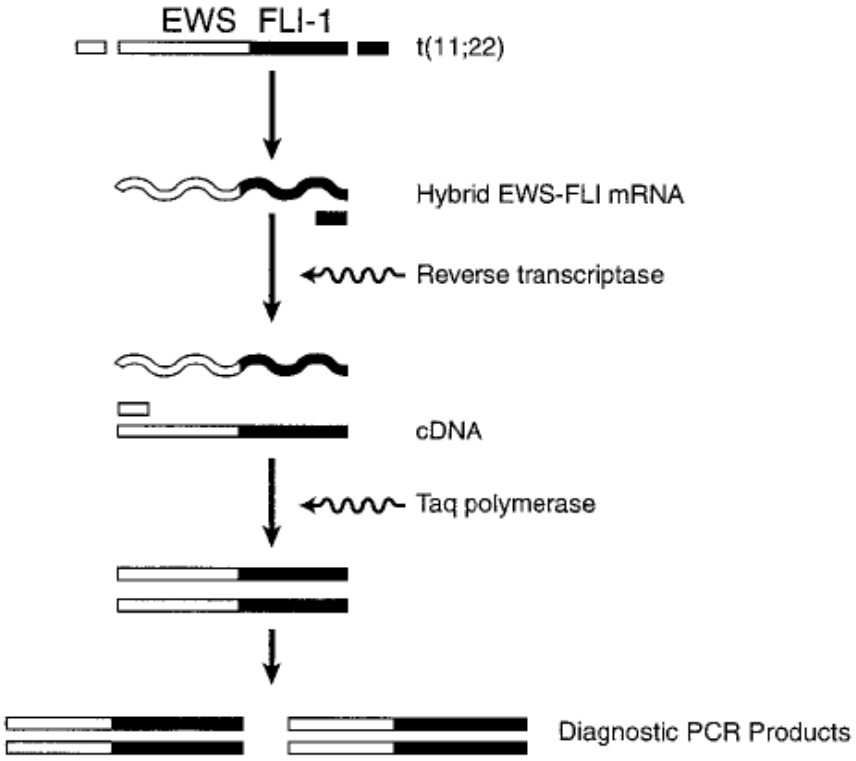

Figure 2.34 Schematic demonstration of RT-PCR amplification of tumor-specific microRNA for CTC detection. Reprinted with permission by American Association for Cancer Research: Clinical Cancer Research [70], copyright (1999)

2.3.4.4 Size Based Isolation of CTC

Isolation by Size of Epithelial Tumor cells (ISET) is very simple and straightforward strategy for CTC detection. It relies on the relatively larger size of epithelial cells as compared to other cells present in the peripheral blood. In this method, the blood is diluted with the buffer

and filtered through a polycarbonate membrane with the average diameter of 8 μm. The larger size of epithelial cells prevents them to pass through the 8 μm membrane pores so they are isolated from leukocytes after filtration [92, 93]. The cells are fluorescently labeled and scanned with laser cytometry for molecular characterization of tumor cells. The diameter of cancer cell found in the breast cancer patient lies in the range of 29.8 μm to 33.9 μm which is higher than that of leukocytes. The breast cancer cells have been successfully isolated using ISET technique with a recovery efficiency of about 85% [92, 94]. White blood cells (WBCs) have an average diameter in the range of 7 to 20 μm so all of them are not smaller than 8 μm which grounds for finding some WBCs left on the polycarbonate membrane with the target cells as shown in Figure 2.35. Though size-based separation is a very simple approach but entails with laser scanning for post analysis.

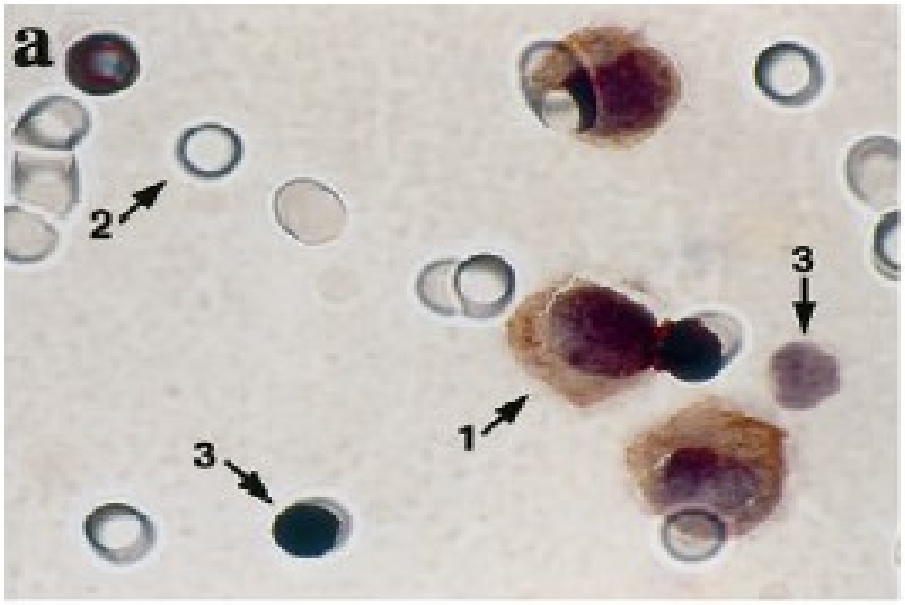

Figure 2.35 Immunocytochemical analysis of CTCs using ISET method where large size tumor cells remain on polycarbonate membrane after filtration. Arrows represent (1) cancer cells (2) membrane pores (3) leukocytes. Reprinted with permission by Elsevier: The American Journal of Pathology [93], copyright (2000)

2.3.4.5 Surface Functionalization for CTC Detection

Microchip-based systems and microfluidic devices are also used for CTCs detection. Recently, a microchip-based detection system has been developed which contained an array of microposts functionalized with EpCAM antibodies which are selective to epithelial cells [95]. When the whole blood was allowed to flow through the microposts under precisely controlled laminar flow conditions, selective binding of antibodies with the epithelial cells occurred as shown in Figure 2.36. They identified CTCs from peripheral blood of patients with metastatic cancer of various types including lung, prostate, breast and colon cancers. They successfully identified CTCs from peripheral blood of 115 out of 116 cancer patients. This approach gave high detection efficiency but involves surface functionalization for cell capture and fluorescent tags for post identification of captured cells.

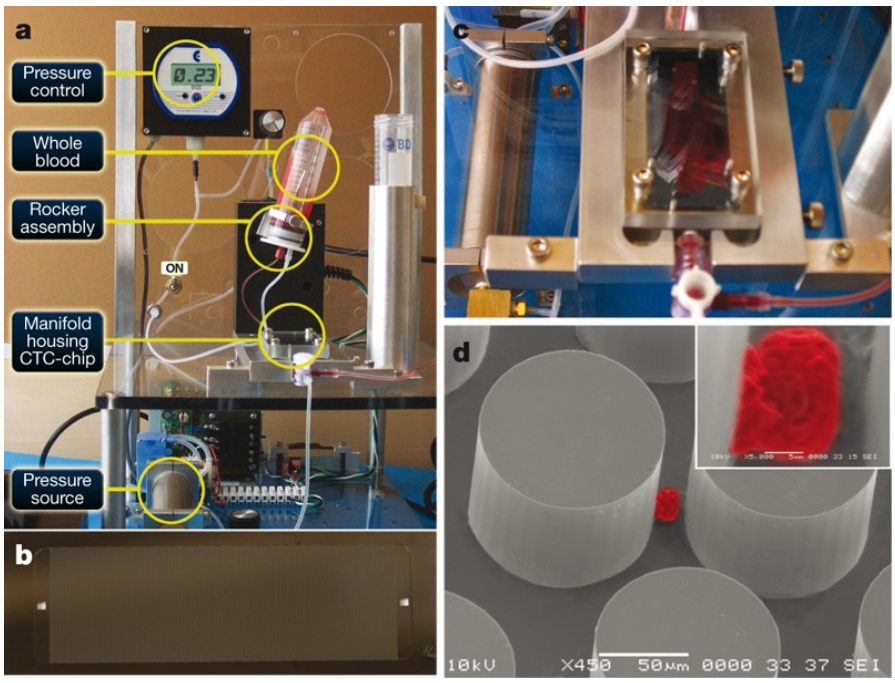

Figure 2.36 Experimental setup for CTC detection from blood using functionalized microposts. Reprinted with permission from Nature Publishing Group: Nature [95], copyright (2007)

2.4 Polymeric Nanoparticles for Controlled Drug Delivery Applications

2.4.1 Controlled Release Systems

Conventional cancer treatment mainly relies on chemotherapy and radiations to kill the cancerous cells. The effectiveness of the therapy is directly related to its capability of targeting and killing tumor cells while affecting as few healthy cells as possible [96]. Within current clinical settings, most of the patients observe side effects which sometimes get so intense that patients must stop therapy before the drugs have a chance to eliminate the tumor [97]. Research efforts are in progress to find new therapeutic agents and to find new ways of delivering these bioactive agents in a controlled fashion. So controlled drug delivery systems are much needed to elevate the cancer drug therapy and consequently the patient's life expectancy.

Controlled release systems incorporate both controlled release over an extended period of time and targeted delivery specific to tumor cells only. A sustained delivery over days/weeks or months is highly recommended for the drugs which are rapidly metabolized and eliminated from body after administration. The drug delivery targeted to specific site is very useful when drug involves the healthy cells and causes intense side effects. All controlled delivery systems seek to improve the therapeutic efficacy of the drugs. This improvement may be in the form of enhanced therapeutic activity as compared to the side effects or reduced drug administration frequency during the treatment [98]. The key objective of such systems is to maintain the concentration of drug in therapeutic window for all the time during treatment. Therapeutic window refers to the amount of drug that provides optimum therapeutic activity without any harmful side effect. Figure 2.37 and 2.38 demonstrate the two forms of controlled release systems. Controlled release formulations can be used to reduce the amount of drug needed to induce the same therapeutic effect at tumor site. Fewer but more effective doses not only help to evade wastage of drug but also increase patient compliance [99]. In many of the controlled release systems, an initial burst of drug release occurs which may cause overdosing in some

cases but in several cases, it is a desired feature of the release formulation so that drug concentration may get to therapeutic window quickly [100]. Various systems ranging from coated tablets to biodegradable polymeric micro/nanoparticles have been developed for controlled release applications.

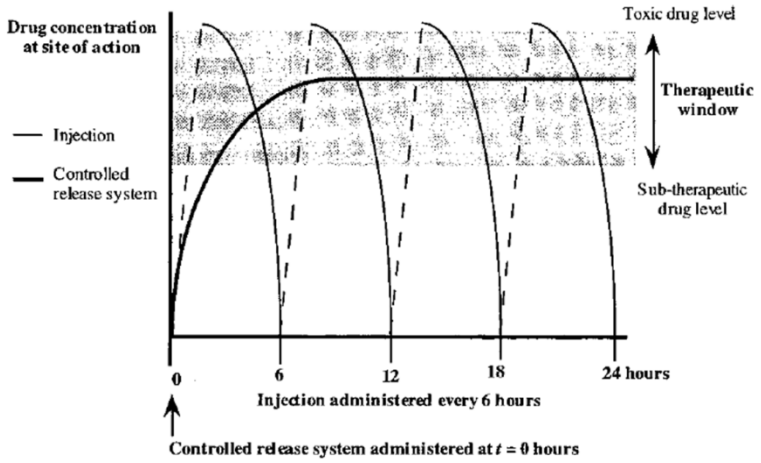

Figure 2.37 Controlled release system to deliver therapeutic drug over extended time eliminates the need of periodic administration. Reprinted with permission from American Chemical Society: Chemical Reviews [98], copyright (1999)

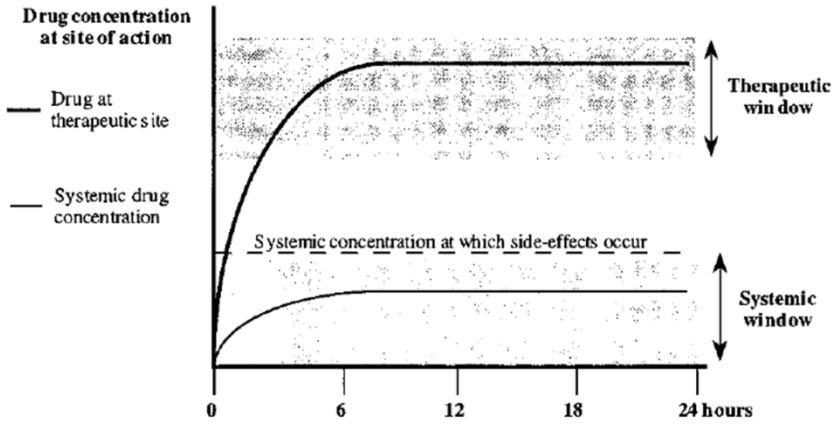

Figure 2.38 Controlled release system improves therapeutic activity. Reprinted with permission from American Chemical Society: Chemical Reviews [98], copyright (1999)

2.4.2 Drug Loaded Polymeric Nanoparticles

Several disease-related drugs or bioactive agents have been successfully encapsulated in polymeric nanoparticles to improve the bioavailability and control over release kinetics [101-103]. Nanomedicines for dreadful diseases like cancer aim to develop polymeric drug release systems which provide maximum encapsulation, improved therapeutic activity and retention time [104, 105]. The efficiency of these polymeric systems is strongly coupled with the particle size, surface charges and molecular weight of the polymer. The size of nanoparticles determines their interactions with the cell membrane and their penetration across physiological drug barriers; surface charges define the cellular internalization of these nanoparticles whereas molecular weight modulates the release mechanism [96, 106, 107].

Biodegradable polymeric nanoparticles have been widely used for nanoencapsulation of various therapeutic drugs and bioactive molecules to develop nanomedicines. Such an extensive use of these nanoparticles as drug carriers is due to their controlled/sustained release behavior, biocompatibility with tissues and cells, subcelluar size for better internalization, biodegradability and *in vivo* stability [108]. Biodegradable nanoparticles are classified as nanocapsules or nanospheres depending upon the structural organization [109] and the drug molecules are either entrapped inside or adsorbed on the surface of these nanovehicles as shown in Figure 2.39. Different types of nanomedicine formulations have been developed for controlled drug release using biodegradable polymers. Drug release mechanism of such controlled delivery systems is formulated according to the needs of its application and the type of drug encapsulated [110]. The controlled/sustained release behavior is usually achieved by slow erosion of polymer matrix or restricted diffusion of drug molecules to the biological aqueous environment surrounding the drug delivery system. Moreover, devices with semi-permeable polymer membrane are also used to control the flow of drug solution under osmotic potential gradient as illustrated in Figure 2.40. Hence, polymer characteristics play a significant role in controlled delivery systems and should be carefully selected.

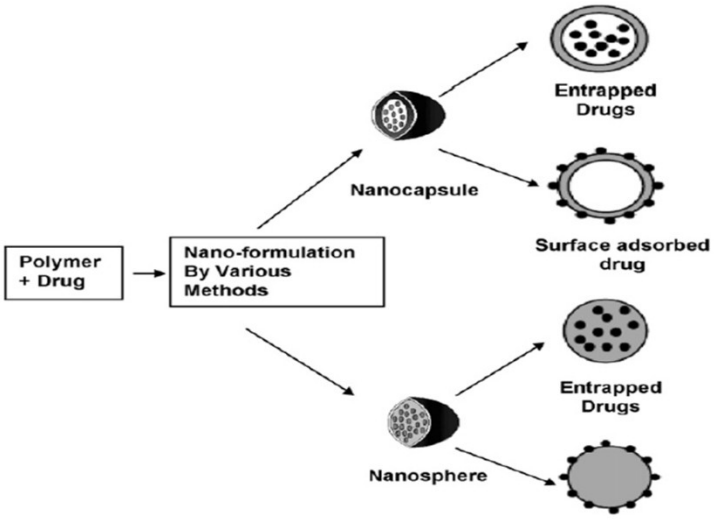

Figure 2.39 Synthesis and encapsulation of drug in polymeric nanoparticles. Reprinted with permission from Elsevier: Colloids and Surfaces B: Biointerfaces [110], copyright (2010)

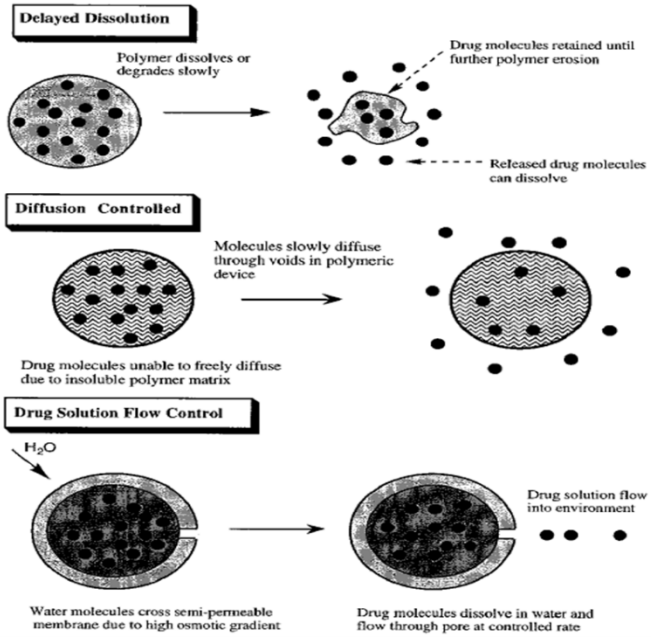

Figure 2.40 Different types of drug release mechanisms for controlled delivery. Reprinted with permission from American Chemical Society: Chemical Reviews [98], copyright (1999)

2.4.3 Poly(lactic-co-glycolic acid) (PLGA)

PLGA is one of the most extensively used polymers for the development of nanomedicine. It is biocompatible, biodegradable, non-toxic, noninflammatory and nonimmunogenic in living environment which lays the foundation for its broad acceptability to biomaterial and nanomedicine applications. PLGA is biologically hydrolyzed in acidic medium inside the body and gives two biodegradable metabolite monomers; glycolic acid and lactic acid as shown in Figure 2.41 [110]. Since body is known to successfully deal with these two monomers so no immune response is activated. So, minimal systemic toxicity is associated while using PLGA for drug delivery applications.

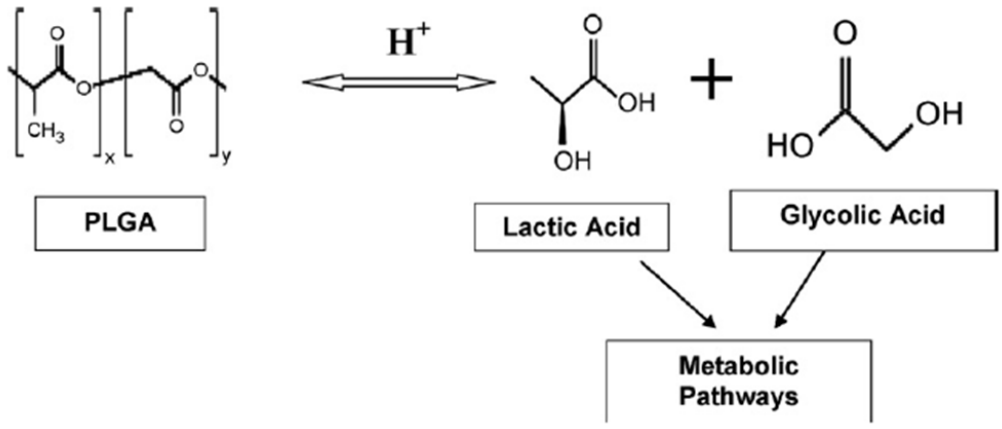

Figure 2.41 Biological hydrolysis of PLGA produces lactic acid and glycolic acid which are metabolite monomers. Reprinted with permission from Elsevier: Colloids and Surfaces B: Biointerfaces [110], copyright (2010)

PLGA has also been approved by Food and Drug Administration (FDA) for therapeutic use in humans. Therefore, PLGA nanoparticles have been widely used to encapsulate various anti-cancer drugs for cancer treatment. The nanoparticles protect the unstable drugs loaded into these nanocarriers from the biological surroundings and their small size facilitates them with capillary penetration and endosomal escape [111, 112]. Furthermore, the high surface area

offered by nanoparticles makes them exceedingly effective for targeted delivery of payload to tumor cells or other tissues [113].

2.4.4 Synthesis of PLGA Nanoparticles

PLGA nanoparticles are mostly prepared by emulsion diffusion, solvent evaporation, interfacial deposition or nanoprecipitation methods [107, 114-116]. Emulsion diffusion method starts with dissolving PLGA polymers in an organic solvent followed by separation in aqueous phase. The aqueous phase contains a stabilizer and finally homogenized to get the nanoparticles. In solvent evaporation method, the PLGA polymers are dissolved in volatile organic solvents like methylene chloride, chloroform and acetone. The solution is then poured in a continuously stirring aqueous phase followed by sonication. The aqueous phase may or may not have stabilizer in solvent evaporation technique. For interfacial deposition, the nanoparticles are synthesized in the interfacial layer of water and the organic solvent. Sonication is used to separate the nanopraticles in this method of nanoparticles preparation. Nanoprecipitation is the most commonly used method for the preparation of PLGA nanoparticles. In this method, PLGA polymers are dissolved in a volatile organic solvent like acetone and the solution is added drop-wise into continuously stirring aqueous phase with stabilizer. Finally the organic solvent is allowed to evaporate at low pressure. Figure 2.42 explains the synthesis schemes for PLGA nanoparticles.

PLGA-based nanopraticles are bulk-eroding and generate acids during polymer erosion. These acids are neutralized by the bases in the release medium or human body fluids. Slow diffusional mass transport across the nanoparticles result into a low pH within the drug carriers [117]. Such a drop in pH may affect drug stability and accelerates polymer degradation due to the autocatalytic effects which are the major concerns in non-porous PLGA-based particles [118]. Porous drug delivery systems can overcome these autocatalytic effects by increasing the diffusivity of the molecules [119]. Thus, PLGA based porous nanoparticles can

be a much better carrier for controlled drug delivery systems. Porous nanoparticle systems also show better flow and aerosolization efficiency during pulmonary administration as compared to non-porous PLGA nanoparticles [120, 121]. Drug release kinetics are directly controlled by the pore characteristics of porous PLGA nanoparticles so by controlling the pore morphology, highly controlled drug release systems can be designed [122]. But synthesis of porous nanoparticles is relatively complex so a lot of research work has done for finding simpler and rapid approaches to synthesize porous nanoparticles.

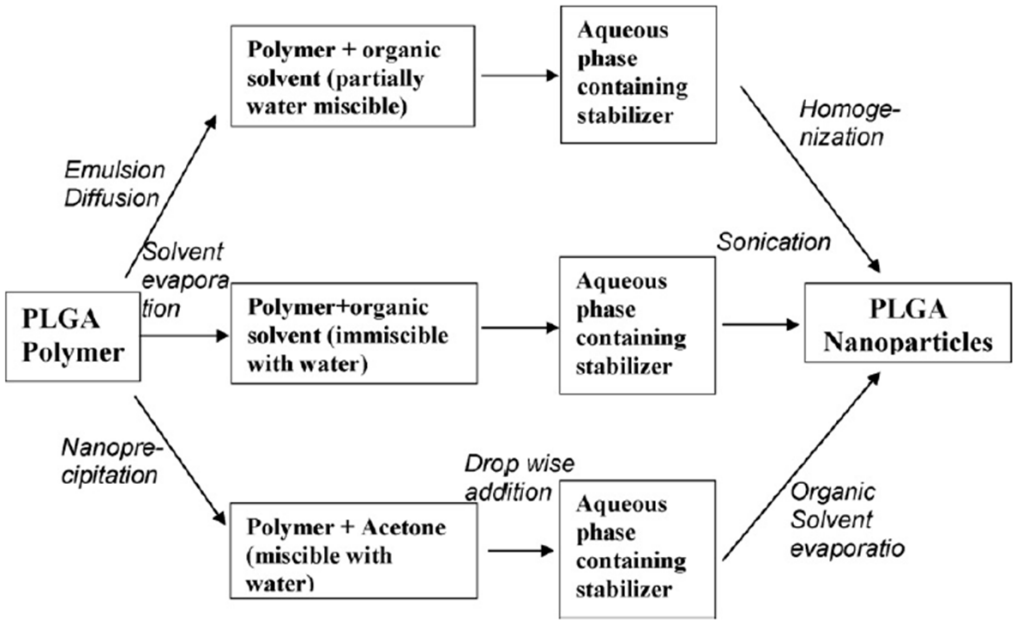

Figure 2.42 Schematic to represent different methods for the synthesis of PLGA nanoparticles. Reprinted with permission from Elsevier: Colloids and Surfaces B: Biointerfaces [110], copyright (2010)

2.4.5 Synthesis Techniques for PLGA Porous Nanoparticles

Various approaches have been developed to synthesize porous micro/nanoparticles which include the use of volatile pore forming agents or extractable polymers as porogen. Ammonium bicarbonate has been used as a gas foaming porogen which evaporates to give

porous features on the surface of particles [123, 124]. Zhao et al. used poly(acrylic acid) as the porogen which gave porous surface of the particles after thermal imidization [125]. In one of the reports, Pluronic F-127 polymer has been used as the extractable porgen to prepare porous particles [126]. Most of these methods are either limited by the physiochemical properties of the porogen or the need for thermal curing. Porosity is a direct function of the porogen concentration so just by varying the porogen concentration; porosity of the particles can be manipulated to achieve the ideal drug release kinetics as shown in Figure 2.43 [123, 126]. Thus, porous nanoparticles can be used as efficient drug carriers in controlled drug delivery systems.

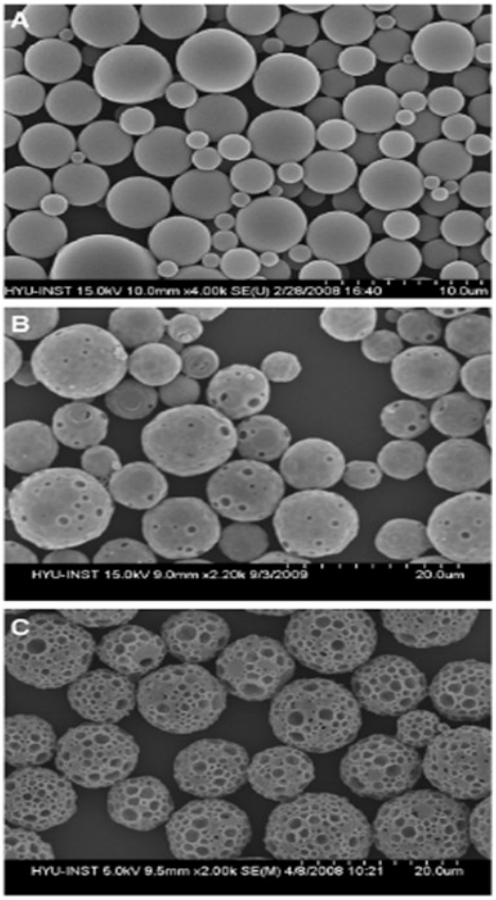

Figure 2.43 PLGA porous particles with varying (increasing A to C) concentrations of porogen show that porosity varies directly with porogen concentration. Reprinted with permission from Elsevier: Journal of Controlled Release [123], copyright (2011)

CHAPTER 3

NANOGAP BREAK JUNCTIONS FOR MOLECULAR DETECTION OF CANCER

3.1 Introduction

Recent advancement in the field of molecular diagnostics has facilitated better understanding of disease progression establishing new biomarkers for early diagnosis, appropriate treatment and faster drug breakthroughs. Epidermal Growth Factor Receptor (EGFR) protein is considered to be involved in several types of cancers and has been reported as a common biomarker for many cancers like breast cancer [127], lung cancer [128], cervical cancer [129], bladder cancer [130], esophageal cancer [131] and ovarian cancer [132]. The presence of a biomarker in some specimen can point out threats for the disease, specify the phase of that disease and enable us to figure out some irrefutable way to monitor changes to homeostasis [133]. Therefore the early detection of EGFR over-expression can dramatically improve treatment and prognosis for the patients.

Various approaches have been reported for the detection of EGFR and its interactions. These techniques incorporate immunohistochemical [134], flow cytometric [135], amperometric [136], mechanical [137] and optical [138, 139] detection modalities. These methods of detecting proteins are generally categorized as labeled detection and label-free detection methods. In the case of labeled detection methods, presence of proteins is confirmed by some secondary molecule (organic, inorganic or radioactive) that binds to the proteins. Optical detection utilizes a fluorescent tag attached to the proteins and the change in fluorescent intensity after binding signals the presence of proteins. Whereas electrical detection directly interrogates the presence and electrical conductivity of protein molecules but entails efficient device fabrication in order to

define contact structures with a molecular dimension separation so that transport properties of single molecules may be studied.

A variety of metal-molecule-metal structures have been developed for measuring electrical conductivity through molecules [2]. Metal-molecule-metal structures can be broadly classified as vertical device structures (VDS) and lateral device structures (LDS). VDS utilize a self-assembled monolayer of molecules grown on a metal surface and second contact is made through conductive probe atomic force microscopy [140], crosswire [141] or scanning tunneling microscopy [142]. Whereas LDS involves a pair of metal contacts with nanometer sized separation and the probes selective to protein molecules are immobilized between the contact structures. Such devices that contain a thin metal strip, in that a gap is created by some technique, are known as break junctions. This gap can be formed through e-beam lithography [143], mechanically controlled break junctions [7], electrodeposition [144] and electromigration induced break junctions [10, 145]. Most of these techniques either are slow and costly, mainly because of e-beam writing or face lower yield of functional devices. Herein, we present a detection model for EGFR molecules by making use of a new class of break junctions where a focused ion beam (FIB) is used to scratch a thin metal strip, followed by conventional microscale probing and electromigration in order to produce break junctions with high throughput, greater yield, low cost and at exact spot, as reported before [146].

Previously, antibodies have mostly been used to functionalize nano devices that were used for biomarker detection. These antibody-based devices are not capable of performing well for field-deployable or point-of-care modalities because antibodies require specific temperature, humidity and low ionic strength of the buffer solution in order to retain their function [147]. Low ionic strength is necessitated to prevail over surface Debye screening but it causes poor interaction between target and surface probes [147]. Recently researchers showed significant effort towards introducing aptamers against several vital biomarkers [16, 148]. Aptamers are

reported to be as selective and sensitive as antibodies and are exceedingly stable over changing temperature, humidity and ionic concentration [14].

Elevated levels of EGFR in the serum of lung cancer patients have been reported before. The normal EGFR concentration can be in the range of 45-78 ng/ml, whereas it may be as much as an order higher in the lymph node metastasis of lung cancer patients (850 ng/ml) [149, 150]. The early detection of a few hundreds of ng/ml EGFR can be important to improve the prognosis of the patients. We have developed an economical and faster detection model that uses a new class of nano-electrode manufacturing and detects low concentration EGFR proteins (50 ng/µl) binding to RNA aptamers. The effective attachment of RNA aptamers on a chemically modified silicon dioxide (SiO_2) surface and protein binding to RNA was indicated by direct current electronic measurements. Figure 3.1 shows a cross-sectional sketch of the electronic biosensor that depicts the detection mechanism of the transduction. Attachment of RNA to SiO_2 surface and RNA-protein complex interactions were also verified through optical measurements before deploying the surface chemistry on the actual devices.

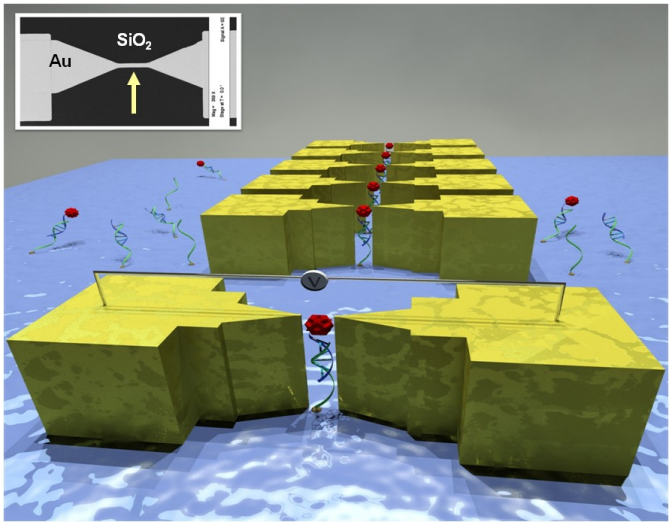

Figure 3.1 Schematic of the device that demonstrates the mechanism of the electronic detection (not to scale). Inset shows an SEM micrograph of the thin Au line on SiO_2 chip where arrow points out the prospective location for nanogap to be induced.

3.2 Materials and Methods

3.2.1 Chemicals

All the chemicals were purchased from Sigma-Aldrich (St. Louis, MO, USA) unless noted otherwise. The chemicals used for this work were 3'-aminopropyltriethoxysilane (APTES); 1,4-phenylenediisothiocyanate (PDITC); ethanol, isopropyl alcohol (IPA); acetone; dimethyl sulfoxide (DMSO); Pyridine; 6–amino–1–hexanol; N,N-Dimethylformamide (DMF); N,N-Diisopropylethylamine (DIPEA); phosphate buffered saline (PBS); magnesium chloride; hybridization buffer solution and diethylpyrocarbonate (DEPC) treated de-ionized water (DIW).

3.2.2 Methods

The presented work included three significant sections that were accomplished autonomously. The first section involved the fabrication of nanogap break junctions. The second step elucidated the immobilization of selective probes (aptamers) on the SiO_2 substrates. The third and most important part demonstrated the protein binding and its optical/electrical detection.

3.2.2.1 Fabrication of Nanogap Metallic Break Junctions

A two-step photolithography process was carried out to define structures on SiO_2 substrate. The first layer patterned 3 μm wide lines of titanium/gold (thickness 50 Å/150 Å) using metal lift-off. The second step of photolithography defined 200×200 μm^2 aligned probing pads that were made of Ti/Au (thickness 100 Å/500 Å). Figure 3.2 shows a representative device after two step photolithography and lift-off process. A single wafer carries thousands of such devices after photolithography followed by lift-off process which dictates the rapid manufacturing of nanogap break junctions from these devices.

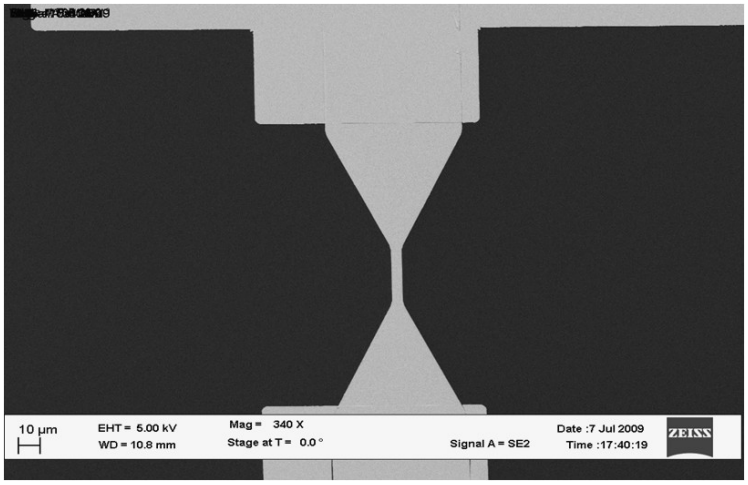

Figure 3.2 SEM micrograph of a representative device after two step photolithography followed by lift-off process.

The metal lined surface was partially scratched by FIB milling process to create the nanogap break junctions at precise locations. The FIB process depends on applied acceleration voltage, milling current and scratching time [151]. At higher milling current and scratching time, the entire gold layer got removed and also induced defects in SiO_2 layer beneath, rendering device un-usable. Secondly the higher milling current produced larger gaps as shown in Figure 3.3. FIB process was characterized to get optimal scratch in the metal line. FIB scratching with Gallium ions was done at 30 kV acceleration voltage, 1 pA milling current and 2 sec per micron scratching time in order to acquire optimum outcomes. Figure 3.4 shows an optimized FIB scratch that doesn't take away the metallic layer completely but only creates a defect in it for electromigration. The current-voltage (*I*-*V*) characteristics across the metal lines were determined using Agilent Semiconductor Parameter Analyzer (4155C) on a probe station. The *I*-*V* measurements before and after the nanomanufacturing of metallic break junctions were recorded to demonstrate the electromigration effect. A sweeping voltage was applied to induce the electromigration process. The applied bias should be just enough to produce the gap under electromigration and should be stopped right after the nanogap is generated. Figure 3.5 shows

a nanoelectrode device manufactured after electromigration which produces nanogap at the scratched location on metallic strip. The essential advantage of FIB scratching followed by electromigration is to overcome the uncontrolled and low yield manufacturing by conventional electromigration [6].

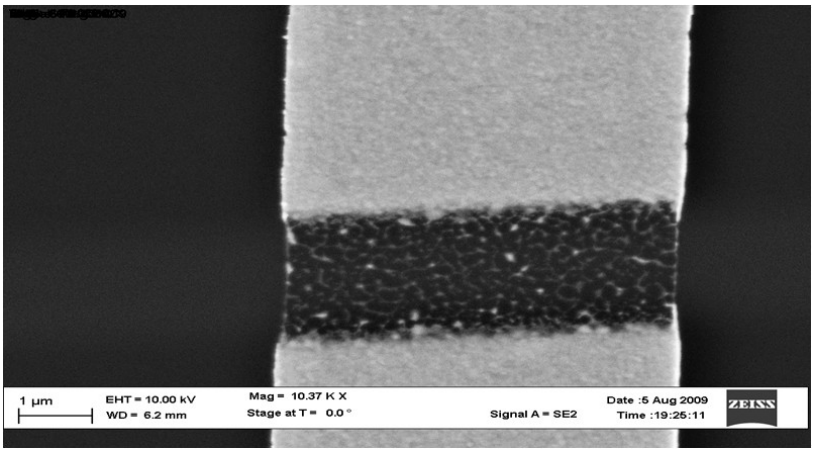

Figure 3.3 SEM micrograph of metallic strip after FIB milling at higher dose (30 KV applied voltage, 20 pA milling current and 120 secs of scratching time)

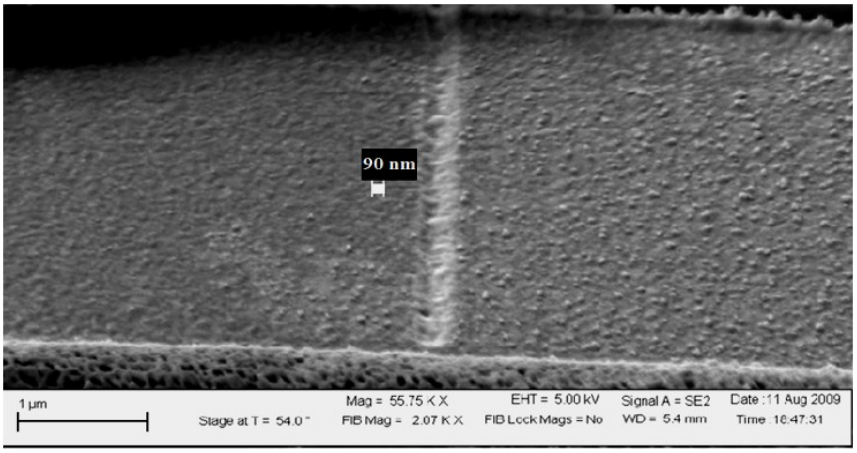

Figure 3.4 SEM micrograph demonstrates optimized FIB milling to create a fine scratch on metal line (30 KV applied voltage, 1 pA milling current and 30 secs of scratching time)

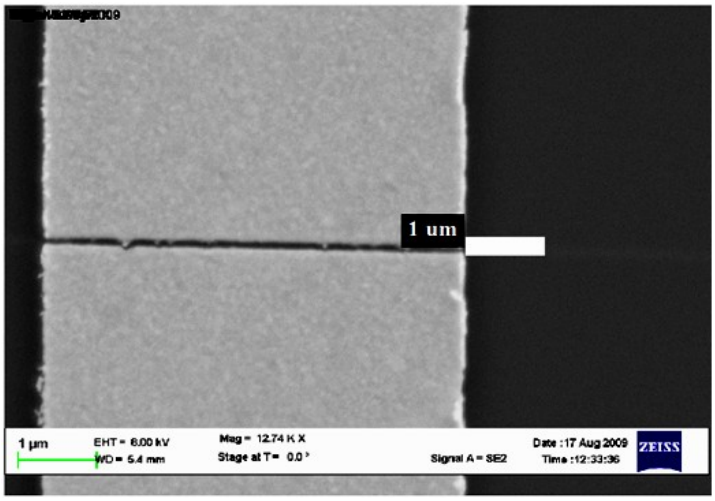

Figure 3.5 SEM micrograph of a representative break junction produced in result to electromigration

3.2.2.2 Preparation of Anti-EGFR Aptamers

Anti-EGFR aptamer was synthesized with a well-known process called “Systematic Evolution of Ligands by Exponential Enrichment” (SELEX) as reported before [15, 152]. An iterative selection of binding species against purified human EGFR (R&D Systems, Minneapolis, MN) was done to isolate anti-EGFR RNA aptamer [153, 154]. The high affinity (K_d = 2.4 nM) anti-EGFR RNA aptamer and a non-functional mutated aptamer were extended with a capture sequence. The extended anti-EGFR aptamer (5’-GGC GCU CCG ACC UUA GUC UCU GUG CCG CUA UAA UGC ACG GAU UUA AUC GCC GUA GAA AAG CAU GUC AAA GCC GGA ACC GUG UAG CAC AGC AGA **GAA UUA AAU GCC CGC CAU GAC CAG**-3’); extended mutant aptamer (5’-GGC GCU CCG ACC UUA GUC UCU GUU CCC ACA UCA UGC ACA AGG ACA AUU CUG UGC AUC CAA GGA GGA GUU CUC GGA ACC GUG UAG CAC AGC AGA **GAA UUA AAU GCC CGC CAU GAC CAG**-3’) and amino modified substrate-anchored probe oligonucleotide (5’-amine-CTG GTC ATG GCG GGC ATT TAA TTC-3’) were used. The capture sequence has been highlighted in bold font and underlined. The capture sequence was

used to modify anti-EGFR aptamer and the mutant aptamer by extending the DNA template at its 3' end with a 24-nucleotide sequence. The extended capture sequence didn't disrupt the aptamer structure but was used to immobilize aptamers on the surface through duplex-formation with the surface bound single-stranded DNA (ssDNA) probe molecules. The 5'-amine modified DNA strands were purchased from Alpha DNA (Montreal, Quebec).

3.2.2.3 Immobilization of Aptamers on SiO_2 Substrate

A thermally oxidized silicon wafer was diced into 4×4 mm^2 small chips in order to confirm the surface chemistry. The chips were initially cleaned in oxygen plasma for 15 minutes using $Ar+O_2$ at 200 W. This also resulted in a hydrophilic SiO_2 surface. The substrates were then immediately immersed in a solution of 2% APTES in ethanol for 1 hour at room temperature to get the surface silanized. The chips were then sequentially rinsed with IPA and DI water and then dried under nitrogen gas, followed by curing at 115^oC for 30 minutes. The chips were then submerged in a solution of 1 mM phenyldiisothiocyanate (PDITC) in DMSO containing 10% pyridine for 5 to 7 hours at 45^oC in order to get PDITC cross linker molecules attached onto the silanized surface. The chips were then washed sequentially with ethanol and DI water and dried in nitrogen flow. After that, the chips were allowed to incubate in a humidity chamber by placing 8 µl of amine modified ssDNA solution (5 µM concentration of DNA in DI water with 50% DMSO, 1% Pyridine) on each substrate for 16 to 18 hours at 45^oC to attach amino modified DNA to PDITC cross linker molecules. After ssDNA attachment, each chip was rinsed sequentially with ethanol and DEPC treated DI water and dried with nitrogen. The functionalized surface was then deactivated by capping unbound reactive groups of PDITC and submerging the chips in a blocking buffer solution that contained 50 mM 6-amino-1-hexanol with 150 mM DIPEA in DMF for 1 hour. The chips were then rinsed with DMF, ethanol, DEPC treated DI water and dried under nitrogen stream. After that, anti-EGFR RNA aptamer hybridization was carried out by incubating the chips in a buffer solution (100 nM concentration of anti-EGFR

aptamer with 5:1 DI water and Hybridization buffer solution) at 42^{o}C for 1 hour. The chips were washed thoroughly with DEPC treated DI water and dried with nitrogen gas. The anti-EGFR RNA aptamer had an extension that was hybridized with the surface bound complementary ssDNA. As controls, the mutant aptamer was hybridized to surface-bound ssDNA on separate chips using identical protocol. The presence of ssDNA and RNA aptamers immobilized on the SiO_2 surface was determined by fluorescence measurements of Acridine Orange stain at an excitation wavelength of 460 nm and the emission wavelength of 650 nm using Zeiss Confocal Microscope. Similarly, control chips with no aptamers were also prepared by performing all steps except aptamer hybridization.

3.2.2.4 Protein Binding and Electrical Detection

Chips with the attached RNA aptamer were then incubated in 50 ng/µl of EGFR protein prepared in phosphate buffered saline (PBS) with 5 mM Mg^{2+} solution at 37^{o}C for 45 minutes. The chips were washed thoroughly with PBS and DEPC treated DI water and dried under nitrogen flow. The chips were analyzed for the captured EGFR protein by optical detection of fluorescent Sypro Ruby Protein Blot stain at 488 nm wavelength. The fluorescence intensity analysis was done with ImageJ software. Briefly, the surface bound ssDNA was used to immobilize an anti-EGFR aptamer and subsequently the aptamer was used to capture the EGFR protein.

After confirming the attachment chemistry for RNA immobilization and selectivity of anti-EGFR aptamer on plain chips, electrical detection of EGFR protein was performed using nanomanufactured metallic break junction devices on SiO_2 substrate. Exactly identical attachment chemistry as described for plain chips was employed for these devices for protein detection. The electronic signatures of binding were measured with Agilent Semiconductor Parameter Analyzer (4155C) on a probe station. It recorded the direct current tunneling through

the nanometer scale electrode separation before and after the protein binding to the probing aptamers in between these nano electrodes.

3.3 Results and Discussion

3.3.1 Fabrication and Characterization of Nanoelectrodes

Optimal FIB scratches are obtained by employing the tuned dosage of FIB milling current, acceleration voltage and scratching time. The characterization of nanoelectrode manufacturing has been illustrated in Figure 3.6 and 3.7. The *I-V* data recorded after FIB scratching of the metal lines demonstrated a linear ohmic behavior that confirmed electrical and physical continuity of the metal lines (Figure 3.6(a)). A voltage sweep from 0 to 4V was applied to break the metal lines through electromigration phenomenon. Figure 3.6(b) shows a sudden drop in current that depicts an absolute separation between metal lines. The scanning electron microscope (SEM) micrographs also show a complete break in the metal lines with a nanometer scale separation. The inset to Figure 3.7(a) shows an estimated gap of 30-60 nm between the two electrodes. Figure 3.7(b) demonstrates the comparison of *I-V* data recorded for a representative break junction under same voltage (-1 to 1V) applied before and after the application of electromigration voltage. A tiny and random current flow observed after the electrode separation depicts only the tunneling current characteristics. The tunneling current in an arrangement of the nanogap electrodes having vacuum as the insulator between them can be approximated by the Simmons formula as

$$J = \left(\frac{\alpha}{\delta_z^2}\right)\left\{\bar{\varphi}\exp\left(-A\delta_z\sqrt{\bar{\varphi}}\right) - \left(\bar{\varphi}+eV\right)\exp\left[-A\delta_z\sqrt{\bar{\varphi}+eV}\right]\right\}$$

Where $\alpha = e/\left(4\pi^2\beta^2\hbar\right)$, $A = 2\beta\sqrt{2m/\hbar}$, $\bar{\varphi}$ is the average barrier height relative to the Fermi level of the negative electrode, δ_z is the barrier width and eV represents the applied

voltage across the nanoelectrodes [155]. β is the dimensionless correction factor, e and m represent the charge and mass of electron respectively, and $\hbar$ denotes the Dirac's constant.

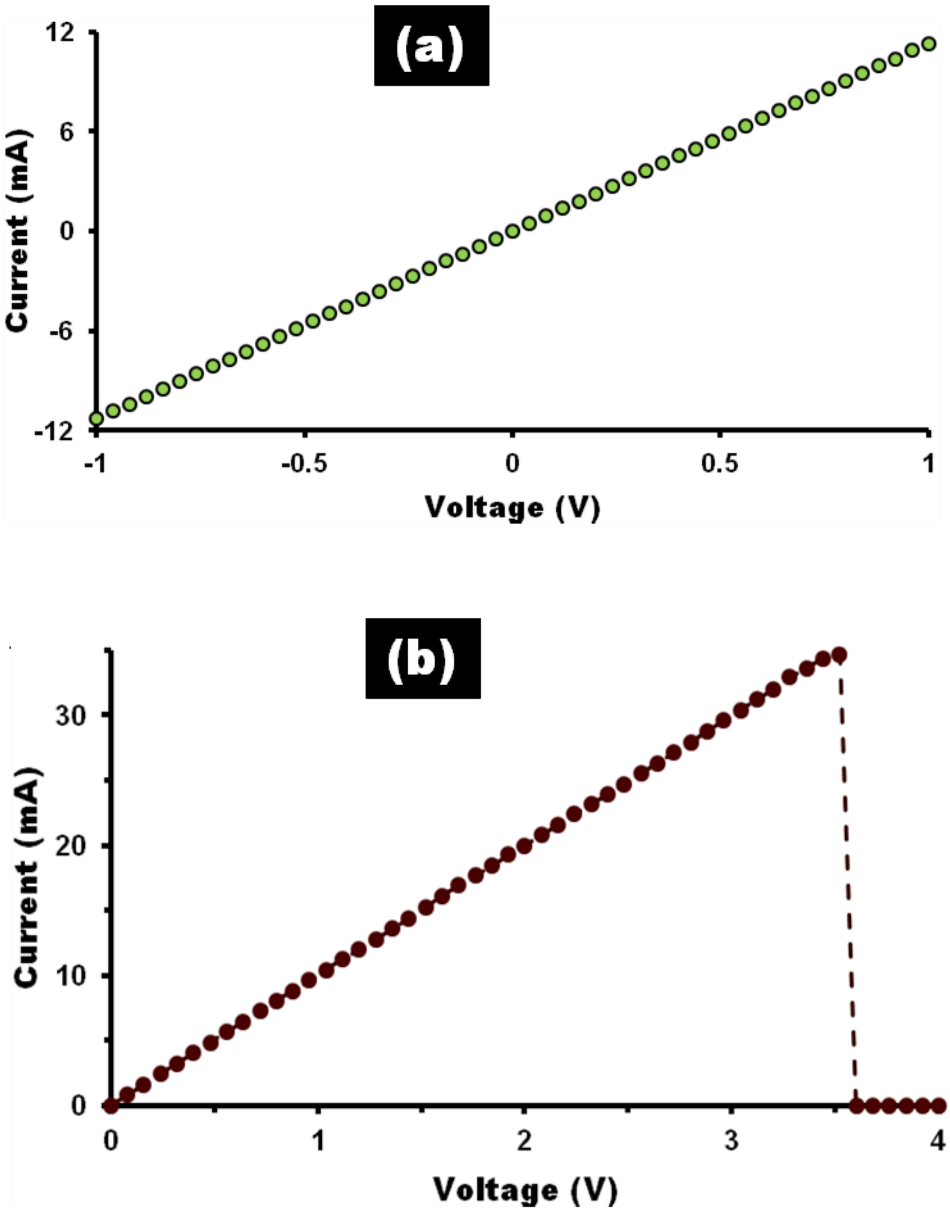

Figure 3.6 Characterization of a representative break junction; (a) Linear current signifies intact ohmic contact after FIB scratch (b) Sudden drop of current indicates the electrode separation

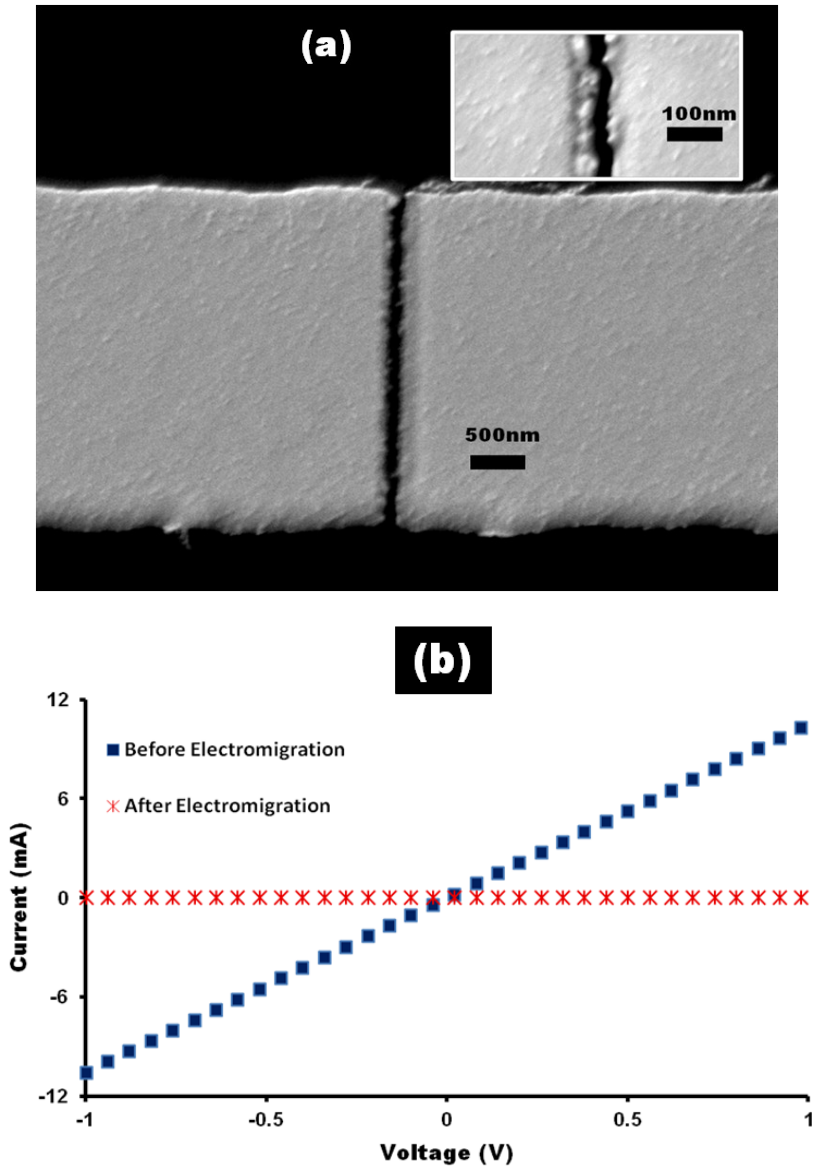

Figure 3.7 Effect of electromigration (a) SEM micrograph shows break junction with nanometer size separation and (b) Comparative *I-V* measurements show the effect of electromigration

3.3.2 Optical Characterization of Surface Chemistry

The surface binding and the presence of ssDNA and RNA aptamer immobilized on the plain surface was confirmed by Acridine Orange stain and the fluorescence measurements from the staining experiments are illustrated in Figure 3.8. The binding of ssDNA to the functionalized

plain surface is portrayed by Figure 3.8(a) whereas the hybridization of RNA aptamer to the surface-bound ssDNA is depicted in Figure 3.8(b).

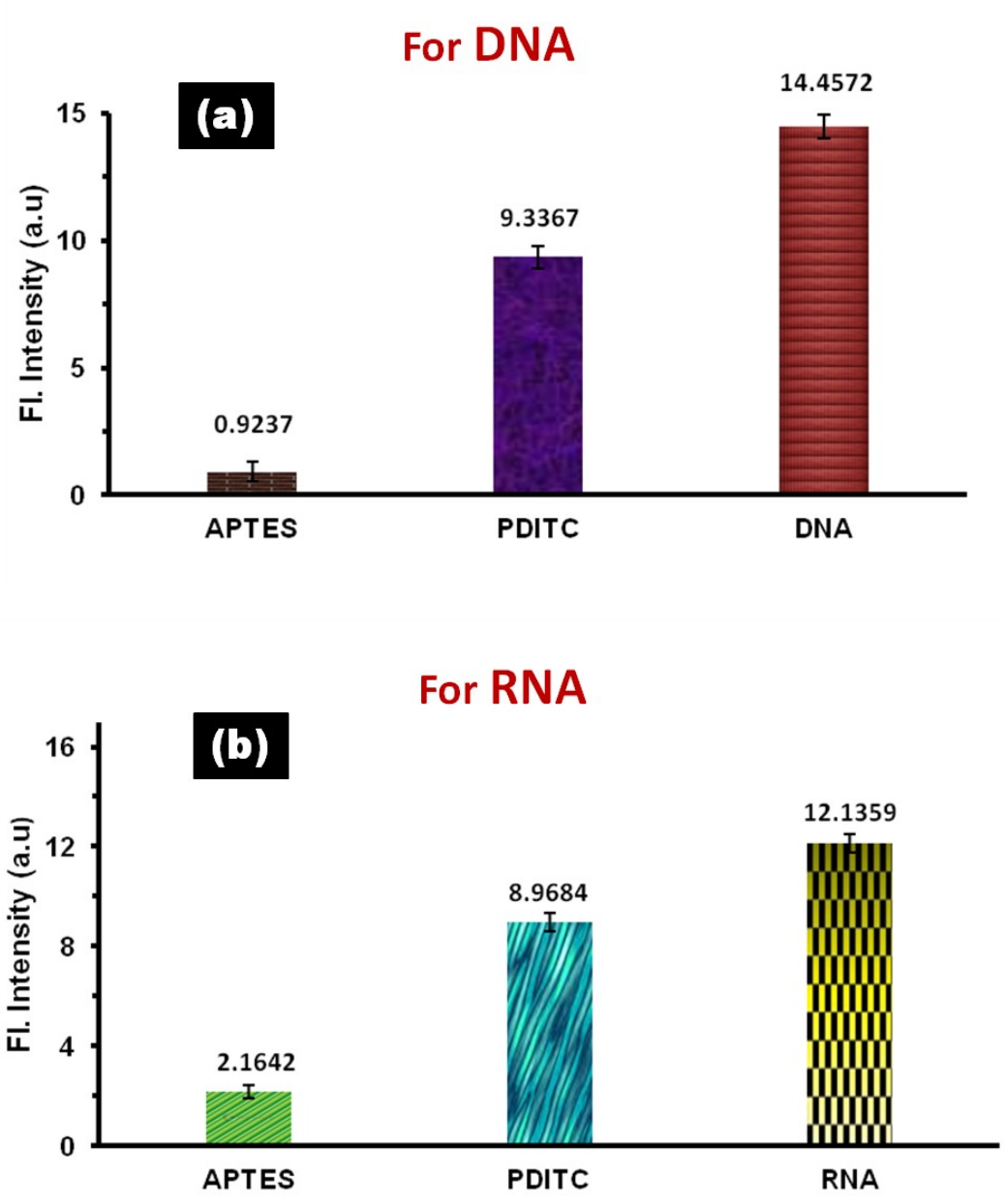

Figure 3.8 Acridine Orange (AO) stain intensity measurements (background subtracted) compares functionalized chips with control chips to illustrate (a) the presence of surface-bound ssDNA and (b) hybridization of RNA aptamers to surface bound ssDNA. The Error bars represent the standard deviation for n = 10

Acridine Orange gives green fluorescence when it interacts with ssDNA whereas a flame-red fluorescence is observed when it interacts with double stranded nucleic acids [156]. The Acridine Orange stain binds electrostatically to the nucleic acids as it carries positive charge. Electrostatic communication with non-specific polyanions was avoided by using a very low concentration of AO stain (0.2% v/v) and providing a buffer solution with some cations like Mg^{+2} and Na^{+} that compete binding to the nucleic acids [157].

EGFR binding to the probing aptamer onto the plain chip surface was confirmed by using the Sypro Ruby protein gel stain that is a ruthenium based stain used to detect the amino acids lysine, arginine & histidine [158]. Figure 3.9 demonstrates an obvious enhancement of fluorescent intensity measured from the chips having anti-EGFR RNA aptamer probes and EGFR protein as compared to that of negative control chips that include probe-functionalized chips not exposed to the target proteins and the chips exposed to the target protein but without probe aptamer immobilized on the surface. The fluorescent intensity is at a maximum when use of a blocking buffer is omitted because unreacted PDITC moieties also contribute towards protein capturing. But probe-functionalized chips with a blocking buffer selectively capture the EGFR protein as revealed by a marked increase in fluorescence intensity.

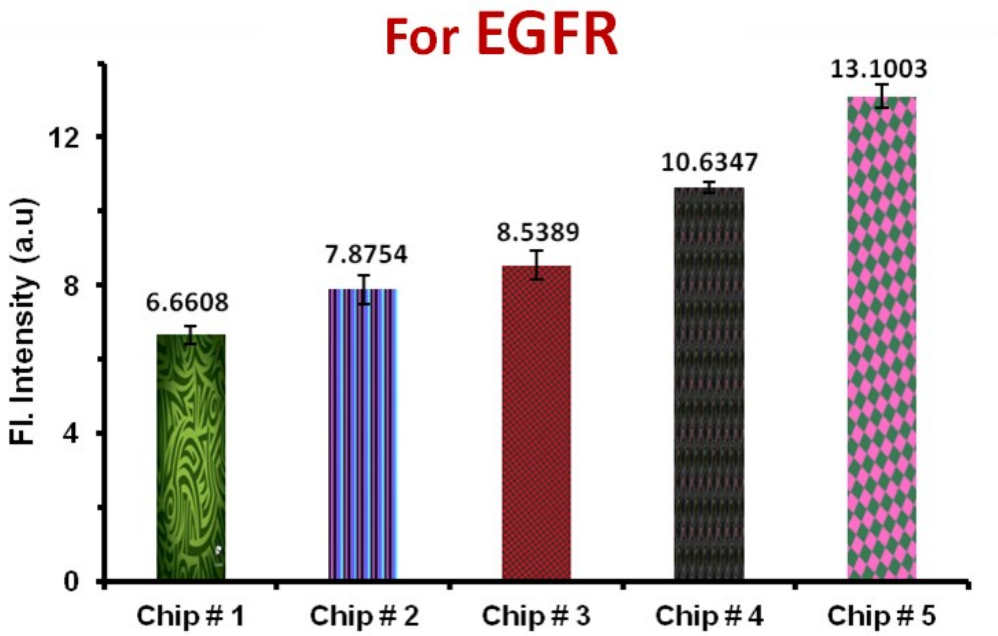

Figure 3.9 Sypro ruby protein gel stain intensity measurements confirm the selective capture of EGFR on functionalized SiO_2. From L to R: Chip # 1: Control chip treated with blocking buffer (BB) but no aptamer; Chip # 2: Control chip with no BB treatment and no aptamer; Chip # 3: Control chip functionalized with mutant aptamer and treated with BB; Chip # 4: Functionalized chip with EGFR aptamer and captured protein after BB treatment; Chip # 5: Functionalized chip with EGFR aptamer and captured protein without using BB. Error bars correspond to the standard deviation for n = 10

3.3.3 Crystal Structure and Electrical Detection of EGFR Attachment

The footstep of EGFR protein was estimated from the crystal structure of the extra-cellular region of human EGFR. Figure 3.10 shows the images for crystal structure of EGFR made by using PyMOL software. EGFR is a large, monomeric, modular glycoprotein [159] with its dimensions on the order of tens of angstroms. As a first order estimate, the protein footstep is about 11 nm as we previously reported [160]. It is expected that the protein structure would expand when it binds to the probe aptamer via its extracellular ligand binding domain. This provides a low demand on the break junction size stringency; we can detect proteins (biomarkers or others) even with the break junctions that are larger than just a few nanometers.

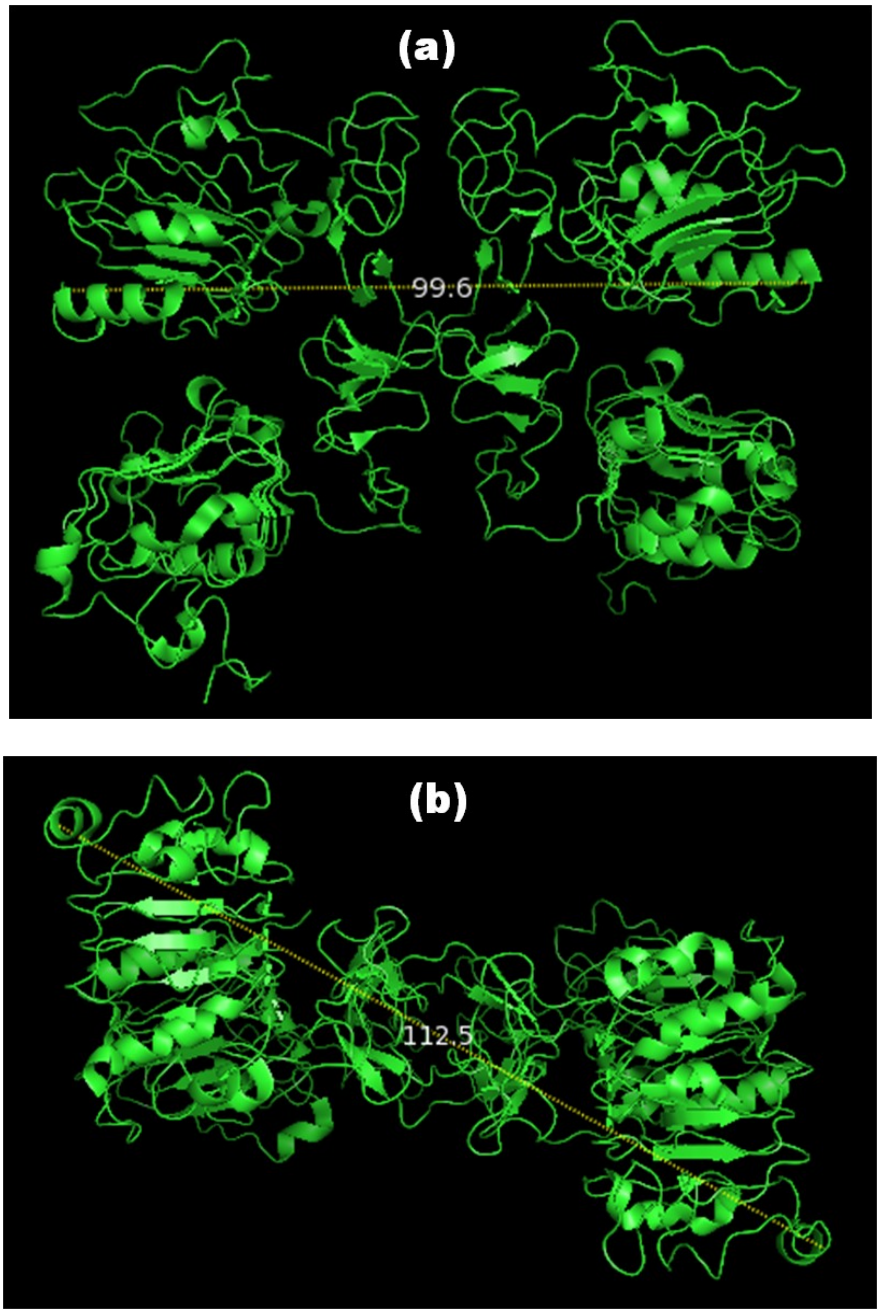

Figure 3.10 Crystal structure of the extra-cellular domain of human EGFR shows that the widest points of the structure are few hundreds of angstroms: (a) Front view, (b) Bottom view. Images are made with PyMOL 1.2.8.

The *I-V* measurements recorded from -1 to 1V across the metal electrodes, showed a significant increase in current after the capture of proteins by surface immobilized aptamers. There were two orders of reduction in the resistance between the nanoelectrodes indicating the conducting behavior of proteins that bridge the nanogap between the electrodes. Figure 3.11 presents the electronic detection of selective protein. The selectivity of the protein to anti-EGFR RNA aptamer was depicted by the control chips with similar devices fabricated onto them as shown in Figure 3.12 (a-b). The scrambled sequence in a mutant aptamer prevented it from recognizing the EGFR protein whereas anti-EGFR RNA aptamer selectively captures the protein. The yield of devices was 60% that can be further increased by tagging the protein molecules with conducting nanoparticles, e.g. of gold.

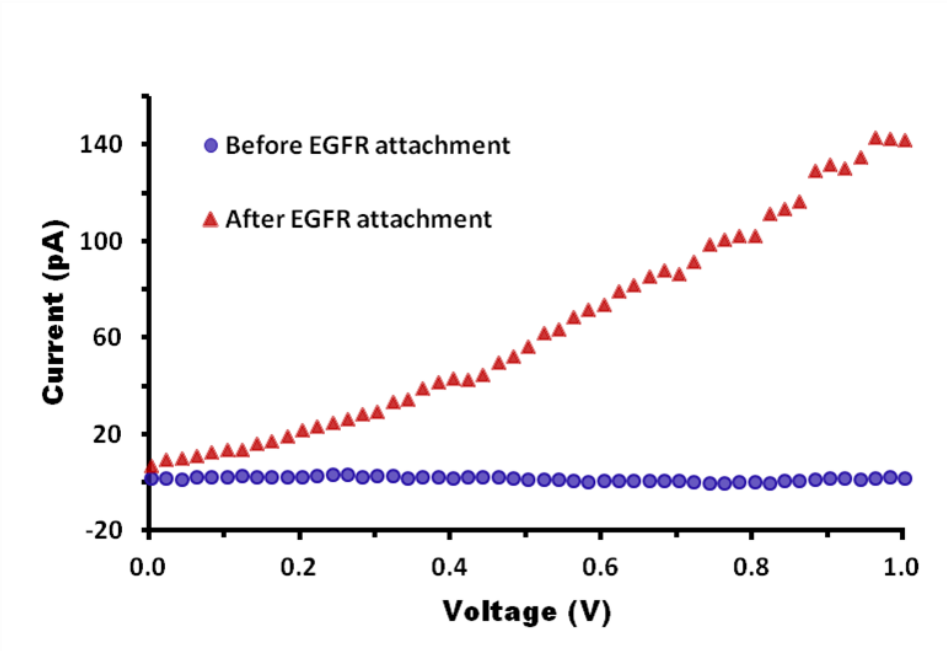

Figure 3.11 Comparison of *I-V* data for a representative break-junction before and after the incubation of functionalized chip in EGFR protein. Anti-EGFR aptamer chip shows two orders of increase in current due to the capture of EGFR bridging the nanogap

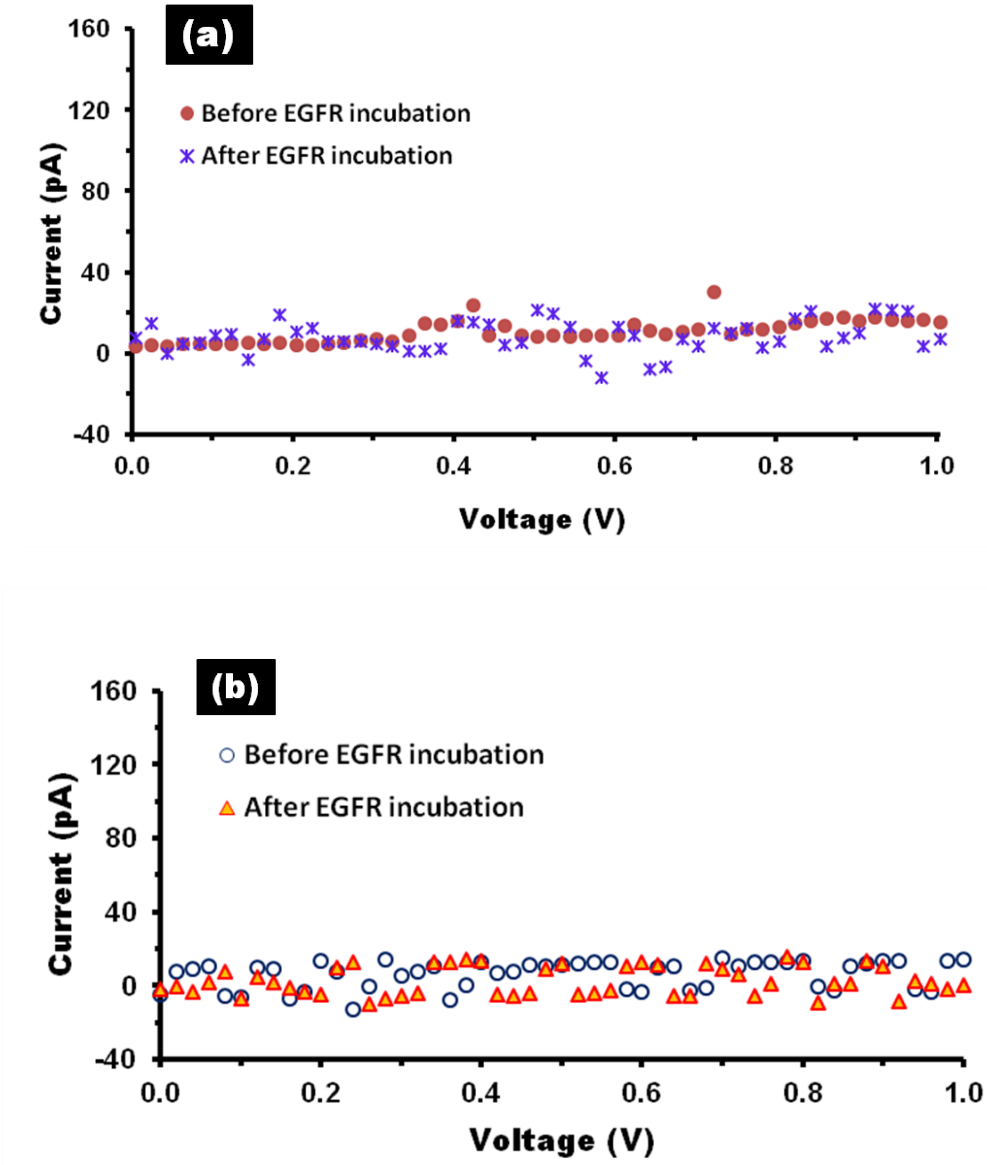

Figure 3.12 Comparison of *I-V* data for a representative break-junction on control chips before and after the incubation of functionalized chip in EGFR protein: (a) control chip functionalized with mutant aptamer (b) control chip with no aptamer show no change in conductivity which reveals the selectivity of anti-EGFR aptamer

Aptamers isolated through SELEX show high-affinity binding to target molecules. The non-specific binding of the aptamer with non-target serum proteins has already been studied and found to be very atypical [149, 161-163]. Serum EGFR levels increase in many cancer and detection of few hundreds of ng/ml would a gigantic step towards early detection. Although the concentration of EGFR used (50 µg/ml) was high but the theoretical limit of detection (LOD) of the device is much smaller. However, surface charges at nanoscale, time of detection i.e. time it would take for EGFR to reach the capture region just by diffusion [164], steric hindrance, conformation of molecules will all contribute to LOD of this framework.

3.4 Conclusion

We present that anti-EGFR RNA aptamer can specifically recognize and capture the EGFR protein that can be electrically detected using metallic break junctions with a nanometer-sized separation. The integration of FIB scratching with electromigration offers rapid, cheap and controlled manufacturing of nanoscale break junctions. After confirming hybridization of anti-EGFR RNA aptamer with surface-bound ssDNA, the nanogap break junctions were utilized for electrical detection of EGFR protein. The presence of protein between the electrodes shows a robust increase in conductivity between otherwise insulated nanoelectrodes. The detection of a disease linked protein biomarker can seriously accelerate diagnosis and therapy. Such proteonic chips can certainly find their application towards bioterrorism where dangerous viruses or bacteria can be electrically investigated for their occurrence.

CHAPTER 4

BIOMECHANICAL DISCRIMINATION OF CANCER CELLS USING SOLID-STATE MICROPORES

4.1 Introduction

Cancer has been the top ranked death-causing disease for the last several decades. Within current clinical settings, cancers are usually diagnosed at an advanced and incurable stage. Common methods used for cancer diagnosis vary between different cancer types. For example, for bladder cancer frequently used diagnostic approaches incorporate biopsy, cytology, cytoscopy, and detection of immunological markers. These approaches have inadequacies such as flawed judgment (biopsy examination and cytology), high cost (cytoscopy), low sensitivity (cytology and immunological markers) and low specificity (cytoscopy) [165-167]. Moreover, incapability of being used as point-of-care device and lack of statistical analysis of single cells limit the deployment of these methods. Therefore, a more reliable, faster processing, and inexpensive detection scheme is critical to diagnose clinically significant but asymptomatic cancer.

Tissue or cell samples taken directly from the region where tumor is suspected can be the best source to diagnose cancer. The procedure used to obtain such sample is called *biopsy*. Open surgical biopsy or image-guided intervention obtain cancer cells of primary tumors from a précised region but entail with increased risk of procedural complications [26]. Percutaneous biopsy is a typically used clinical procedure that includes fine needle aspiration (FNA) and core biopsy. FNA employs a very fine needle of 22-gauge (22G) to collect the sample for cytopathology whereas core biopsy uses a slightly larger needle of 16G or 19G to obtain a small tissue section for histology and immunohistochemical analysis [27]. Though percutaneous

biopsy offers a wide range of benefits over open surgical procedure including patient compliance, less prone to serious complications, low cost and easy processing but involves the risk of slightly missing the suspicious tumor area while collecting biopsy sample. Primary and metastatic solid tumors contain cancer cells along with normal cells like endothelial cells, fibroblasts and immune/inflammatory cells [28]. Low grade cancer and lack of precision in case of percutaneous biopsy can lead to a normal cell enriched sample with too few of cancer cells. Conventional testing procedure for such a sample is highly time consuming, technically challenging and more likely to have erroneous conclusion by the pathologist. We offer a simple and straightforward scheme that is capable to recognize a very few cancerous cells from thousands of normal healthy cells, does not require an expert/pathologist and provides statistical analysis of every single cell present in the biopsied sample.

Mechanical properties like elasticity, size, viscosity, deformability, charge and stiffness of the cells are administered by the cytoskeleton which is an internal polymer network and defines the shape of a cell, its mechanical strength and important cellular functions [168, 169]. Cell division, locomotion and transport of intracellular particles are sturdily coupled with the cytoskeleton [170]. Tumor cells differ from normal cells in various aspects including morphology, cell growth, cell-to-cell interactions and cytoskeletal organization [171, 172]. Changes to cellular functions and morphology of these diseased cells are mirrored in the cytoskeleton. Consequently these diseased cells exhibit different mechanical behaviors which indicate the physiological status of the cells and can be used as inherent cell markers for the discrimination of cancerous cells.

So far, only a few experimental systems have been deployed to study cellular mechanical properties. Micropipette aspiration is one of the prevailing techniques which applies a negative pressure to the cell and records the aspiration distance as a function of time [173]. Optical deformability, scanning force microscopy, optical tweezers, microplate manipulation and acoustic microscopy have also been reported for determining the cell rigidity [22, 174-177]. All

of these approaches revealed cancerous cells to be softer and less resistant to flow under applied forces. Oncogenically transformed fibroblast cells are known to have significantly different elasticity when compared to their complementary normal cells [173]. Human breast cancerous cell lines (MCF-7) also exhibit enhanced elasticity than their counterpart normal cell lines (MCF-10) due to dissimilar viscoelastic nature of cells [22]. Metastatic cancer cells display even higher elasticity which stems from their need to squeeze through the surrounding tissue matrix for making their way into the circulatory systems [30, 173]. These discoveries advocate the use of cellular elasticity as a robust cell marker to diagnose the underlying disease. But all of the current techniques are limited by poor statistical differentiation, low throughput, high cost, special preparation and non-physiological handling or cell adhesion due to mechanical contact of the probe. Herein, we present a novel scheme of using a single solid-state micropore as biological transducer that translates the cell mechanics to electrical signals. A single micropore on a membrane sandwiched by a dual compartment setup is used to record the electrical signature of the single cell translocated through the micropore. The specific pulse characteristics distinguish the cancerous cells from healthy ones and provid a statistical differentiation of each translocated cell in a cost-effective, high throughput and much reliable fashion.

Solid-state micropores have been used in a variety of sensor applications. These have been deployed for electroporation, patch clamp measurements, stability of lipid bilayers, monitoring bacterial activities, investigating cell deformability, size based discrimination, cell counting and measuring electric properties of a single cell [31-36]. Chemical and thermal stability, mechanical strength and capability to be integrated in a Lab-on-a-chip locale enable micropores to be used for such diverse studies. Though micropores have been reported for investigating cell deformability or detecting large size circulating tumor cells (CTCs) present in blood but these have never been deployed for diagnosing cancerous cells based on merely cell mechanics discrimination between similar sized cells.

Bladder cancer cells have been reported to be as much as 32 times softer than the normal cells using scanning force microscopy [29]. Exceedingly different viscoelastic nature of bladder cancer cells makes these a strong candidate for undertaking elasticity as an inborn cell marker to distinguish the tumor cells from the healthy ones. This study presents a simple and dependable scheme to diagnose bladder cancer. PDMS microchannels were employed to compare the motility and stiffness of bladder cancer cells with that of normal urothelial cells and a distinctive viscoelastic behavior was observed. The micropore device not only evaluates the mechanical properties of cells for correlated detection of cancer cells but also provides statistical analysis of every single cell present in the investigated sample. Relatively larger mass of cells doesn't allow these to translocate through micropores under electrophoretic bias. Therefore, an optimized fluid pressure was used for translocation of cells through the micropore. The ionic current flow through the micropore was continuously monitored and physical blockage of the micropore gave distinctive current pulses. Pulse magnitude, width and shape indicate the biomechanical properties of the translocated cell and provided the quantifiable viscoelastic behavior of a single cell which distinctively correlated to the physiological state of the cell. The capability of our device to recognize tumor cells when they are not many in contrast to their normal counterpart (1:1000) takes over the prime challenge in conventional biopsy examination.

4.2 Materials and Methods

4.2.1 Fabrication Process for Micropore Device

All the chemicals were obtained from Sigma-Aldrich (St Louis, MO, USA) unless mentioned otherwise. The fabrication process started with a double-side polished, (100) orientation silicon wafer and a thermally grown 200 nm thick oxide layer was deposited on it as shown in Figure 4.1. After standard RCA cleaning process of the wafer, a uniform layer of photoresist (Shipley S1813) was spin coated on one side of the wafer and g-line photolithography was used to open square windows. The other side (bottom side) of the wafer

was manually coated with photoresist to shield the oxide layer from getting etched by buffered hydrofluoric (BHF) acid. The square window pattern was transferred to the underlying oxide layer by using BHF etching and then acetone was used to remove the residual photoresist on both sides of the wafer.

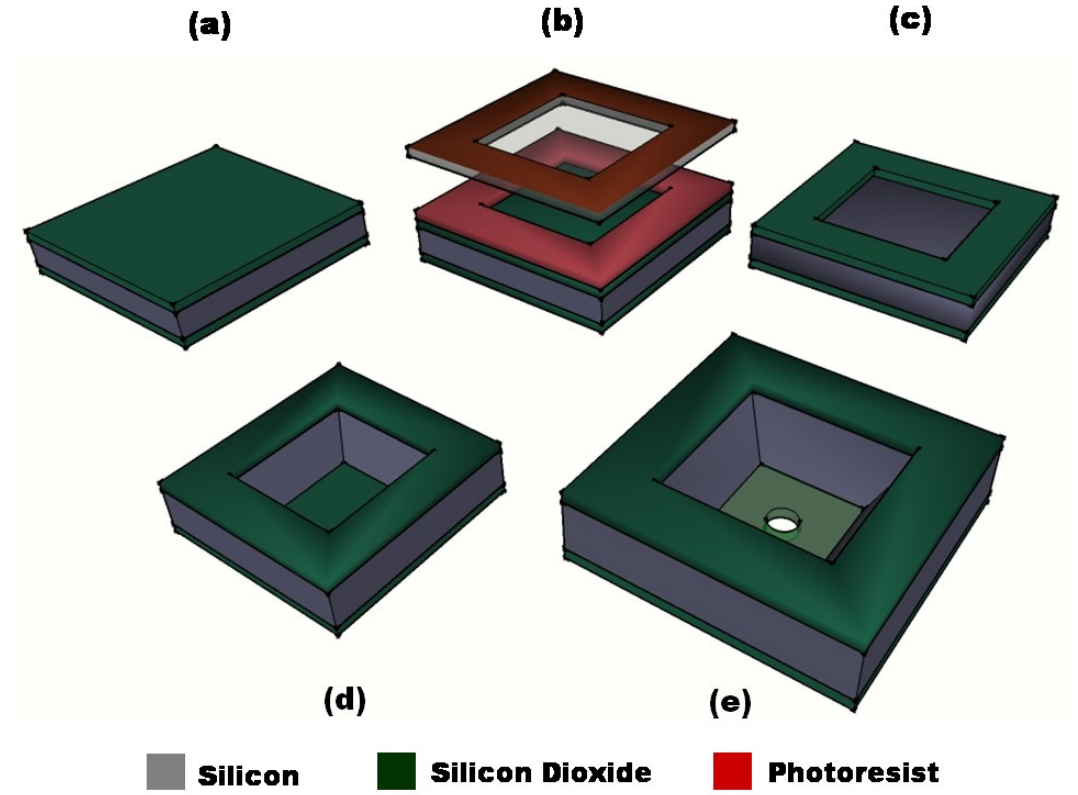

Figure 4.1 Fabrication process of solid-state micropores (a) Thermally grown 200 nm thick oxide layer on both sides of double side polished silicon wafer (b) Spin-on photoresist followed by conventional photolithography to open square windows in resist layer (c) BHF etching to transfer the square window pattern to the underlying oxide layer (d) TMAH anisotropic wet etching of Si using oxide layer on the other side of the wafer (bottom side) as the etch stop to obtain oxide membrane diaphragms (e) Drilling of micropore in the oxide membrane using focused ion beam (FIB)

The wafer was immersed in diluted solution (25%) of tetramethylammonium hydroxide (TMAH) at 90 ^{o}C for anisotropic wet etching of silicon. The silicon wafer was etched through the whole thickness with sidewall angle of 54.7° until oxide layer on the other side was reached

forming an inverted pyramid as shown in Figure 4.2. The V-groove etching of Si gave freely-standing oxide membranes. These thin oxide membrane had wavy topography which was due to the internal stresses as shown in Figure 4.3(a). Micropores of 20 μm size were drilled in these thin oxide membranes using the focused ion beam (FIB). The diameter of the drilled micropore was defined by the FIB milling current, thickness of the membrane, material of the membrane and the drilling time [36, 178, 179]. Higher the exposure time or the milling current, larger was the diameter of the resulted micropore. SEM micrograph of the drilled micropore revealed that the periphery of the micropore was rough which could rupture the cell membrane during translocation. Thermal treatment of micropores at 1050 °C for 5 minutes not only helped to make the inner walls of the micropore smoother and flat but also removed the residual stress of oxide membrane. Figure 4.3(b) demonstrates the micrograph of a micropore after thermal treatment.

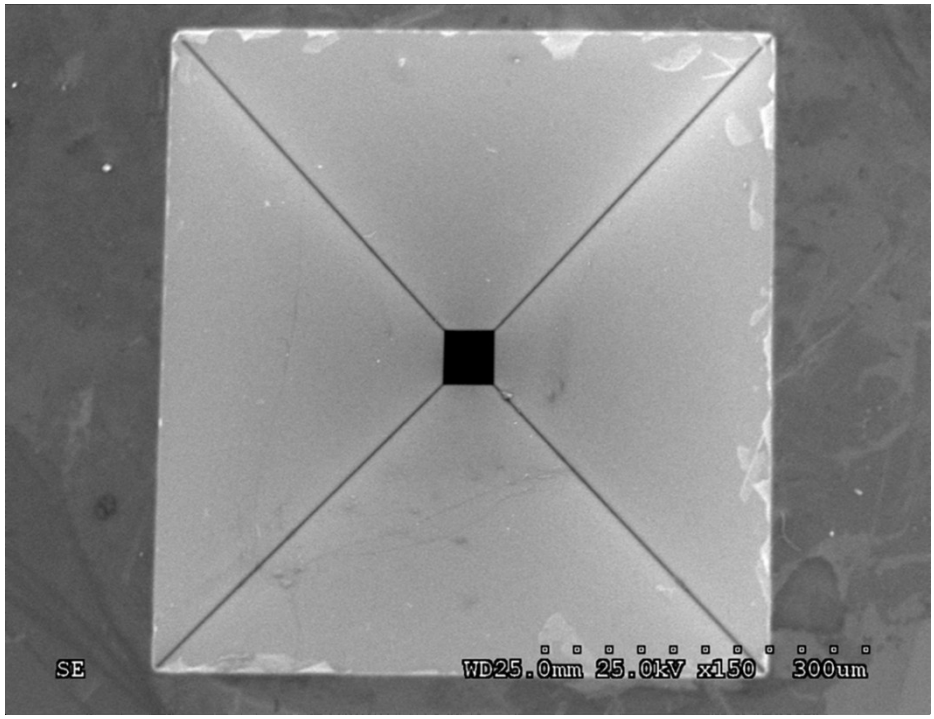

Figure 4.2 SEM micrographs showing *V*-grooved etching of Si using TMAH

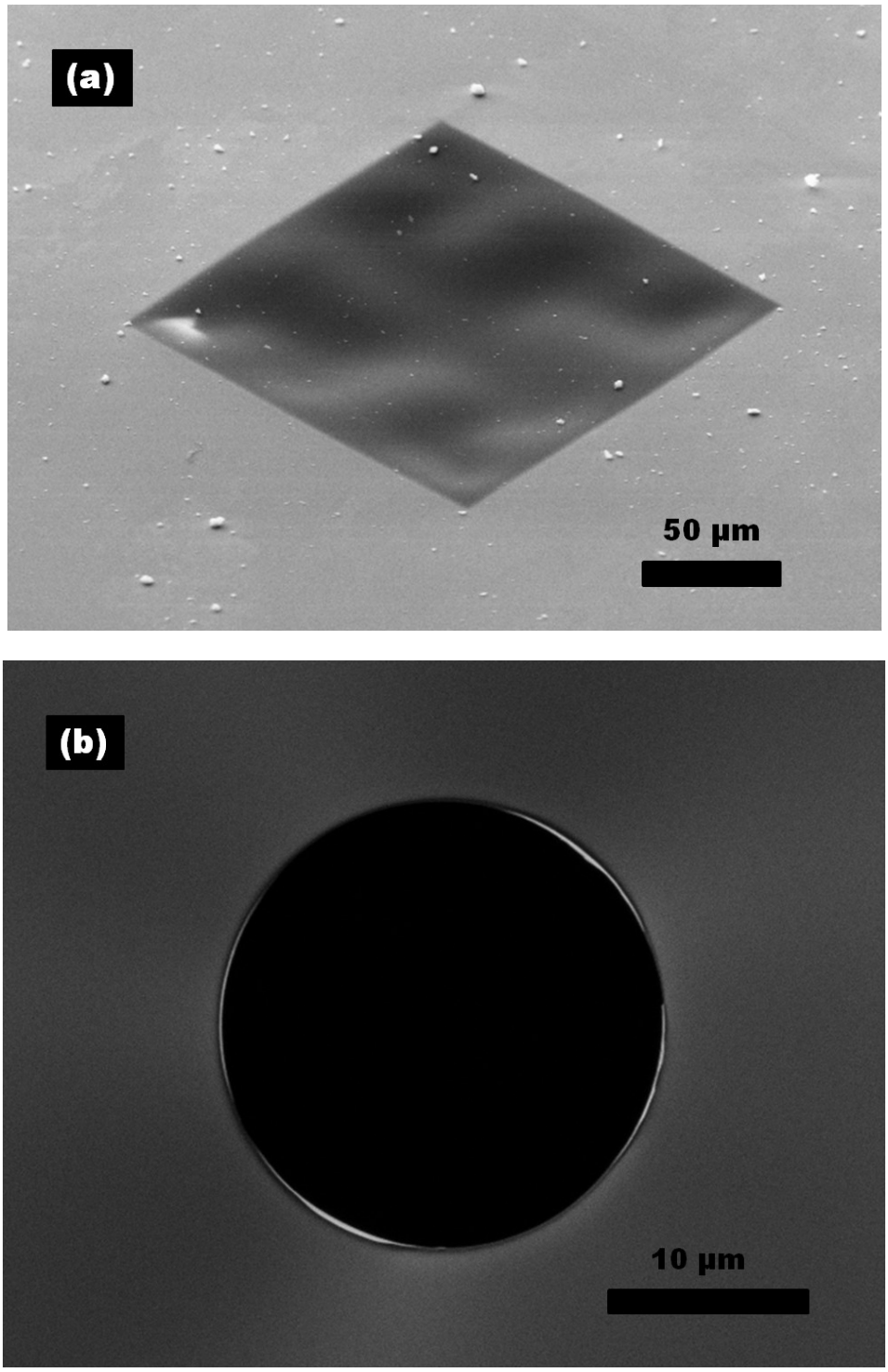

Figure 4.3 SEM micrographs displays (a) Wavy surface of oxide membrane due to internal stress (b) 20 µm micropore after thermal annealing

4.2.2 Experimental Setup for Electrophysiological Analysis of Cells

The overall experimental system for processing and measuring the electronic signature for cells is shown in Figure 4.4 (a). The dual compartment scheme was implemented by making use of two separate Teflon blocks. Each block had a small channel ending in 1 mm opening which aligned when the blocks were assembled together. The micropore chip was squeezed in between the two blocks while polydimethylsiloxane (PDMS; Dow Corning) gaskets were deployed on both sides of the chip to evade the outflow of NaCl (0.85% w/v) solution which filled the compartments. Figure 4.4 (b-c) shows the Teflon assembly with PDMS gaskets on sides of the micropore chip. Ag/AgCl electrode pair was used to measure the ionic current flow across the micropore. Data acquisition cards (National Instruments) connected to these electrodes provided voltage biasing and recorded the current measurements. A tubing adapter appended the inlet compartment of the Teflon block assembly to a syringe pump (Harvard Apparatus). The syringe pump injected the cells suspended in NaCl solution into the inlet compartment at an optimal flow rate while the outlet compartment was filled with NaCl solution only. Polypropylene cell strainer (BD Falcon) with a nylon mesh (100 μm size) was used to obtain a more uniform single cell suspension and eliminate any chunks or cell clumps. When a cell translocated through the micropore, physical blockage of the micropore offered more resistance to the flow of ionic current. Resistance to the flow of current is given by $R = \rho L/A$ where ρ is the resistivity of NaCl (0.85% w/v) solution, L represents the thickness of oxide membrane and A stands for the effective area of the micropore. Therefore, any variation to the effective area of the micorepore due to physical blockage by translocating cells was mirrored in its conductivity. The micropore device needs to be tuned for particular set of experiments so that the optimal flow rate, sampling interval and micropore size can be selected. The fine-tuning of the experimental setup picks optimal processing parameters depending upon the size, density and the mechanical properties of all types of cells present in the investigated samples.

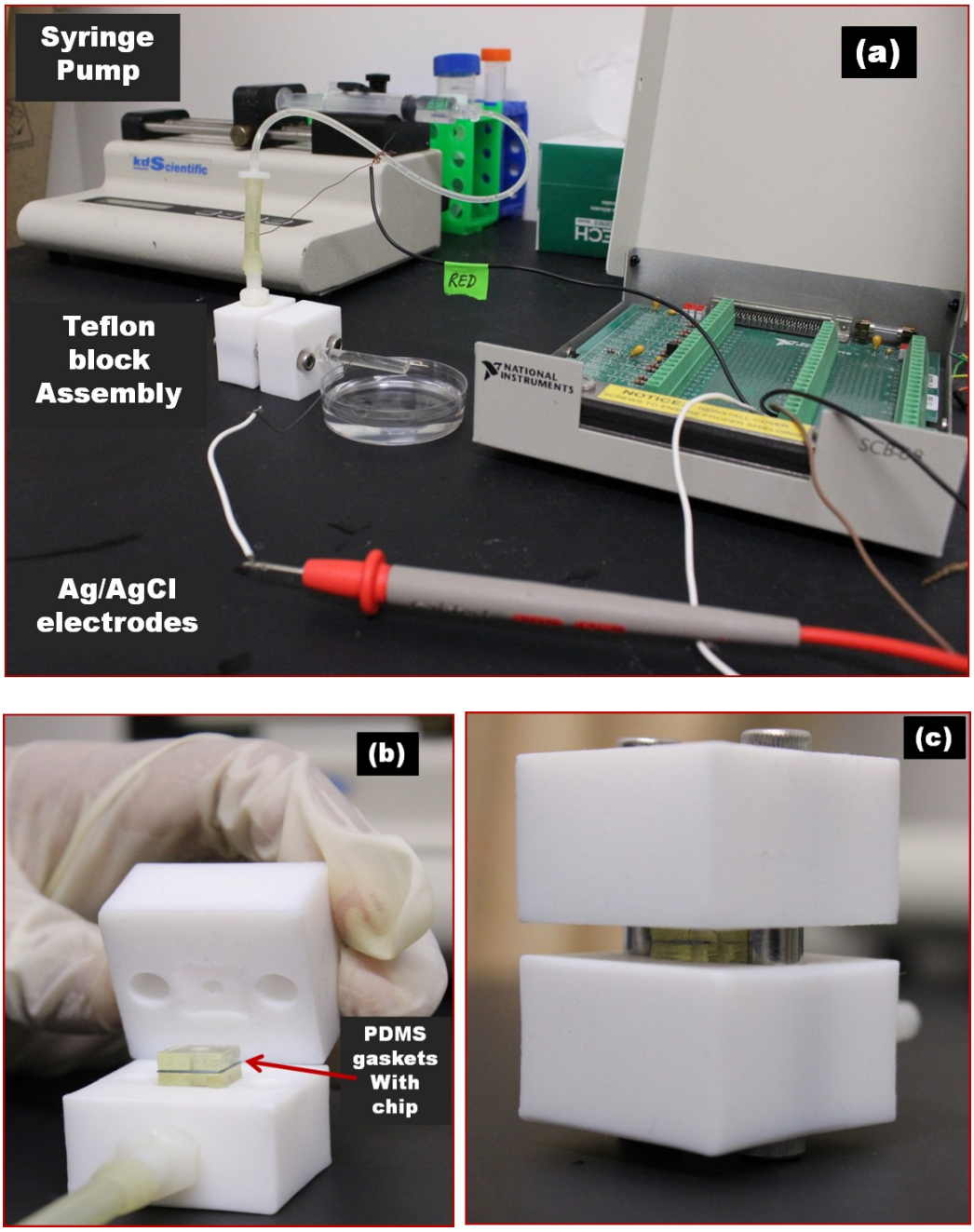

Figure 4.4 Micropore Teflon device system (a) Syringe pump pushes the cells to the inlet chamber of Teflon block assembly. The chip with single micropore is sandwiched between the Teflon blocks. PDMS gaskets are used to avoid leakage and Ag/AgCl electrodes are inserted in the tubing appended at the inlet and outlet chambers (b) The inner view of Teflon blocks before being assembled (c) Micropore device after getting assembled device

4.2.3 Tapered Microchannels in PDMS for Cell Migration Comparison

PDMS microchannel devices were fabricated using the conventional soft lithography technique. Each device had 150 μm deep inlet and outlet reservoirs which were connected through an array of 300 tapered micro-channels (from 20 × 5 μm^2 to 5 × 5 μm^2). Initially, photolithography was done to define patterns on master mold which was then used to transfer patterns into PDMS. After punching the fluidic ports, the PDMS device was sterilized, treated with UV Ozone plasma for 5 minutes and bonded to sterilized glass coverslip. Fifty thousand of living cells were seeded in the inlet reservoir and allowed to migrate through the microchannels. Optical micrographs of migrating cells were captured on regular intervals up to 4 days as shown in Figure 4.5(a). The number of cells that squeezed through the channels and transited to the outlet reservoir over the same length of time were quantified to compare the viscoelastic nature of bladder cancer cells to normal urothelium cells. Figure 4.5(b) illustrates the quantitative comparison of the motility of cancerous cells and normal urothelial cells.

4.2.4 Normal Human Urothelium Cell Culture

Immortalized normal human urothelium cells were cultured with T-medium (Invitrogen) supplemented with 5% fetal bovine serum. Cultured normal human urothelial cells appeared as an epithelioid cell monolayer and were enzymatically dissociated with trypsin (0.25%)-EDTA (0.03%) solution for the experiments. The dissociated cells were counted using standard hemocytometer to get the desired cell density in the processing solution.

4.2.5 Human Bladder Cancer Cell Line Culture

Human bladder cancer cell line was purchased from American Type Culture Collection (Rockville, MD) and cultured with T-medium supplemented with 5% fetal bovine serum. Once bladder cancer cells were confluent, trypsin (0.25%)-EDTA (0.03%) solution was used to dissociate the cells enzymatically in order to acquire cells for the experiments.

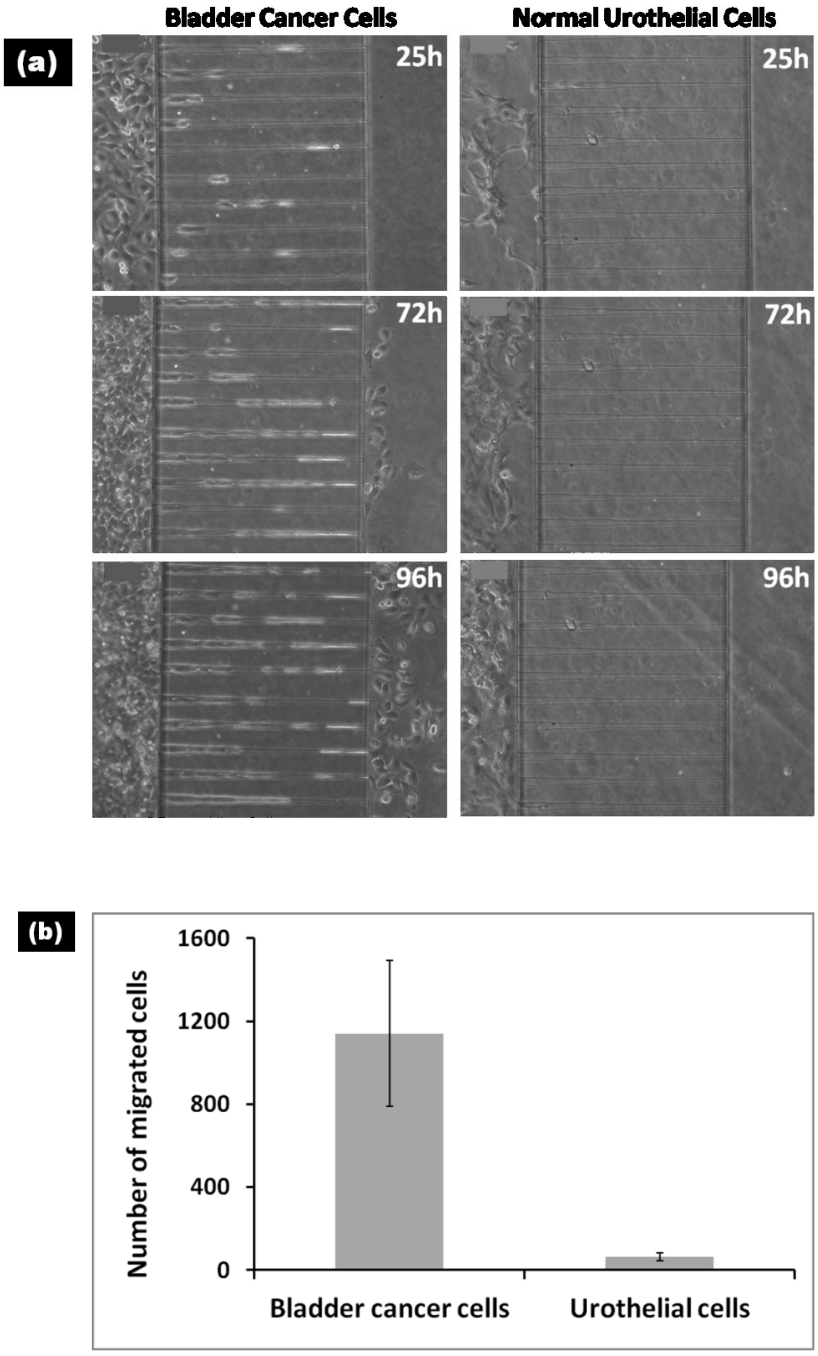

Figure 4.5 Cell-migration through the tapered microchannels (a) Softer nature of bladder cancer cells allow a large number of cells to squeeze and enter the tapered microchannels while stiffness of normal urothelial cells restrain them from entering into same sized microchannels over same length of time (96 hours) (b) The quantitative comparison of cell-migration for both types of cells.

4.3 Results and Discussion

4.3.1 Cell Migration and Morphology

Comparative study of cell migration on PDMS micro-channels revealed that quite a large number of bladder cancer cells managed to enter the microchannels, briskly migrated through the channels and exited to the outlet reservoir over a period of 96 hours whereas normal human urothelium cells were inhibited from entering the same microchannels after same time span. This clear disparity in their morphological flexibility and mobility indicated to notably different mechanical properties of cancerous cells from their healthy counterparts. This might be due the flexible cytoskeleton of malignant cells stemming from their faster replication and enhanced motility [22]. Thus, cellular rigidity reflects the physiological status of the cells and can be used to detect and isolate the diseased cells. The trypsinized cells assumed the spherical shape in suspension and were found healthy after disaggregation as can be seen in Figure 4.6. These optical micrographs also demonstrated that bladder cancer cells were nearly equal in size to that of normal urothelial cells (20-25 um). It dictated that size-based discrimination techniques would be incapable to distinguish between the two types.

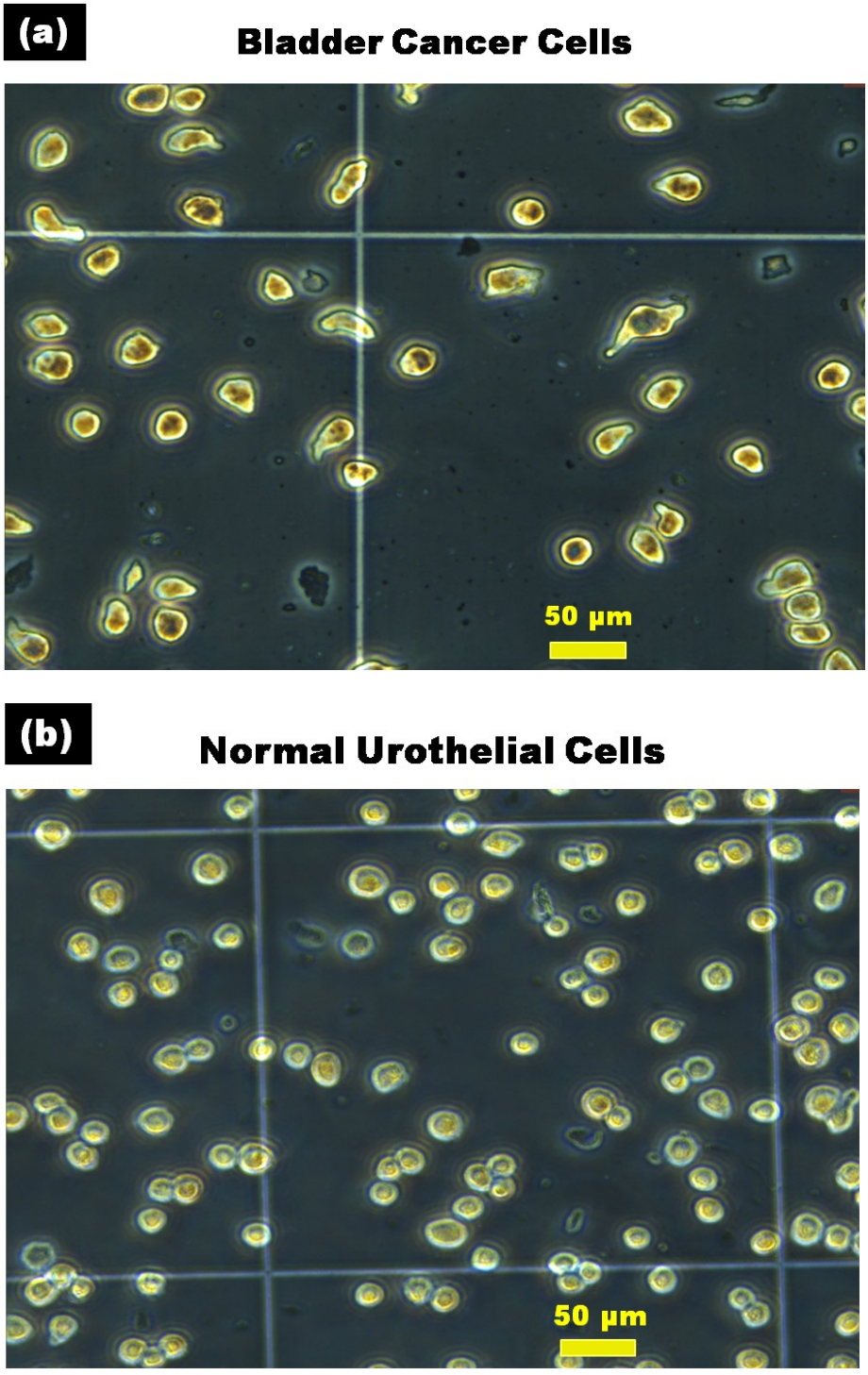

Figure 4.6 Optical micrographs for both types of cells after dissociation demonstrate that cells hold spherical shape in suspension and are approximately equal in size.

4.3.2 Optimization of the Micropore Device

Dual compartment micropore device was assembled as explained in Materials and Methods section. The membrane thickness, micropore size, flow rate and sampling frequency were tuned and tweaked to confine one cell at a time and record the mechanical behavior of every single cell of the sample. Thin silicon dioxide membrane (200 nm) guaranteed single cell translocation through the micropore at any specific time. Micropores less than 12 μm didn't allow the normal urothelial cells to pass through easily and were prone to blockage. On the other hand, micropores larger than 25 μm missed some translocation events so 20 μm diameter micropore size was selected for its enhanced discrimination without getting blocked. An optimized flow rate of 20 μl per minute was selected to achieve maximum throughput without losing any cell translocation events. Similarly, electrical signal sampling frequency was optimized. High sampling frequency induced a lot of inherent noise which could suppress some current blockage signals during translocation. Lower frequency provided a more stable baseline with less noise but events with translocation times less than the sampling interval could be missed. The optimum ionic current sampling frequency was chosen to be 0.2 MHz which elucidated that electrical signal collection after every 5 μsec. A 5 volts bias was applied across micropore resulting in a 25 MV m^{-1} transmembrane field across the 200 nm long channel. The field would be present only in the locality of the membrane and would not build any gradient in the bulk solution [180]. The cell's microenvironment was not affected by this electric field because fast translocation events were too quick to root any in-house damage to the cells. We observed the cells that were processed through the device and found that the cells retained their structural properties and looked similar to unprocessed ones.

Phosphate buffered saline (PBS) and 0.85 percent NaCl solution are commonly known physiological silanes for cell suspension [36, 181, 182]. We suspended the cells in NaCl (0.85% w/v) solution because Ag/AgCl electrodes started losing their AgCl coating in PBS, which was obvious by the whitish end of electrode dipped in PBS. The gradual loss of AgCl coating caused

an unstable baseline but NaCl solution resolved this issue by providing enough Cl^- ions for Ag to retain the AgCl coating on it.

4.3.3 Effect of Membrane Thickness

The thickness of the oxide membrane defined the area of contact of the cell membrane with the inner walls of the micropore. Micropores of same size but different membrane thickness (200, 330 and 450 nm) were used to study its impact on the translocation behavior of cells. The translocation profile was not much affected by varying the thickness of the membrane but thicker membranes were found to be more prone to blockage/clogging of the micopore. Longer channels provided more area for physical contact between tranlocating cell and the hydrophilic micropore walls. This increased the probability for cells to adhere on the micropore walls due to hydrophilic phosphate heads on lipid bilayers which caused plugging of the micropore. Thus thinner oxide membrane (200 nm) not only ensured single cell confinement but also removed the possibility for the micropore to get clogged/blocked while providing enough mechanical strength to be used for multiple runs of the experiment.

4.3.4 Cell Concentration and Reliability

Different concentrations of bladder cancer cells were used to get the electronic fingerprint of each single cell in the sample. Figure 4.7 represents the electrical signal for a high concentration (20000 cells per ml) and a very low concentration (100 cells per ml). The translocation profile was found to be steady throughout the measurements regardless of the cell suspension concentration. It demonstrates that the frequency of pulses reflects the concentration and can be used for cell enumeration. Figure 4.8 shows the electrical signal profile at different time points (1, 10 and 30 minutes) after the initial detection of a cell which is indicated by pulses in the electrical signal. Similar translocation profile throughout the experiment showed that the micropore stayed open and viable for the measurements. Hence, our micropore device is highly dependable for electrophysiological analysis of cells.

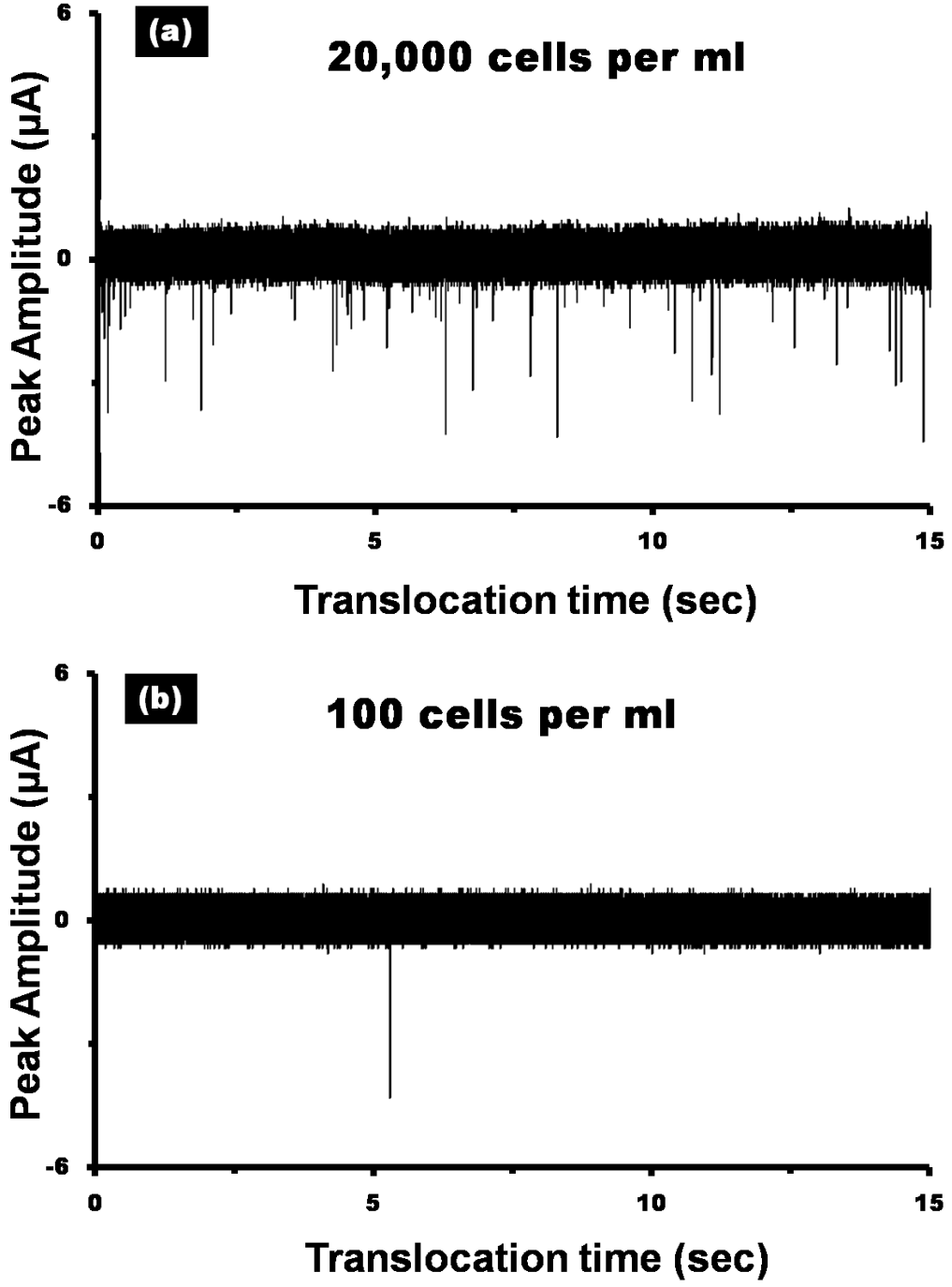

Figure 4.7 Electrical signals from a high and low concentration cell suspension reveal that number of pulses can be used for cell counting.

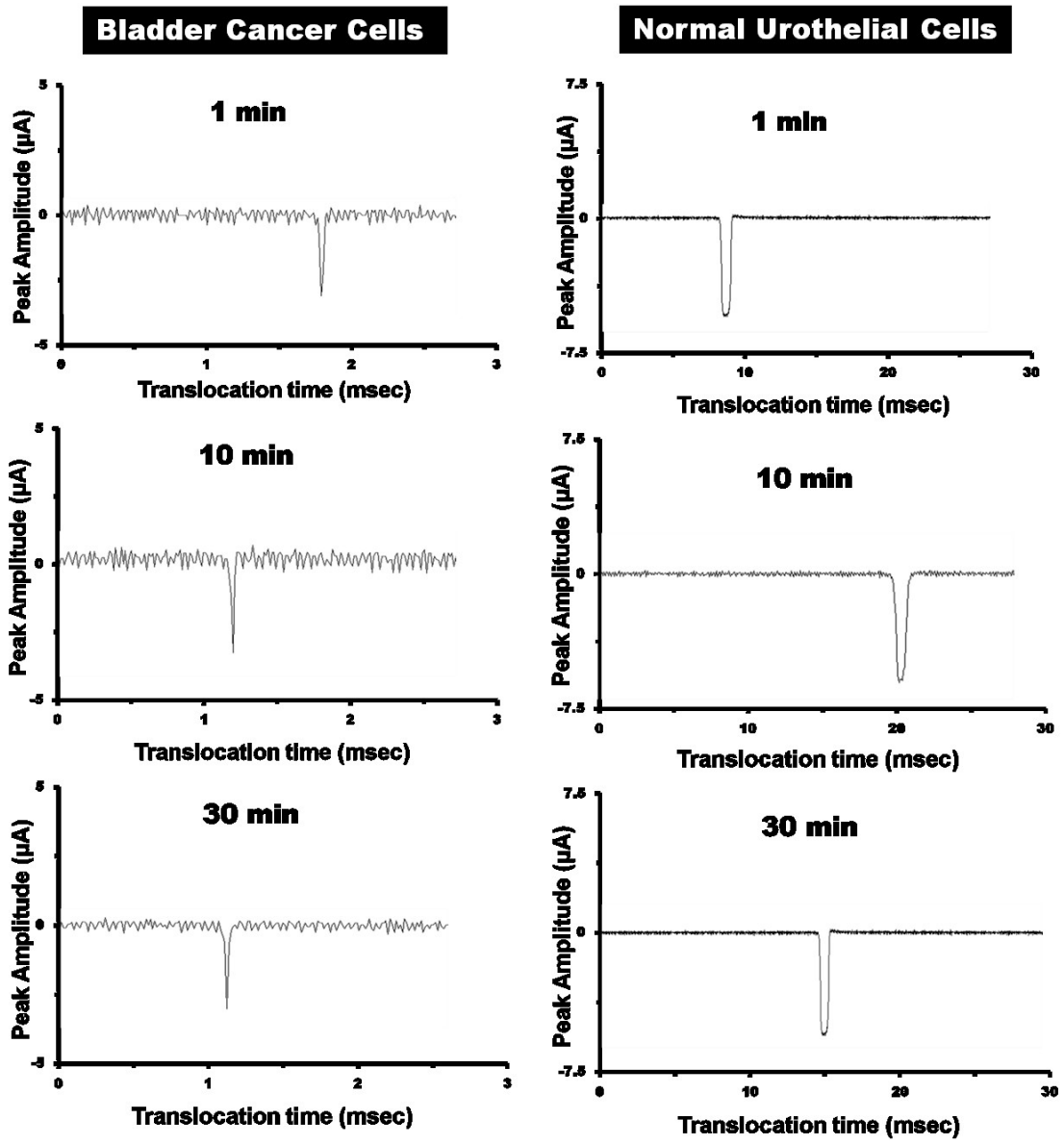

Figure 4.8 Comparison of pulse signals at different time points demonstrate that translocation profile for each of the two cell types remains stable throughout the experiment.

4.3.5 Biomechanical Discrimination of Cancer Cells

The goal of the presented study was to distinctively identify and quantify the bladder cancer cells from ionic current fluctuations through the micropore based upon dissimilar

biomechanical properties of the two cell types. Equal concentrations (20000 per ml) of bladder cancer cells and normal urothelium cells were suspended in separate solutions which were processed for 30 minutes. Bothe the cell types were processed with our micropore system under exactly similar conditions to eliminate the effect of background noise. The measuring setup was set to the optimized parameters (micropore size, flow rate, sampling frequency and membrane thickness) while processing each of the two cell types. The experiments were repeated at least three times and similar results were observed for a particular cell type.

The data showed characteristically different translocation profiles for the two types of cell suspensions. The cells suspended in NaCl solution gave distinctive current blockage pulses due to physical blockage of the micropore. Figure 4.9 (a-b) shows characteristic pulse signals for bladder cancer cells and normal urothelial cells. Though cell strainer was employed to remove cell clots but still a few of the cells were seen clumped together which were easily recognized from their current blockage pulse shape as demonstrated by Figure 4.9(c).

More than 90% of bladder cancer cells were distinctively identifiable from normal urothelial cells by their pulse characteristics (width, amplitude, pulse shape). When the cancerous cells passed through the micropore, these squeezed due to their deformable nature and translocated through the 20 μm micropore in much smaller time as compared to their counterpart. Though both the cell types were not much different in size yet normal urothelial cells showed one order of magnitude increase in translocation time owing to their stiffer nature.

The pulse shape can explicitly describe the orientation of the translocating entity [36, 183]. The ionic current through the micropore corresponded to a cross-sectional circular contour which portrayed the particular physical dimension of the confined cell. The outline of translocated cell predominately defined the pulse shape whereas cell's biomechanical properties characterize its translocation profile. Figure 4.10 shows the scatter plot to demonstrate the distribution of pulses for both the cell types processed separately under similar conditions.

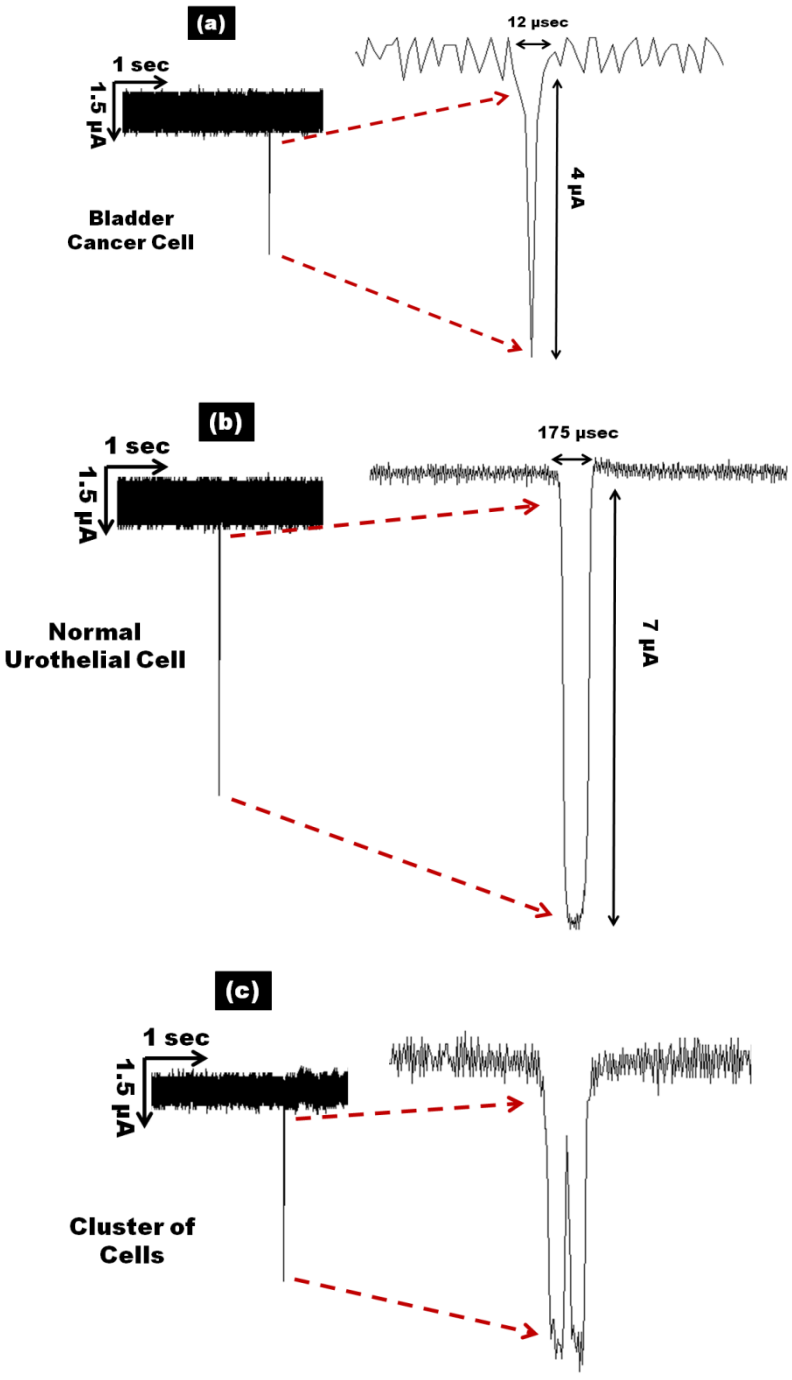

Figure 4.9 Translocation profile (translocation time, current peak amplitude) of the cell passing through the micropore. Characteristic pulse signals form (a) Bladder cancer cell (b) Normal urothelial cell (c) cell cluster which would be ignored during data analysis.

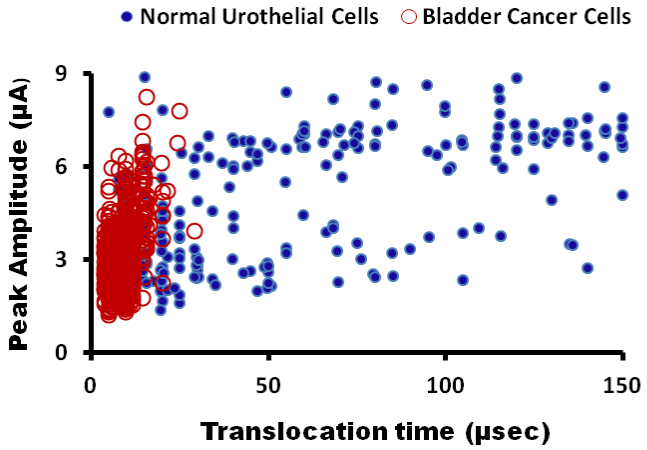

Figure 4.10 Scatter plot shows the distribution of pulses for both the cell types

The pulse statistics (average translocation time and peak amplitude) for the two cell types are shown in Table 4.1. Statistical analysis based on translocation time and the peak amplitude was performed using one-way ANOVA and it demonstrated that the two types were significantly different from each other (p-value < 0.001). The normal human urothelium cells showed a greater spread of data because plugging effect of the stiffer cells gave jolted and fluctuated pulses. The reported method not only discriminated the cancerous cells but also provided adequate information to exactly trail the 3D profile of the translocated cell.

Table 4.1 Translocation Summary of pulse statistics for both cell types through 20 μm micropore

Cell Types ➔ **Measurement (Units) ↓**	**Bladder Cancer Cells**	**Normal Urothelial Cells**
Average Translocation Time (μsec)	8.48±3.45	107±89.06
Average Peak Amplitude (μA)	3.11 ± 1.04	5.64 ± 2.15

4.3.6 Identification of Cancer Cells from Mixed Cell Suspension

After defining the pulse characteristics (pulse duration, peak amplitude, pulse shape) for each cell type, the bladder cancer cells were mixed with normal urothelial cells using different concentration ratios (1:1, 1:10, 1:100, 1:1000) to detect the presence of cancerous cells out of a mixture. The data was recorded at optimized flow rate (20 µl min^{-1}) and sampling interval (5 µsec). Density plots were drawn to analyze the data distribution as shown in Figure 4.11. The data showed that the device could identify the cancerous cells with a detection efficiency of more than 75% which elucidated our device as a simple, cheap, faster and reliable electronic biosensor for early diagnosis of cancer.

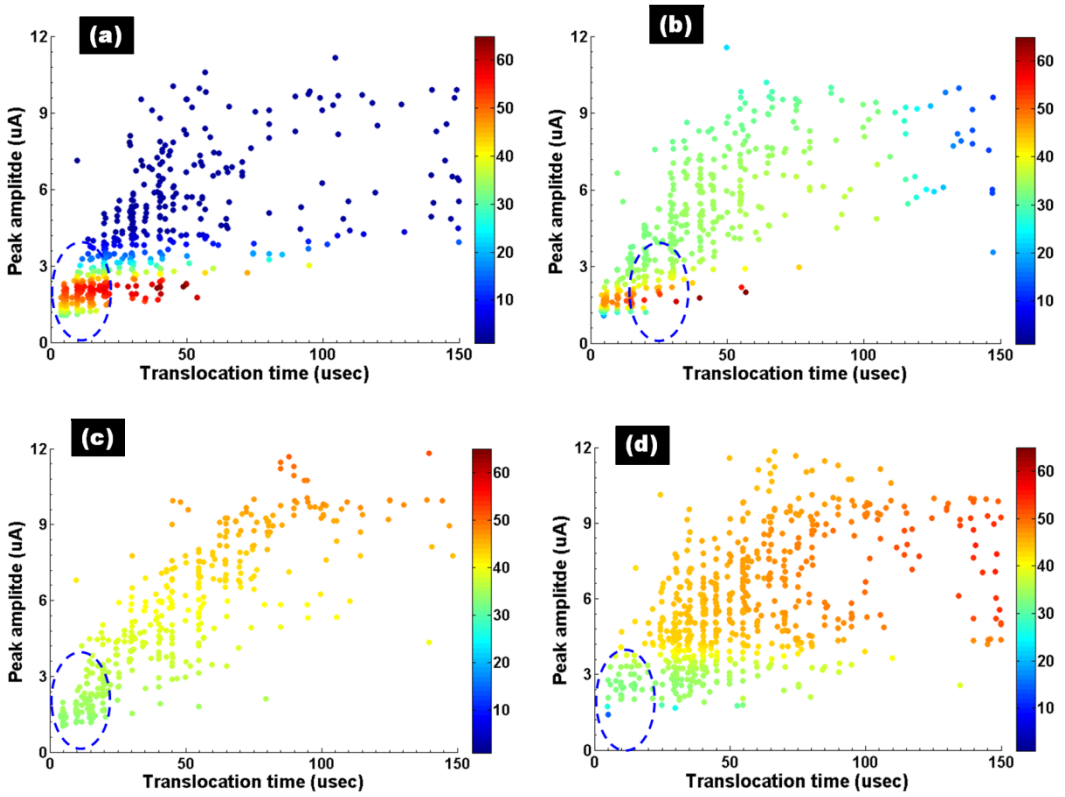

Figure 4.11 Data density plots for cell suspension with increasing relative concentration of normal urothelial (healthy) cells **(a)** 1:1 **(b)** 1:10 **(c)** 1:100 **(d)** 1:1000. The cancer cells can be identified out of a mixed cell suspension as pointed out by the dashed ovals. The color map assigns the relative data density distribution of cells.

Though biopsy samples are very important sources for diagnosing cancer but conventional pathology is limited by high clinical turnaround time, high cost, need of an experienced pathologist, probability of erroneous results and lack of statistical behavior from single cells. Our device has the potential to overcome all these shortcomings by detecting cancer cells without relying on biomarkers, cell staining or experience. Moreover, the approach is also capable to diagnose cancer at earlier stage by screening each single cell of biopsied sample which is almost impossible in recent pathological testing. The recording of cell translocation pulses provides information about cell properties and analysis gives an affirmative determination of cancer cells. One order of magnitude difference in translocation time dictates the capability of our device to undertake the highly intrinsic biomechanical properties of a cell as a robust discriminating factor for early detection of cancer. The device can also be used for cell enumeration and phenotype characterization of investigated cells.

4.4 Conclusion

We offer a novel approach to identify bladder cancer cells using solid-state micropores as the biological transducer. Biophysical properties (cellular functions, physical dimensions, rigidity, growth rate, cytoskeleton) of cancer cells significantly vary from normal cells. PDMS microchannels demonstrated significant difference in viscoelastic nature of bladder cancer cells and normal urothelial cells. The micropore device records the current blockage pulse for the translocated cell. The data not only discriminates the cancer cells but also provides statistical analysis of every cell in the investigated sample. High throughput, efficient detection, low price, statistical analysis of each cell, reliability, no cell staining and utility of an inherent cell marker make our device a better alternative for early cancer diagnosis and offers new investigations into other cellular processes that involve the mechanical properties of cytoskeleton.

CHAPTER 5

PARALLEL RECOGNITION OF CANCER CELLS USING MICROPORE ARRAY ASSEMBLY

5.1 Introduction

Circulating tumor cells (CTCs) are believed to detach from the primary tumor and spread through blood circulation to secondary tissues [184]. The shredding and accumulation of these CTCs through peripheral blood to build up a secondary tumor was initially reported in 1989 [185]. Patients with various types of cancers (breast, bladder, renal etc) have been diagnosed with CTCs in their peripheral blood [61, 186-189]. Premature recognition and accurate enumeration of CTCs in the peripheral blood cannot only help early diagnosis but also indicate the therapeutic efficiency. Reports show that number of CTCs can rise to 5000 CTCs per ml of blood in prostate cancer patients [190]. But generally, CTCs are exceedingly low in number (1-200 cells per ml) which makes it very difficult to identify and quantify them from the whole blood at an earlier stage [95, 191-193].

Various detection schemes have been employed for the isolation and quantification of CTCs including microfluidic flow cytometry, polycarbonate membrane filtration (size based separation), chromatographic isolation and use of immunomagnetic systems (magnetic dynabeads) [92, 95, 194, 195]. These techniques are mainly limited by either low throughput or use of fluorescent tags for cell quantification. Some of these strategies require expensive equipment and cannot be used in a point-of-care module [92, 196]. Immunomagnetic systems involve surface fucntionalization while other optical detection schemes require cell staining [69, 197, 198]. Size based isolation provides higher throughput but entails with laser scanning cytometry for cell enumeration which gets complicated due to retained leukocytes on the membranes [92]. Ultra-low concentration of CTCs in peripheral blood essentially calls for a

faster and efficient processing of blood sample. Fiber optic array scanning technology (FAST) has been reported as a high speed detection scheme but requires immunofluorescently labeled rare cell for scanning [199]. Electrical systems offer label-free detection of pathogens. The electrical microflow cytometers are extensively used in research and do not need fluorescent labels for cell enumeration [200]. For single cell analysis, these electrical microfluidic systems need the flow of cells in a single line fashion, which makes it a low throughput strategy.

Solid-state micropores have been deployed in a wide range of applications owing to their mechanical strength and thermal/chemical stability. Previously, Nanopores have been extensively used for biophysical analysis of DNA, proteins and other pathogens [178, 179, 201, 202]. Recently, an array of nanopores has been employed for parallel analysis of DNA to get high throughput [199]. Similarly, solid-state micropores have been reported for their use in patch clamp measurements, electroporation, cell deformability examination and size based discrimination of cells [34, 203, 204]. In our previous work, we developed a single solid-state micropore device for electrical detection of CTCs from whole blood [36]. Single channel detection faced a major challenge of high processing time. Here, we present a multi-channel device that utilizes multiple micropores for parallel recognition of tumor cells. As a model, an assay of two parallel micropores was deployed in a Teflon device assembly for simultaneous recording of ionic current passing across each of the two micropores. Figure 5.1 shows a schematic representation of the overall detection scheme for parallel processing of cells. The device was able to detect CTCs from the blood sample with 70% detection efficiency. The reported scheme distinguishes the cancer cells through a simple, inexpensive and speedy process that doesn't require any cell staining, surface functionalization or expensive equipment. The CTCs are larger in size as compared to other blood based cells and have different mechanical properties [194]. Metastasis formulates them to be even more elastic since they need to squeeze through the surrounding tissues and enter the circulatory system [30, 173].

Different morphology and biomechanical properties of CTCs discriminate them from leukocytes and give a distinctive electrical pulse signal while passing through the micropore.

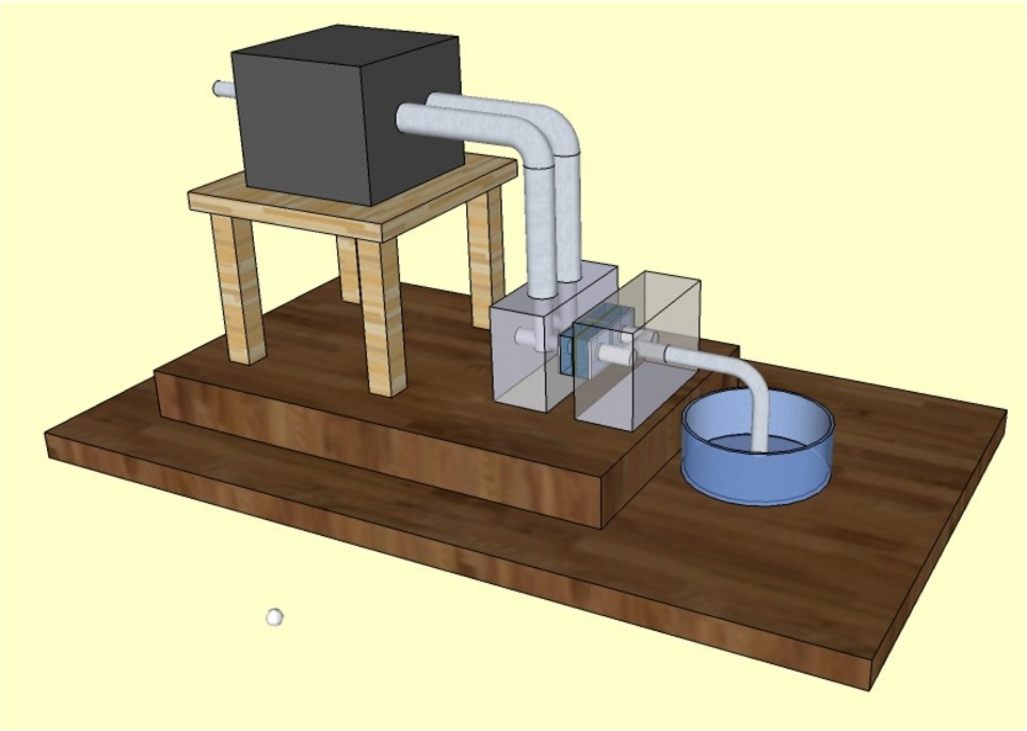

Figure 5.1 Schematic sketch to represent the overall systems with two parallel micropore channels for simultaneous recognition of tumor cells

We offer a high speed and reliable method to identify CTCs from blood. Electrophysiological DNA analysis systems make use of the charge on target molecule for translocation across the nanopore but larger mass of cells inhibits them to move under negative charge on their membrane when externally biased. Therefore, the cells were suspended in Sodium chloride (0.85% NaCl) solution and pushed under fluidic pressure. Separate Ag/AgCl electrodes were used to measure the ionic current across each micropore. Physical blockage of the micropore due to cell translocating through the micropore causes a drop in ionic current flow and an electrical pulse signal is recorded. The system is optimized for parallel recognition of CTCs and simultaneous recording of data without missing any translocation event. Tumor cells are

identified by their characteristic pulse signal. Pulse magnitude, pulse duration and pulse shape are analyzed to recognize the cancer cells. Our system can be applied to an automated and high throughput cellular analysis.

5.2 Materials and Methods

5.2.1 Fabrication of Solid-state Micropores

All the chemicals were purchased from Sigma-Aldrich (St Louis, MO, USA) unless stated otherwise. The micropore fabrication process started with thermal oxidation of a double side polished silicon wafer (100 orientation). The wafer was placed in the oxidation furnace to grow a 200 nm thick oxide layer on both sides of the wafer as explained in Figure 5.2. After piranha cleaning, positive photoresist (Shipley S1813) was spin coated on one side of the Si wafer and conventional g-line photolightography was used to open square windows. Photoresist layer was manually applied to the other side (bottom one) of the wafer to protect the oxide layer against buffered hydrofluoric (BHF) acid. The square window pattern was transferred to the underside oxide layer using BHF etching followed by removing all the remaining photoresist in acetone. Anisotropic etching of silicon was performed using diluted (25%) tetramethylammonium hydroxide (TMAH) which was maintained at 90 ^{o}C during the etching process. The silicon wafer was etched through the whole wafer thickness until it reached the other side oxide layer and gave 200 nm thick free-standing SiO_2 membranes as shown in Fig 5.2(e). Focused ion beam (FIB) was deployed to drill 20 μm sized micropore in each of the membranes. The diameter of the drilled micropore was controlled by the FIB dose (milling current, drilling time). Membrane material and the thickness of the membrane also affect the diameter of the micropore [178, 179]. Higher dose gave a larger pore for oxide membranes of similar thickness. The scanning electron microscope (SEM) analysis showed that inner periphery of the micropore was not smooth and could rupture the cell membrane while translocating through the micropore. Secondly, crimped topography of membrane confirmed the residual stress in the oxide

membrane. Therefore, the SiO_2 membranes were annealed at 1050 ^{o}C for 5 minutes. Thermal treatment made the inner walls of the micropore smoother and reduced the residual stress in the membrane. Figure 5.2(f) shows SEM micrograph of a micropore after thermal treatment.

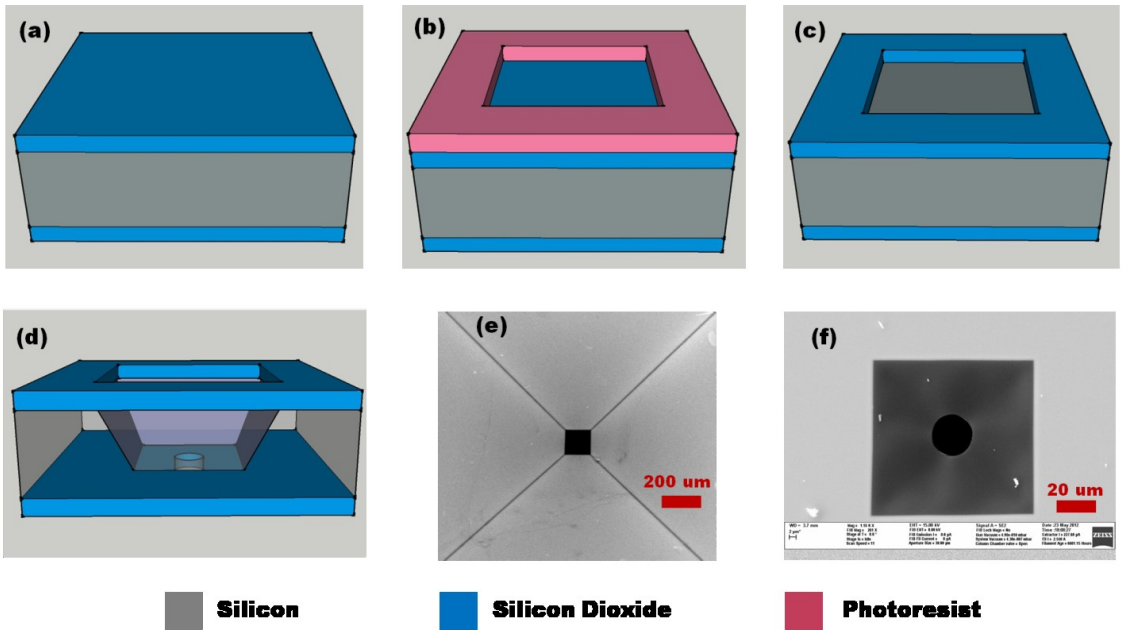

Figure 5.2 Process flow for solid-state micropores fabrication (a) 200 nm thick oxide layer grown on both sides of double side polished silicon wafer (b) Photolithography to open square windows in the spin casted photoresist layer (c) Transfer of square window pattern to the underlying oxide layer by using BHF etching (d) Anisotropic etching of Si using TMAH which performs V-groove etching to get oxide membrane on the other side of the wafer (bottom side). FIB is used to drill micropore in the membrane diaphragm (e) SEM micrograph shows slanted sidewalls of Si ending at oxide membrane resulted from TMAH etching (f) SEM micrograph of a thermally annealed micropore drilled in the oxide membrane

5.2.2 Multichannel Micropore Device Assembly

The multichannel micropore device was carefully designed for parallel processing of investigated sample. Two Teflon blocks (inlet, outlet) were used to sandwitch the micropore array. The inlet block had two channels ending in 1mm hole where as the outlet block also had two 1mm openings which come together to form a single outlet chamber. The openings

perfectly aligned together when the two blocks were assembled together. Figure 5.3 illustrates the design for multichannel micropore Teflon device assembly.

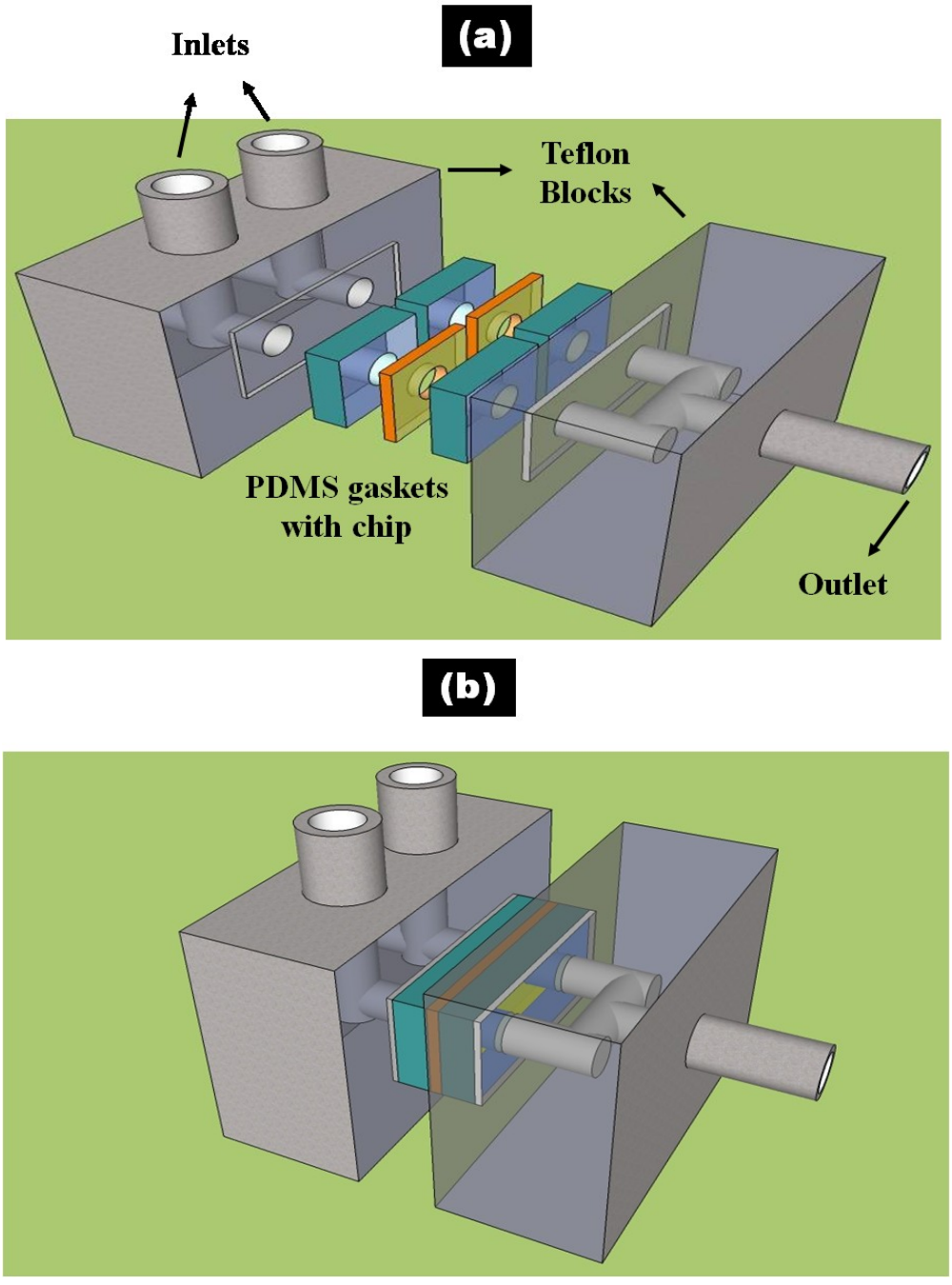

Figure 5.3 Schematics to represent the design of multichannel micropore Teflon device (a) Before assembled together (b) After assembled together

The device was designed to hold individual chip for each micropore in the array for two key motives. First, aligning all the micropores against channel openings in the Teflon blocks may get tedious unless special care is taken to drill the micropores at defined positions on the membrane. Secondly, breakage/damage of a single micropore membrane will result in replacing another chip with the entire micropores array on it. Therefore, one micropore on each chip made the design more flexible and simple. The inlet compartments of the Teflon block assembly were connected to the syringe pump (Harvard Apparatus) through tubing adapters. Cells were suspended in sodium chloride (0.85% w/v) solution which was injected into the inlet compartments at optimal flow rate using the syringe pump whereas the outlet compartment was initially filled with simple sodium chloride (NaCl) solution. Polydimethylsiloxane (PDMS; Dow Corning) gaskets were used on both sides of the chip in order to avoid any leakage of the solution. Ag/AgCl electrodes were dipped in the NaCl solution to measure the ionic current flow across the micropore. Data acquisition cards (National Instruments) were connected to these electrodes for providing voltage bias and recording current measurements. Figure 5.4 demonstrates the actual experimental setup for parallel processing of cells. When a cell passed through the micropore, physical blockage of the micropore increased the resistance and a drop in ionic current flow was observed. The resistance to the flow of ionic current through the micropore is given by $R = \rho L/A$ where ρ is the resistivity of NaCl (0.85% w/v) solution, L corresponds to the thickness of oxide membrane (length of the micropore) and A represents the effective area of the micropore. Physical blockage of the micropore during cell translocation changed its effective area which subsequently altered the ionic current flow across the micropore.

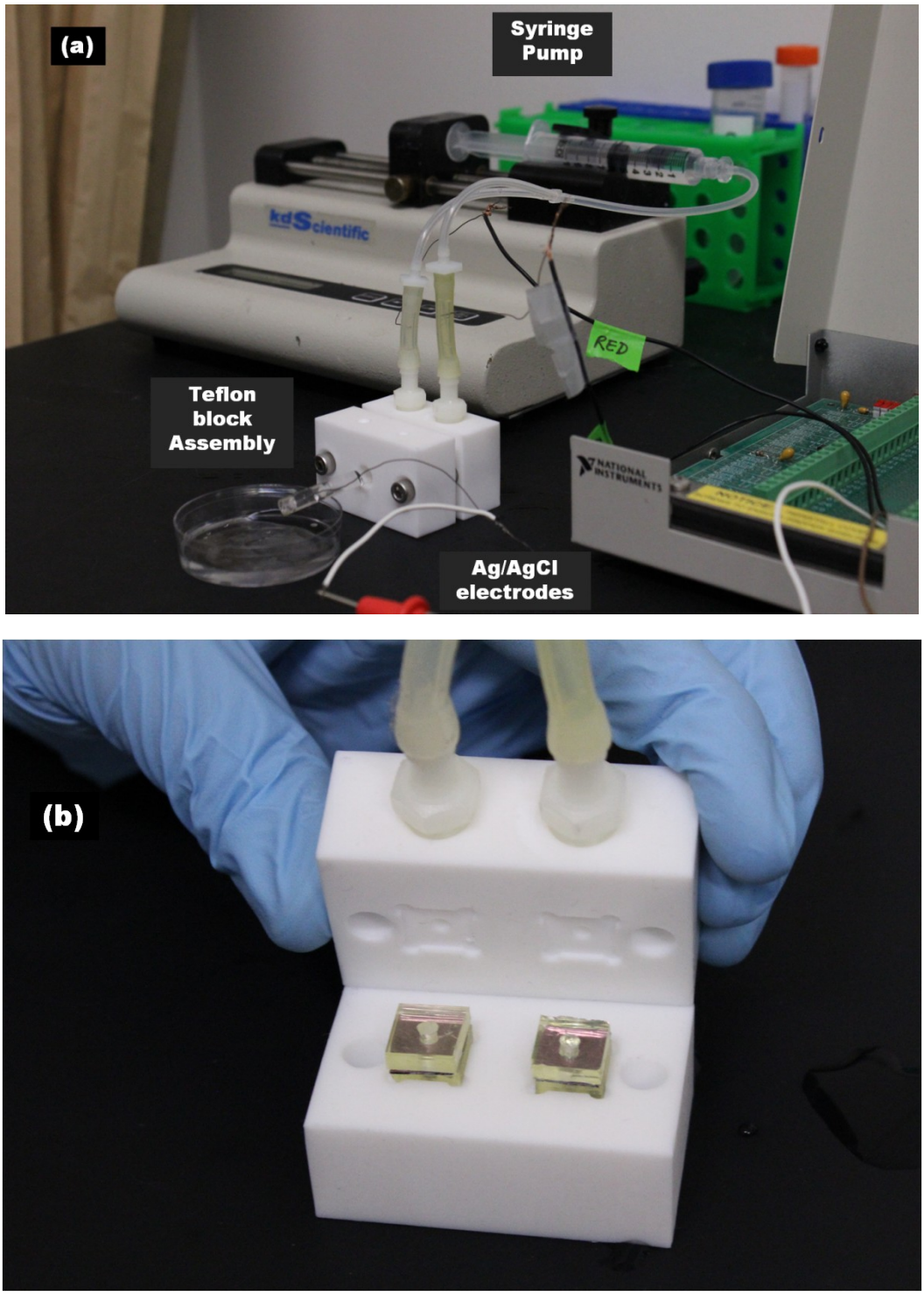

Figure 5.4 Experimental setup (a) Entire system for multichannel micropore device measurements (b) Inner view of Teflon blocks

5.2.3 Culture of Human Derived Primary Renal Cancer Cells

Renal derived cancer cells found in human brain tissues were acquired from consenting patients at the University of Texas Southwestern Medical Center at Dallas (TX, USA) with the approval of Institutional Review Board (IRB). Ice-cold Hanks medium was used to collect the brain tissues containing metastasized renal derived cancer cells which were chemically dissociated with papain (2%) and dispase (2%) as reported previously [205]. The cells were cultured with Dulbecco's modified Eagle's medium (DMEM) supplemented with 10% fetal bovine serum. The cultured cells were enzymatically dissociated with trypsin (0.25%)-EDTA (0.03%) solution to obtain the cells for the experiments.

5.2.4 Red Blood Cell (RBC) Lysis using Lysis Buffer

1x red blood cells lysis buffer was purchased from eBioscience (CA, USA). A volume of 10 ml of the lysis buffer was added to 1 ml of whole blood and the solution was incubated for 10 minutes. Then, the lysis buffer was diluted by adding 20-30 ml of 1x PBS to stop the lysing reaction. After that, the solution was centrifuged at 300-400 x g spin speed to collect the cells at the bottom of the tube in the form of the pellet. The pellet is resuspended in the desired electrolyte to process the cells with micropore device. A small volume is observed under microscope to confirm that it contains no more RBCs. Standard cell counting with a hemocytometer also confirmed about 1000 times reduction in cell density. Though the pellet collected after lysis contained only white blood cells (WBCs) but a very few residual RBCs were also observed. Since RBCs were even smaller than WBCs so these were not much significant for cancer cell identification. However, if needed; a second round of lysis can be performed. Polypropylene cell strainer (BD Falcon) with a nylon mesh (100 μm size) was deployed before processing to remove any chunks or cell clumps and ensure single cell suspension in the investigated sample.

5.3 Results and Discussion

5.3.1 Size and Shape of Cells in Suspension

The cultured renal cancer cells were trypsinized and suspended in NaCl solution for processing with our multi-channel micropore device. All the disaggregated cells held spherical shape in suspension and were found healthy after disaggregation as shown in Figure 5.5. Optical micrograph for the mixed cell suspension (Figure 5.6) provided a clear comparison of cell sizes and revealed that human primary renal cancer cells (pointed by arrow) were much larger (nearly 25 μm) in size as compared to the white blood cells (WBCs).

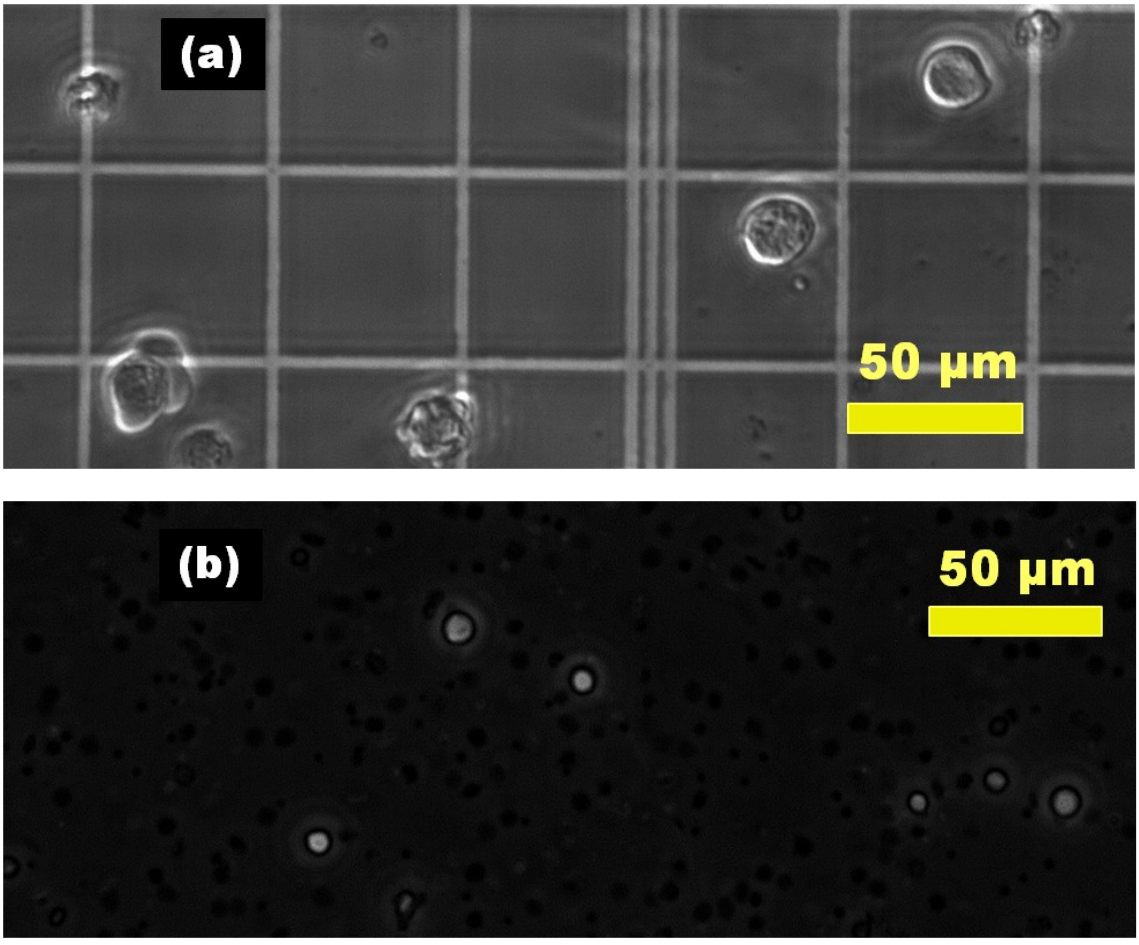

Figure 5.5 Optical micrographs of (a) renal cancer cells (b) White blood cells (WBCs). Both the cell types hold spherical shape in suspension and look healthy under microscope.

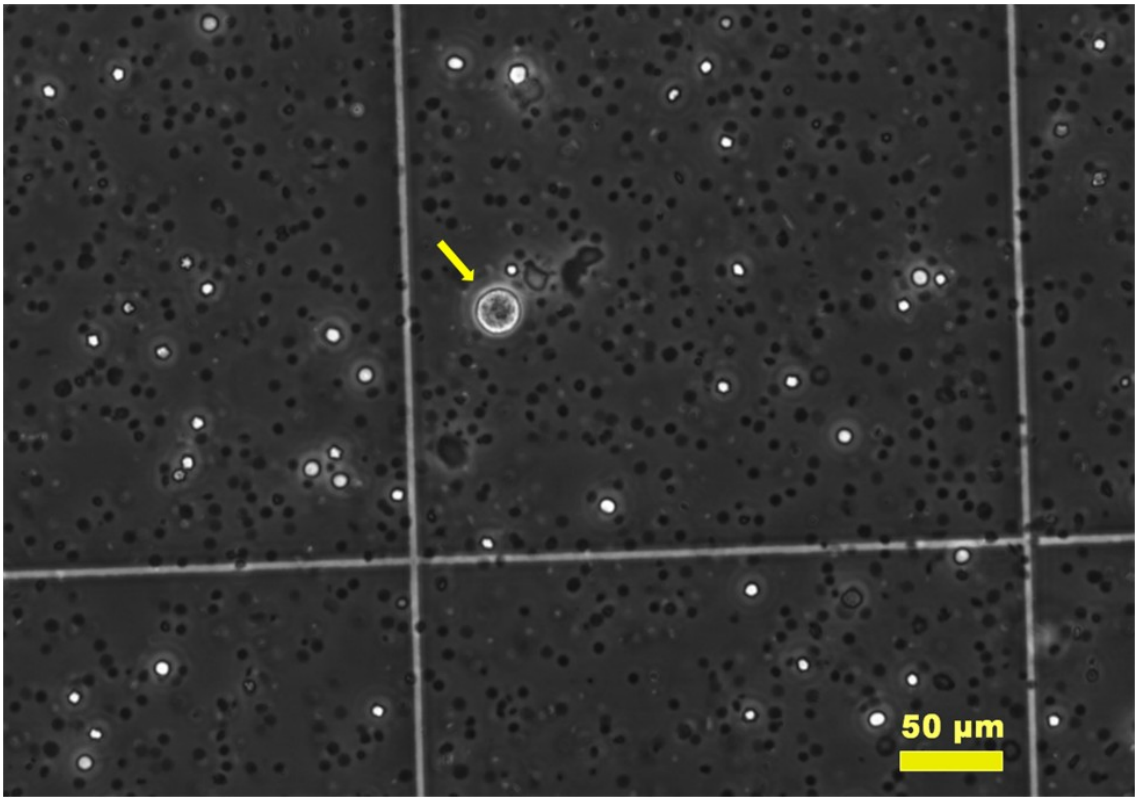

Figure 5.6 Optical micrograph of renal cancer cells and WBCs mixed cell suspension. The micrograph illustrates that renal cancer cells are larger in size than WBCs

5.3.2 Why 0.85% NaCl Solution

Phosphate buffered saline (PBS) and 0.85% NaCl solution are well recognized physiological solutions for cell suspension [36, 181, 182]. We used NaCl (0.85%) solution as the medium for cell suspension because Ag/AgCl electrodes started losing their AgCl coating which resulted in gradual drop of the baseline. NaCl solution provided enough Cl-1 ions for Ag to retain its AgCl coating and gave a much stable line. The loss of AgCl coating was evident from the whitish end of the electrode dipped in PBS solution whereas same electrodes when dipped in NaCl solution didn't lose their AgCl coating.

5.3.3 Multifaceted Optimization of Micropore-based Detection System

Multi-channel micropore device was assembled as explained in the Materials and Methods sections. The device needed to be tuned as per investigated sample requirements (cell size, cell concentration, viscoelastic behavior). Micropore diameter, membrane thickness, flow rate and sampling frequency were the critical parameters that needed to be optimized for finest results. Translocation profile of cells was significantly changed by varying any of these parameters except membrane thickness. The thickness of oxide membrane corresponded to the length of the micropore. Similar size micropores with varying membrane thickness (200, 330 and 450 nm) were used. We concluded that membrane thickness didn't affect the translocation profile much but thick membranes were more prone to micropore blockage/clogging. Thicker membrane (i.e. longer micropore) offered more area for physical contact between the cell walls and the inner hydrophilic periphery of the micropore. Probability for cell adhesion to the micropore walls was higher for longer micropore due to hydrophilic phosphate heads of the lipid bilayer. Moreover, thin membrane also ensured that only one cell would pass through the micropore at a time. Therefore, 200 nm thin oxide membrane was deployed to minimize the micropore clogging and single cell measurement at a time. The micropore diameter was also optimized to come up with the most appropriate size. Micropores with diameter less than 10 μm didn't allow the cancer cells to pass through easily and were prone to blockage. On the other hand, micropores with diameter greater than 25 μm missed some cell translocation events. So, optimal micropore diameter was investigated to be 20 μm which could record all the translocation events without getting blocked. The flow rate at which the syringe pump would inject the solution into both the parallel channels was also optimized. A flow rate greater than 30 μl/min failed to notice some cell translocation events and more than one cell attempted to enter the micropore at a time. Conversely, a flow rate less than 10 μl/min would result in a very low throughput. Therefore, the optimized flow rate was chosen to be 20 μl/min for two parallel channels. Similarly, electrical signal sampling frequency was also optimized. A lower sampling

frequency gave a stable baseline with less noise but resulted in missing some quickly passing cell translocation events. Whereas, higher sampling frequency was able to record these fast events but induced a lot of inherent noise which could suppress the desired pulse signals of smaller amplitude. The optimal sampling interval was set to be 5 μsec which translates to a sampling frequency of 0.4 MHz. At this frequency, the ionic current sample was collected after every 5 μsec. A voltage bias of 5 volts was applied across the micropore which resulted in 25 MV m^{-1} transmembrane field across the 200 nm thick membrane. This field will rapidly drop to zero within few nanometers of the membrane and would not build any gradient in the bulk solution [180]. The cell's microenvironment is also not affected by this electric field because the translocation was too fast to cause any in-house damage to the cells. The cells were observed under microscope after processing with our device and found no different from the unprocessed ones.

5.3.4 Detection Efficiency and Cell Counting

When a cell translocated through the micropore, a disturbance in the electrical signal baseline was recorded in the form of pulse signal. Since the drop in current (amplitude) and the time taken by the cell to pass through the micropore (pulse width) were strongly coupled with the biomechanical (size, shape, stiffness) properties of the cell, a characteristic pulse signal was observed for a cell type. Both the channels showed similar translocation profile for a particular cell type as shown in Figure 5.7. A high concentration (10k cells per ml) and a super low concentration (100 cells per ml) of human primary renal cancer cells were suspended separately in NaCl solution. Figure 5.8 provides a comparison of the current signals for high concentration and low concentration of cell suspension revealed that the number of pulses reflected the cell concentration and can be used for cell enumeration. It also illustrated the detection efficiency of our device that can detect a very concentration (100 cells per ml) of cells. Renal cancer cells and WBCs were processed separately for 30 minutes using the multi-

channel micropore device at optimized settings. The translocation profile was found be steady regardless of the cell concentration or the time as shown in Figure 5.9. It revealed the viability of our device for lengthy measurements.

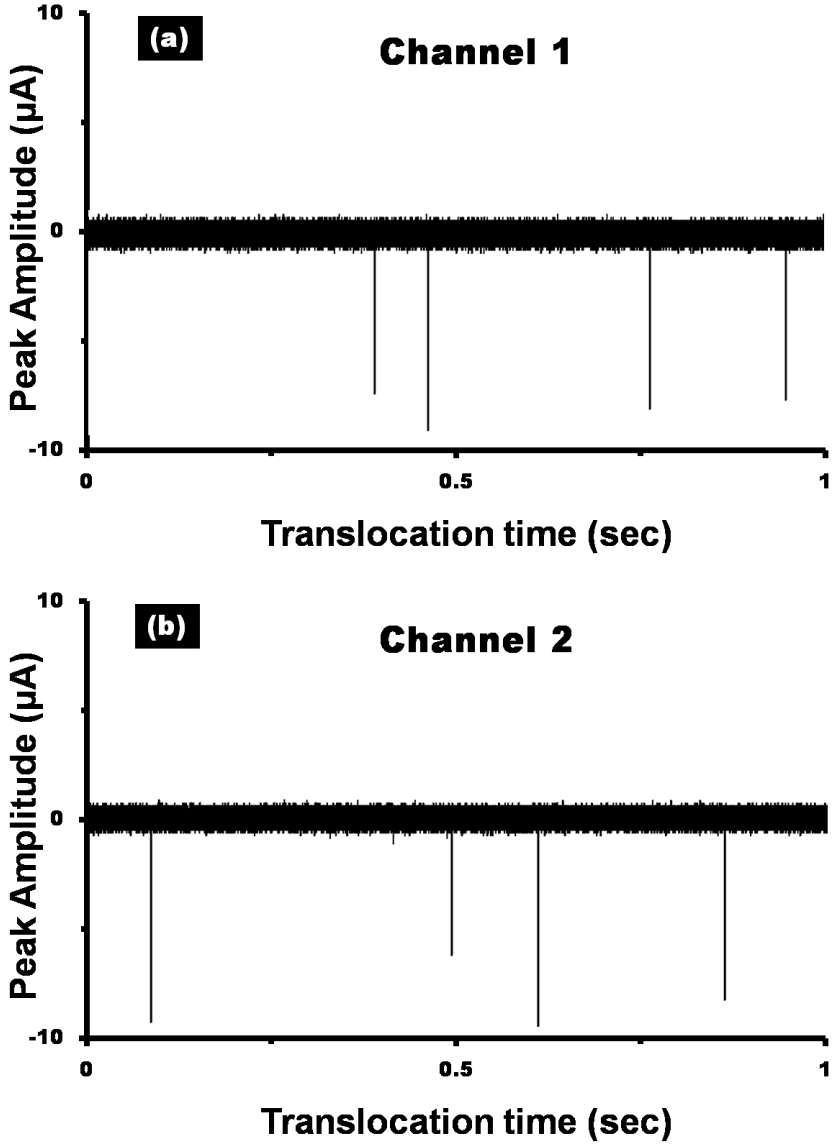

Figure 5.7 Comparison of electrical signal from (a) channel 1 and (b) channel 2 show similar pulse signals and pulse frequency during parallel processing of cell samples

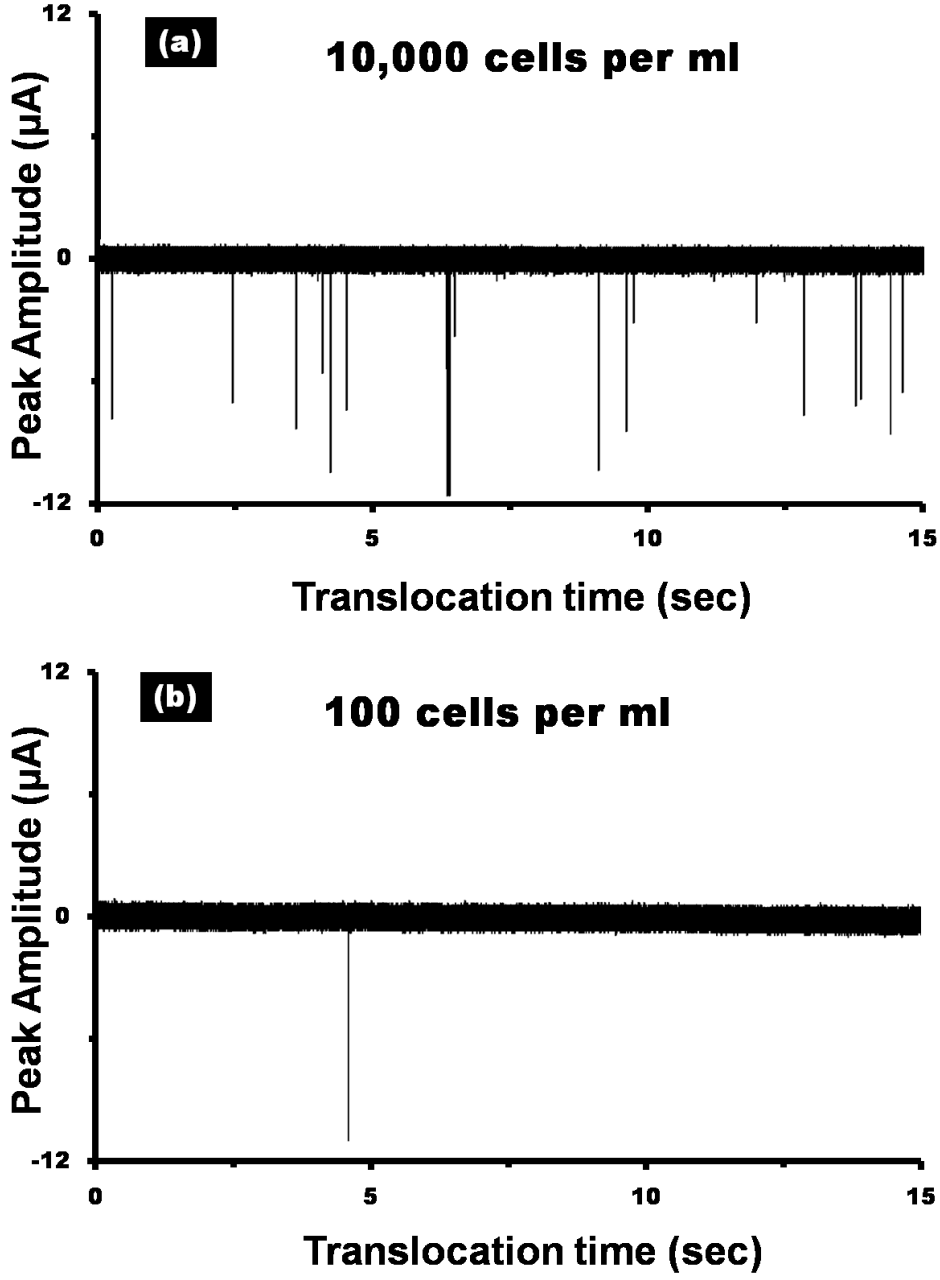

Figure 5.8 Pulse signals from (a) high concentration and (b) low concentration demonstrate the detection efficiency and capability of our device for cell counting

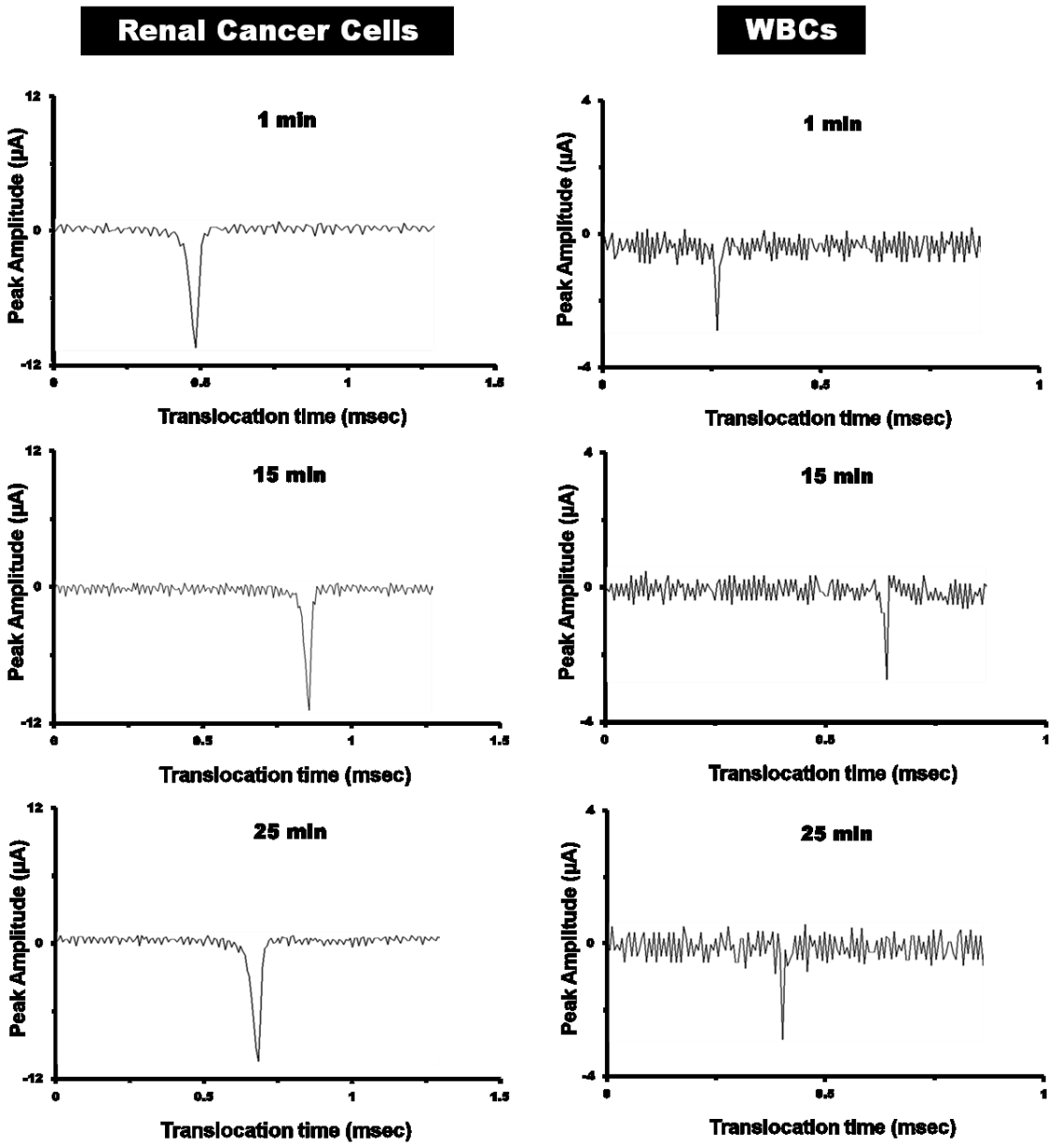

Figure 5.9 Pulse signals at different time points show that electrical signature remain identical throughout the experiment which indicates the reliability of our device.

5.3.5 Increased Throughput

The key objective of parallel recognition was to increase the throughput by rapid processing of blood samples. The whole was lysed using red blood cell (RBC) lysis buffer which

helped to get rid of RBCs. It reduced the cell concentration per ml of blood by three orders of magnitude which eliminated any need of blood dilution. In our previous work, we had to dilute the whole blood atleast 10 times to avoid blockage/clogging of micropore [36]. Dilution increased the sample volume by 10 times and furthermore single micropore measurements made it a very low throughput device. The presented scheme utilized an array of two micropores which provided two parallel channels and simultaneous recording of current measurements across each channel made it a rapid processing device. Moreover, cells collected from 1 ml of blood were resuspended in 500 µl of NaCl solution which helped to reduce the sample volume by 2 times while keeping the cell density still low enough to be processed by our device without getting blocked. Thus, just by adding one extra channel, the throughput was increased by 40 times. At optimized flow rate, it would take only 25 minutes to process 1 ml of blood.

5.3.6 Characteristic Pulse Signal for Cancer Cells

Human primary renal cancer cells gave a distinctive current blockage pulse signal. As already mentioned, WBCs were smaller in size so offered lesser physical blockage to the micropore which showed different translocation profile. The experiments were repeated atleast three times and similar results were observed. The pulse characteristics (pulse width, peak amplitude) for renal cancer cells and WBCs plotted on a scatter plot showed that cancer cells were easily identifiable as can be seen in Figure 5.10. More than 95% of cancer cells showed distinctive translocation profile from WBCs owing to their different biomechanical properties. The pulse signal from a cluster of cells could easily be identified from the pulse shape and was ignored. The characteristic pulse signals are shown closely in Figure 5.11. The pulse statistics (average translocation profile, peak amplitude) for both types of cells are shown in Table 5.1. The analysis of data based on translocation time and peak amplitude was carried out using one-

way ANOVA which showed that the two types were significantly different from each other (p-value<0.001).

Table 10.1 Translocation Pulse statistics for both cell types through 20 μm micropore by channel 1 and channel 2

Measurement (Units)➔	Average Translocation Time (μsec)		Average Peak Amplitude (μA)	
Cell Types ↓	Channel 1	Channel 2	Channel 1	Channel 2
Renal Cancer Cells	73.50 ± 18.13	78.37 ± 36.30	7.52 ± 3.44	7.69 ± 2.83
WBCs after RBC lysis	9.60 ± 6.02	9.18 ± 5.64	1.83 ± 0.47	1.84 ± 0.40

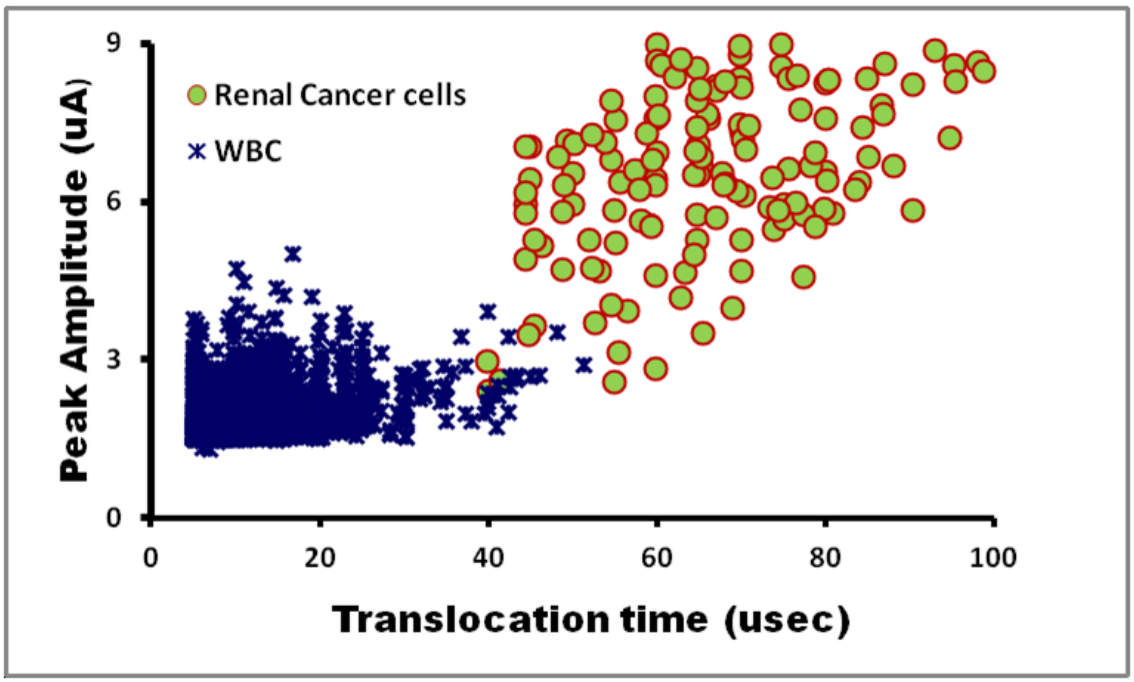

Figure 5.11 The distribution of pulses for both types of cells processed separately through the multi-channel micropore device shows clear data clusters for cancer cells as compared to white blood cells

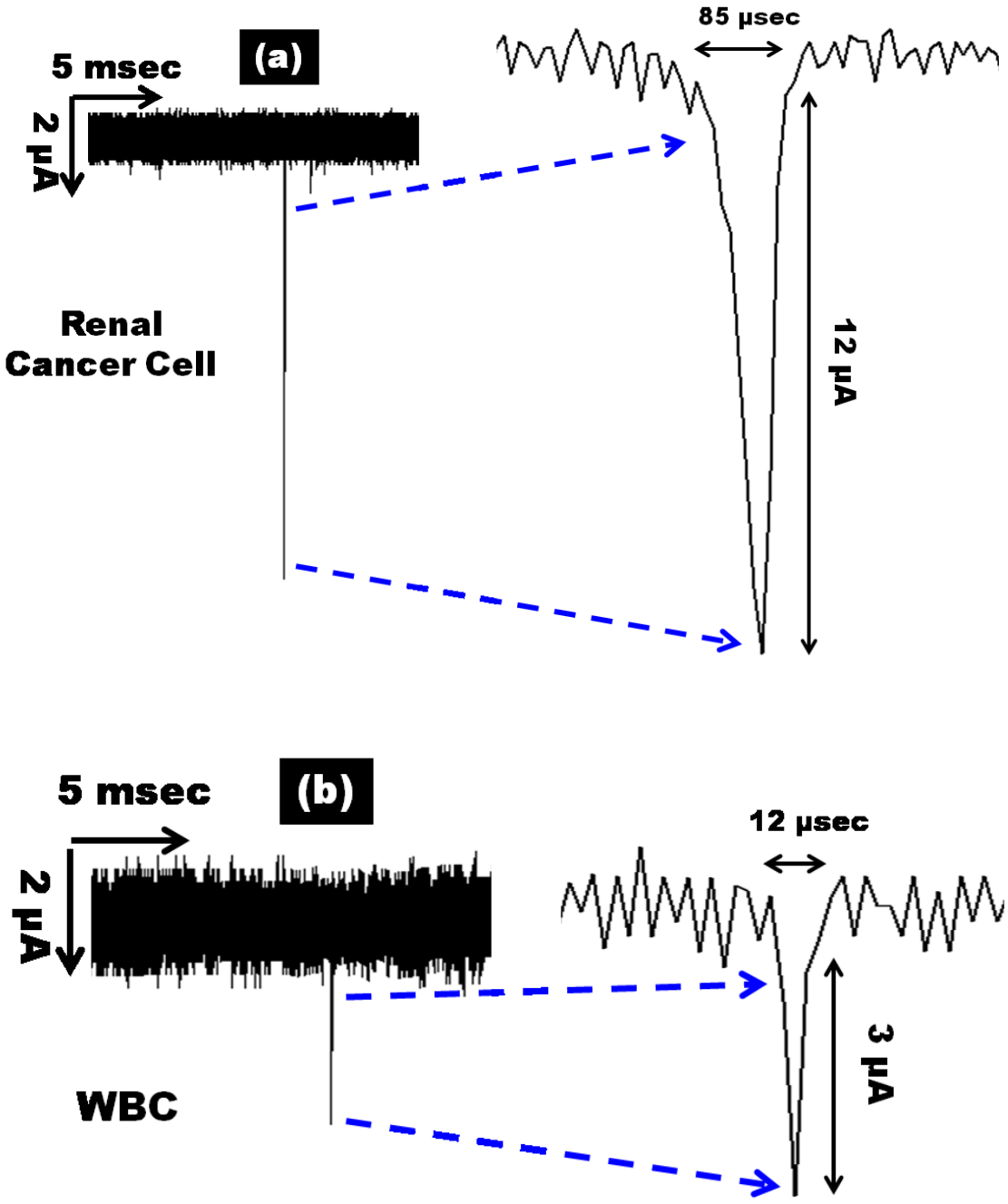

Figure 5.12 Characteristic translocation profile (translocation time, current peak amplitude) for (a) renal cancer cells and (b) WBCs facilitate cancer cell identification

The pulse shape also provided further information about the translocating cell. The orientation of the cell and its biomechanical properties predominately defined the pulse characteristics and pulse shape [36, 206]. The ionic current value corresponded to a cross sectional circular contour which indicated the physical dimension of the translocating cell. Thus, the data could be used to accurately track 3D electrical profile of the translocating cell at optimized settings of the measuring system. Moreover, the slope of the pulse signal indicates the stiffness of the translocating cell which can be used to study the biomechanical properties of the investigated cells.

5.3.7 Recognition of Cancer Cells Mixed with Blood Samples

After defining the signature pulse signals from renal cancer cells and the WBCs, a mixture of renal cancer cells and whole blood was investigated. We mixed 100 cells of renal cancer cells in 1 ml of whole blood and lysed it to get rid of RBCs. The collected pellet was resuspended in NaCl solution to get a mixed cell suspension. The RBC lysis didn't affect the cancer cells present in the blood sample and the cancerous cells were easily distinguished from WBC with a detection efficiency of more than 70%. Human primary renal cancer cells were processed in mixed suspension with freshly collected rat blood as well as human whole blood. The data demonstrated that cancer cells were effortlessly identified from rat and human whole blood even when they were mixed at a very low concentration (100 cells per ml) as shown in Figure 5.12. It validated the efficacy and viability of our device for CTC detection at an earlier stage. Our device provided parallel recognition of cancer cells, enumerated the number of cells present and can potentially trail the 3D electrical profile of the translocating cells.

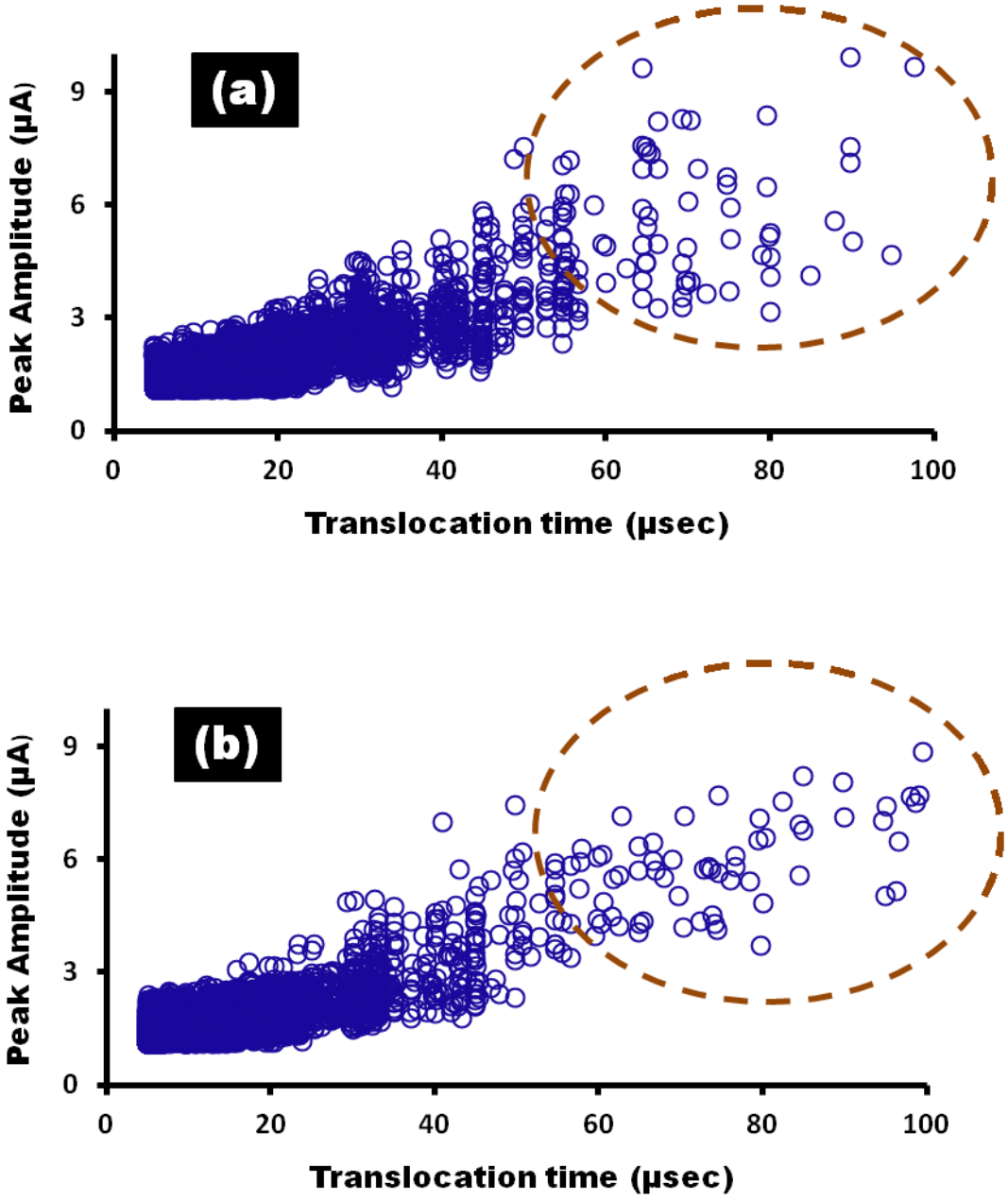

Figure 5.13 Scatter plots for cancer cells mixed with freshly collected (a) rat blood and (b) human whole blood demonstrate that characteristic current signal discriminates cancer cells from WBCs and can be efficiently recognized out of a mixed cell suspension as pointed out by the dashed ovals.

5.4 Conclusion

A novel and fast processing detection scheme to identify cancer cells from whole blood sample using solid-state micropore array is presented. An array of micropores with simultaneous recording of data for parallel recognition of cancer cells resolved the key challenge for single solid-state miropore devices. The throughput can be increased by adding more micropores in the array to make the processing even faster. The cells were pushed under optimized fluid pressure to record electronic signatures for one cell at a time. The biophysical properties of cells gave a characteristic pulse signal which discriminated the cancer cells from other cell types. Our multi-channel micropore device didn't need any cell staining, surface functionalization or expensive equipment. It not only efficiently detected the cancer cells but also provided statistical analysis of every single cell in a high throughput fashion. The system is also capable to investigate other samples where biomechanical properties of cells can be used as the discriminating factor to indicate the physiological state of the cells.

CHAPTER 6

SYNTHESIS OF POROUS PLGA NANOPARTICLES FOR DRUG DELIVERY SYSTEMS

6.1 Introduction

Over the last few decades, there has been increased interest in developing biodegradable micro/nanoparticles for drug delivery applications. Among the new drug delivery systems, polymeric nanoparticles have emerged as promising carriers for sustained release of bioactive agents. The increased surface area offered by small particles makes these exceedingly effective for targeted drug delivery [207-209]. It has also been reported that nanoparticles can offer elevated drug content inside the neoplastic cells by prevailing over the multidrug resistance [210, 211]. The increased focus on deploying nanoparticles in drug delivery systems is due to the ease of their preparation with well-defined biodegradable polymers (like Poly(lactic-co-glycolic acid) (PLGA)), low cost and highly stable behavior in biological fluids [212, 213]. The destiny of nanoparticles in any drug delivery system is also an important concern during development process.

The controlled and targeted release coupled with therapeutic mechanisms significantly impacts the quality of the drug by eliminating the potential of both under and overdosing. PLGA offers many possibilities to accurately control the resulting drug release kinetics over periods of days to months and easy administration using standard syringes and needles. But drug stability and accelerated polymer degradation due to autocatalytic effects are the major concerns in non-porous PLGA-based particles [118]. Porous drug delivery systems can overcome these autocatalytic effects by increasing the diffusivity of the molecules [119]. Thus, PLGA based porous particles can be very helpful to optimize the therapeutic efficiency of medical treatments and to reduce serious side effects [122]. Porous nanoparticle systems exhibit much better flow

and aerosolization efficiency during pulmonary administration when compared to non-porous nanoparticles [120, 121]. For drug release study porous and non-porous PLGA nanoparticles are widely studied. Pore characteristics have significant impact on drug release and by controlling pore morphology, it is possible to design highly controlled drug release systems [122]. Herein, we describe salt-leaching technique where trapped salts are extracted out at a later stage to prepare porous polymeric drug delivery system with prolonged and controlled drug release properties. Figure 6.1 shows a schematic drawing to represent the synthesis technique.

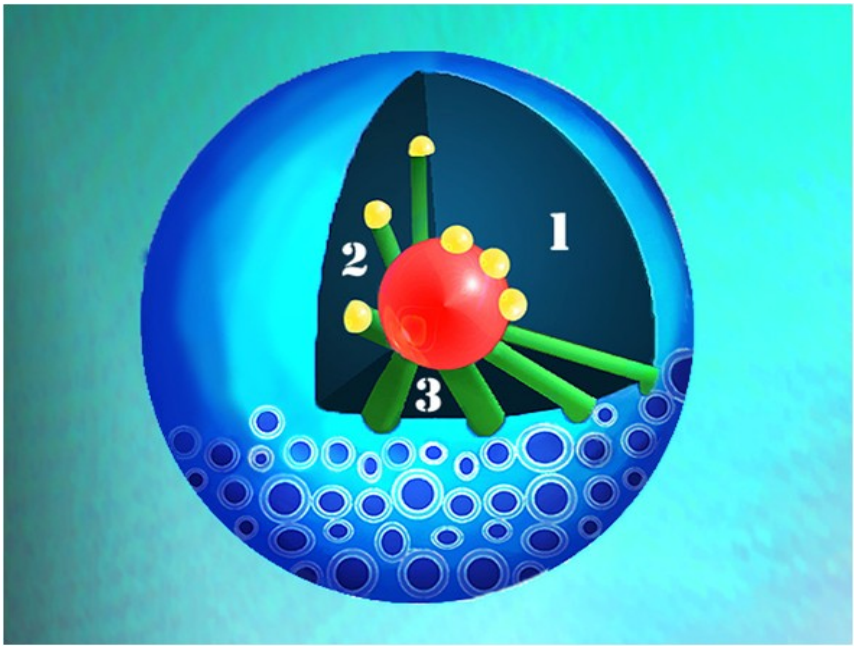

Figure 6.1 Graphical representation of the slat-leaching process to give porous features on the surface of nanoparticles when the entrapped salts are eventually extracted out.

Poly(lactic-co-glycolic acid) (PLGA) is a biocompatible and biodegradable copolymer which is synthesized by means of ring-opening copolymerization of two different monomers; glycolic acid and lactic acid. The biodegradation, biocompatibility and tissue reaction of PLGA is documented in different investigations [214, 215] and numerous polymeric devices like microspheres, microcapsules, nanoparticles have been synthesized using PLGA to deliver

variety of drugs [216]. These PLGA nanoparticles are prepared either by using single emulsion or double emulsion methods. Single emulsion method is a straightforward process where only one water phase solution is cross-linked with oil phase solution. Water-in-oil-in-water (w/o/w) double emulsion method incorporates dispersed oil beads containing smaller aqueous globules. The particles obtained by this technique provide a great opportunity for the controlled release of chemical species initially entrapped in the internal globules [217, 218]. Such double compartment structures can be considered as reservoirs of encapsulated materials to be released under certain conditions. Double emulsion materials are generally prepared with two surfactants of opposite solubility. In order to prepare a w/o/w emulsion, a hydrophilic surfactant is first dissolved in oil and then water is added to form w/o emulsion. The solution is then emulsified again in an aqueous solution to produce a w/o/w double emulsion.

Serum albumins are very significant water soluble protein constituents of the circulatory system which perform many physiological functions [219]. Albumins are profusely found in body fluids and tissues of mammals. Albumins mainly regulate the colloidal osmotic pressure of blood. Though albumins are readily soluble in water yet high concentrations of neutral salts like ammonium sulfate can help precipitation [220]. Bovine serum albumin (BSA) also known as Fraction V, is one of these serum albumins which is a commonly known hydrophilic drug. BSA finds its use in a wide range of applications due to its stability, low cost and no side effect in most of the biochemical reactions.

Chloroform ($CHCl_3$) is a colorless, sweet smelling but somewhat hazardous liquid which is widely used as organic solvent in research because it is fairly unreactive, conveniently volatile and effortlessly miscible with other organic solutions. Chloroform is also obtained from seaweeds but commercially produced by heating a mixture of chlorine and methane. The reaction occurs at 400-500 ^{o}C where progressively more chlorinated compounds are produced due to free radical halogenations process as shown below

$$CH_4 + Cl_2 \longrightarrow CH_3Cl + HCl$$

$$CH_3Cl + Cl_2 \longrightarrow CH_2Cl_2 + HCl$$

$$CH_2Cl_2 + Cl_2 \longrightarrow CHCl_3 + HCl$$

Nanoparticles have been identified as important drug carrier nanovehicles where therapeutic and diagnostic agents are encapsulated, covalently attached, or adsorbed on to the surface of such nanocarriers. Research into rational and controlled drug delivery has resulted into hollow nanospheres and porous nanoparticles. Porous nanoparticle systems can be made of various materials, prepared in a variety of different ways, and designed to deliver drugs to specific parts of the body. Porous nanoparticles can vary from 25 nm to several hundred nm of diameter [120]. Owing to high chemical and thermal stabilities, enhanced surface areas and fine compatibilities with other materials, porous nanoparticles are widely used as inorganic carriers for biological reagents [221]. Porous nanoparticles have proven to be robust drug delivery systems that can facilitate a controlled release of encapsulated drugs of varying chemistry and molecular weight into biodegradable nanoparticles.

Various approaches have been deployed to synthesize porous micro/nanoparticles which incorporate the use of poly(acrylic acid), Pluronic F-127 or ammonium bicarbonate as the porogen reagent [123, 125, 222]. These chemical species are either limited by their physiochemical properties, high price or need for thermal curing. We offer a simple and straightforward method which may empower us to use a wide range of cheap, easily obtainable water-soluble salts as extractable porogens. Such a rapid, inexpensive and simple technique with potential for a variety of alternative materials as porogen, can improve the controlled drug delivery systems to a large extent.

In this study, porous and non-porous PLGA nanoparticles containing BSA were prepared by water-in-oil-in-water (*w/o/w*) double emulsion method using sodium bicarbonate as the extractable porogen. The porous nanoparticles showed increased and sustained drug release than the non-porous ones. The particle size, size distribution, porosity, stability, drug

loading efficiency and drug release behavior were characterized. BSA was used as a model drug to study *in vitro* drug release behavior. The protein release studies were carried out using bicinchoninic acid (BCA) protein assays. Standard curves were plotted to determine the amount of the drug loading and release.

6.2 Materials and Methods

6.2.1 Chemicals

All the chemicals were purchased from Sigma-Aldrich (St. Louis, MO, USA) unless otherwise mentioned. There were three major experimental goals achieved in succession. The first section details the synthesis of drug loaded porous and non-porous nanoparticles. The second step elucidates drug loading and loading efficiency. The third and most important part demonstrates the drug release studies of the nanoparticles.

6.2.2 Preparation of BSA Loaded Porous and Non-porous PLGA Nanoparticles

Porous and non-porous PLGA nanoparticles were synthesized by water-in-oil-in-water (*w/o/w*) double emulsion technique. Twenty mg of the hydrophilic BSA was dissolved in 0.2 ml of deionized (DI) water to make the water phase of the solution (w_1). In parallel, 90 mg of PLGA was dissolved in 3 ml of chloroform to make 3% PLGA solution, forming the oil phase solution (*o*). Then 1 gm of polyvinyl alcohol (PVA) was dissolved in 20 ml of warm (50 °C) DI water to make 5% aqueous PVA solution that formed the second water phase solution (w_2). Each of the solution was vortexed to ensure that the reagents were mixed well. Now, the BSA solution (w_1) was added to the PLGA solution and vortexed for 30 seconds to make water-in-oil phase. In order to prepare porous nanoparticles, 2 mg of sodium bicarbonate was mixed in 1 ml of DI water to form the porogen solution. This solution was immediately added to the above water-in-oil solution to introduce pores on the particles. These pores would be formed at a later stage due to salt-leaching. This step of adding sodium bicarbonate solution was skipped for the preparation of non-porous nanoparticles as shown by the schematic flowchart in Figure 6.2.

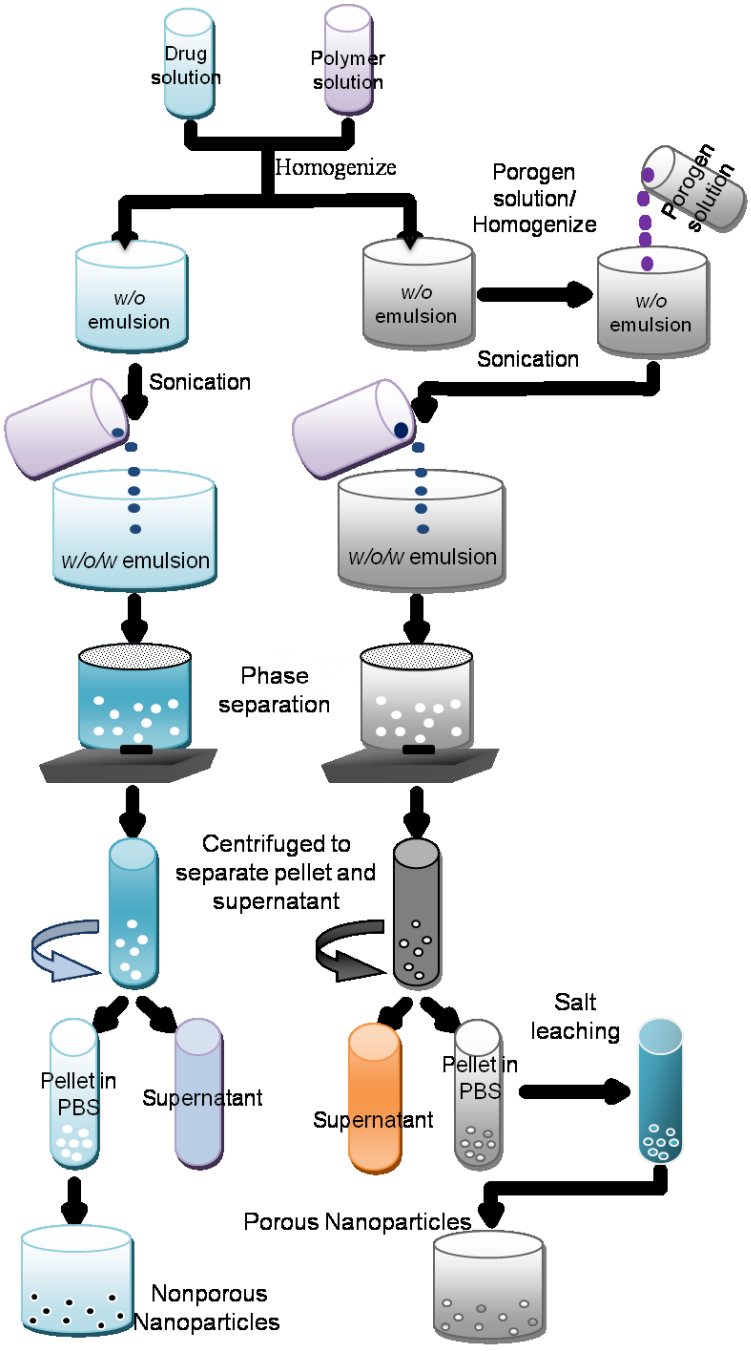

Figure 6.2 Schematic flowchart demonstrates the step-by-step process to synthesize porous and non-porous PLGA based nanopraticles.

The solution was then sonicated for 1-2 minutes at 40 W. After that, the solution was added drop-wise to the stirring beaker of aqueous PVA solution thus forming water-in-oil-in-water phase. The resultant solution was then emulsified by sonication for 2 mins at 40 W. Next, the mixture was gently stirred overnight in a chemical hood allowing the chloroform to evaporate. Once the chloroform evaporated completely, the solution was transferred into a 50 ml tube and centrifuged at 4000 rpm for 15 min. The supernatant was collected and frozen for calculating the loading efficiency at later stage. The pellet was resuspended in 5 ml PBS and vortexed for 1 minute. The resulting solution was frozen at -80 °C and then freeze dried to get the nanoparticles after recording the dynamic light scattering (DLS) readings to measure the size and polydispersity of nanoparticles using a ZetaPALS DLS detector (Brookhaven Instruments, Holtsville, NY). In order to get the porous nanoparticles, the freeze dried particles (white in color) were taken in a plastic tube and 3 ml of DI water was added to perform salt leaching. The tube was vortexed again and centrifuged at 4000 rpm for 15 min. This step was repeated three times to ensure that no salt was left behind. The supernatant during salt-leaching process was also collected and frozen to study the possible drug released during salt-leaching process as the loaded drug (BSA) was hydrophilic.

6.2.3 Scanning Electron Microscope (SEM) Imaging of PLGA Nanoparticles

The freeze dried nanoparticles were suspended in DI water and diluted 10X to reduce their density on the substrate surface used for imaging. DI water was used instead of PBS to avoid any contamination from the salts present in PBS solution. The solution was then poured on the top of autoclaved glass cover slips and was left overnight to dry in nitrogen ambient. The samples were then sputter coated with 50 Å thick gold to prevent the surface from getting charged during electron microscopy. The thin layer of gold made cover slip surfaces conductive enough to image with SEM. Figure 6.3 shows the SEM micrographs of porous and non-porous nanoparticles.

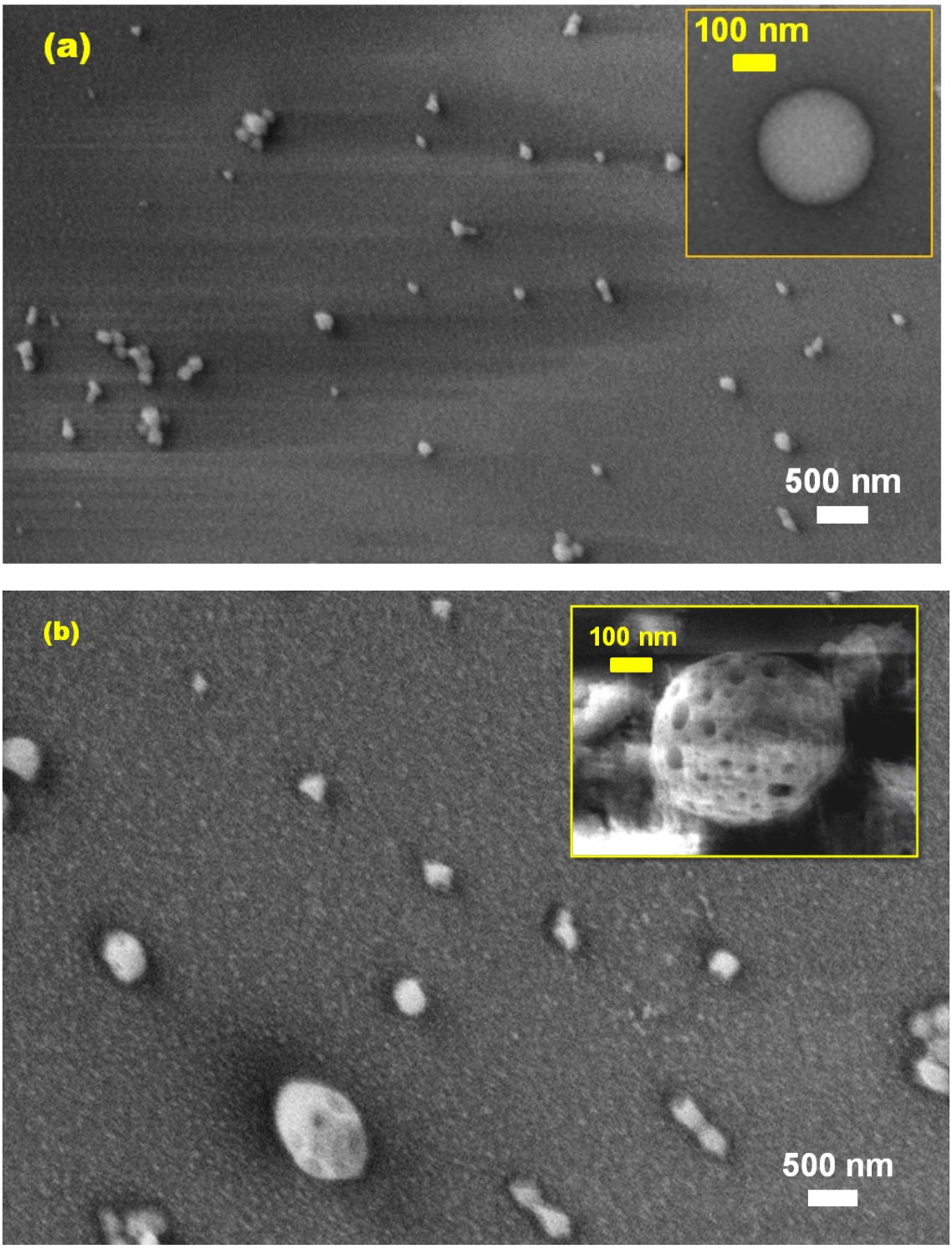

Figure 6.3 SEM micrographs for (a) non-porous and (b) porous nanoparticles. The insets show the magnified view of the nanoparticles.

6.2.4 Indirect Method for Drug Loading Efficiency

The drug loading efficiency was determined using the indirect method. The supernatant collected and frozen in the previous steps were used to calculate the loading efficiency. Indirect method relies on the protein present in the supernatant solution. Instead of direct investigation of the amount of drug loaded in the nanoparticles, we calculated the amount of drug present in the supernatant using the standard curve. The drug present in supernatant solution reflected the amount of unloaded drug which was subsequently used to calculate the loaded drug using the indirect method. Loading Efficiency was calculated using the formula given below:

$$Loading\ Efficiency\ (\%) = \frac{A - B}{A} \times 100$$

Where *A* represents the amount of original drug and *B* refers to the amount of drug present in the supernatant.

6.2.5 Drug Release from BSA Loaded Nanoparticles

In order to monitor protein release from BSA loaded nanoparticles, these were placed in a 100 kDa molecular weight cut-off dialysis bag (Spectrum Laboratories Inc., Rancho Dominguez, CA). Porous and non-porous nanoparticles were separately mixed in 2 ml of PBS and were put in different bags. Each dialysis bag was immersed in 10 ml of PBS solution which was the dialysate. Three replicates for both types of particles were prepared to study the drug release activities. Drug release studies were performed by measuring BSA release at predefined time points: 1, 5, 7, 11, 14, 18, 22 and 30 days. At each time point, the PBS solution was replaced by fresh PBS solution keeping the volume unchanged and the collected samples were stored at -20 °C for further analysis.

At each time point, 3 samples (one from each replicate) were collected to get a more reliable release data. After collecting all the samples for porous and non-porous PLGA nanoparticles, Pierce BCA protein assay (Fisher Scientific, Hampton, NH) was used for quantitative analysis of the drug release. The working reagent consisted of reagent A and

reagent B at the ratio of 50:1 where BCA was used as reagent A and copper sulphate as reagent B. A 200 µl volume of the working reagent and 25 µl of PBS (containing BSA obtained from collected samples) were added to each well for respective measurements of porous and non-porous nanoparticles drug release behavior. After adding all the stored samples collected at predetermined time points to the BCA containing wells, standard solutions were also added on the same well plate, with gradually reducing concentrations of BSA to determine the standard curve. The well plate was then covered with the aluminum foil and kept in the incubator at 37 ^{o}C for 30 minutes. In the presence of protein, the color of the solution changed from blue to purple. Absorbance was recorded using spectrophotometry (Infinite M200 plate reader, Tecan, Durham, NC) at wavelength of 562 nm. Absorbance values for the standard concentration values provided a standard curve that was then used to calculate the concentration of BSA protein released. The percentages of protein release was calculated using the following equation

$$percentage \quad of \quad protein \quad release = \frac{X}{Y} \times 100$$

where *X* indicates the amount of released protein and *Y* represents the total amount of loaded protein.

With the obtained values, percentage of cumulative protein release was calculated and plotted against the administered time points. The standard deviations of the absorbance at each time point were also plotted on the same graph to demonstrate the precision of the data.

6.3 Results and Discussion

6.3.1 Characterization of Synthesized Nanoparticles

After preparation of the nanoparicles, laser scattering measured by zeta potential analyzer was used to determine the particle size distribution, polydispersity, zeta potential and mean particle diameter. The average diameters for porous and non-porous PLGA nanoparticles

were found to be 525.2 nm and 321.8 nm respectively (see Table 6.1). The morphology of PLGA nanoparticles was found to be spherical from SEM micrographs. The size of the non-porous nanoparticles was found to be smaller than the porous nanoparticles and the size distribution was also observed to be more uniform in case of non-porous nanoparticles as illustrated in Figure 6.4.

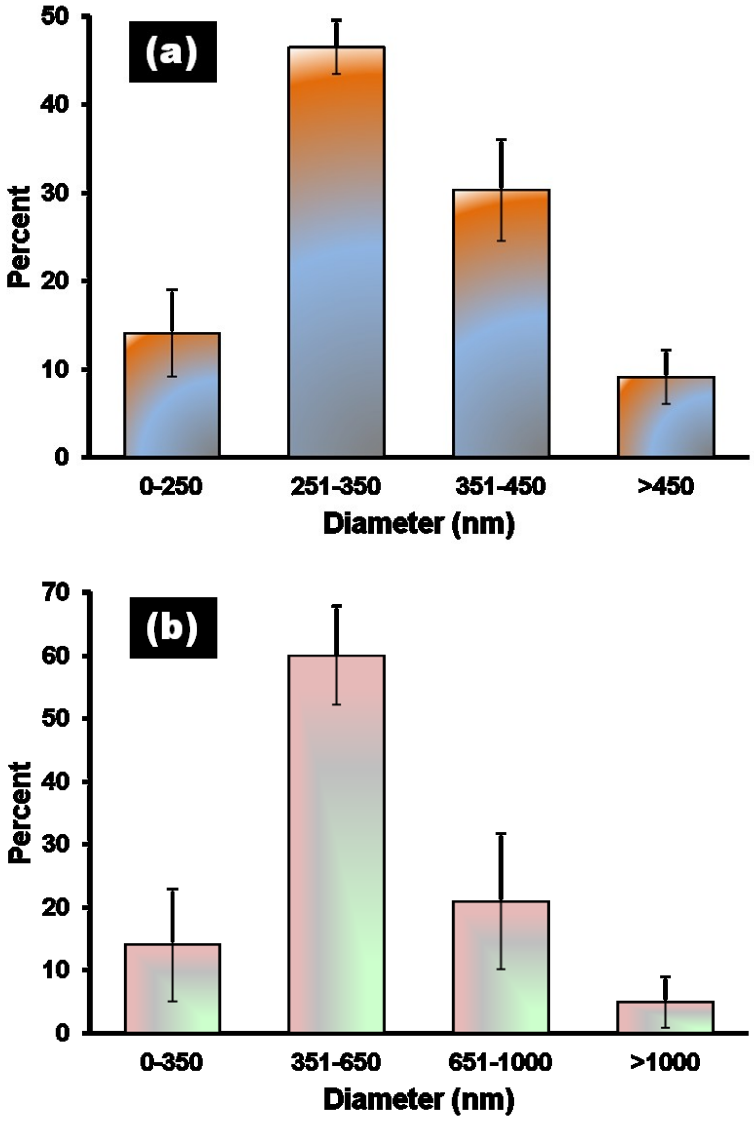

Figure 6.4 Size distributions of PLGA nanoparticles (a) BSA-loaded non-porous PLGA nanoparticles with average diameter of 321.8 nm. (b) BSA-loaded porous PLGA nanoparticles with average diameter of 525.2 nm

The porous nanoparticles were expected to be larger than the non-porous nanoparticles in line with previous reports [120]. The larger sizes of the porous particles were due to sodium bicarbonate incorporation which later leached out, leaving porous features on the particle surfaces. The porosity, pore sizes and distribution of pores on the porous PLGA nanoparticles can be controlled by using different concentrations of the porogen [123]. Here a single concentration of porogen was used because the main focus was to establish salt-leaching as a novel technique to prepare the porous nanoparticles. The pore size was estimated to be 30-60 nm from SEM data.

Polydispersity index, a dimensionless number, is used to gauge the particle size distribution. Its value may vary from 0.01 (monodispersed particles) to 0.7 (particles with fluctuating size distribution) [211]. Particles with broadly varying size distribution indicate polydispersity index >0.7 [223]. Polydispersity of both types of nanoparticles is summarized in Table 6.1 which clearly shows that both types of nanoparticles had polydispersity index much less than 0.7. Porous PLGA nanoparticles exhibited higher polydispersity index value which might have stemmed from the uncontrolled vortexing of porogen solution in *w/o* phase solution while synthesizing the nanoparticles.

The stability of the particles in solution is very important for biological applications that incorporate colloidal suspensions. Particle composition and the medium in which these are dispersed, determine the zeta potential (ζ) of the particles. High surface charges (ζ > ±30 mV) prevent particle aggregation and thus make the particles highly stable in the colloid suspension [224]. Particles with surface charges (ζ > ±10 mV) are also relatively stable whereas (ζ < ±10 mV) allows the particles to flocculate due to small repulsive effect [225]. In this work, we used PLGA with carboxylic acid end groups (-COOH) on it and the presence of carboxyl groups on the PLGA nanoparticles surface passed on negative charges which was confirmed by the ζ values recorded for porous and non-porous PLGA nanoparticles. Though the zeta potential for

the nanoparticles was less than –30 mV, but still it was high enough to give reasonably good colloidal properties.

Table 6.1 Characteristics of BSA loaded porous and non-porous PLGA nanoparticles

Property	Non-porous PLGA Nanoparticles	Porous PLGA Nanoparticles
Porogen concentration (% w/v)	0	0.2
Average diameter (nm)	321.8 ± 7.4	525.2 ± 7.4
Polydispersity	0.132 ± 0.031	0.314 ± 0.006
Zeta potential, ζ (mV)	-17.09 ± 0.25	-21.67 ± 1.5
% Loading efficiency	77.59	65.50
% Cumulative release	59.91	87.41

6.3.2 Drug Loading Efficiency

Drug loading efficiency was determined by using indirect method because BSA is hydrophilic drug and can degrade in organic solvent. The loading efficiency was found to be 65.50% and 77.59% for BSA loaded porous and non-porous nanoparticles, respectively. The drug loading efficiency was sufficiently high which show the viability of those nanoparticles in controlled drug delivery systems. High loading efficiency is always wanted for an efficient drug delivery system so that less quantity of the particles would be needed to administer a particular dose. The non-porous nanoparticles had higher loading efficiency as compared to porous nanoparticles. The porous structures on the surface of nanospheres allowed some drug to

easily flow out whereas non-porous nanoparticles incorporated more drug [123]. The salt-leaching process, on one hand, caused the formation of porous structures on the nanoparticles surface but it also reduced the loading efficiency of the nanoparticles.

6.3.3 Drug Release Studies

To investigate the BSA drug release from porous and non-porous PLGA nanoparticles, BCA protein assay was used. The % cumulative BSA release for porous and non-porous PLGA nanoparticles was found to be 87.41% and 59.91% respectively, over a period of 30 days. For the first few days, more than 30% of BSA was released while after that, relatively less amount of BSA release was observed as shown in Figure 6.5. Release behavior of both types of nanoparticles is plotted to show the comparison over the same period of time.

Comparison of BSA release from the porous and non-porous PLGA nanoparticles showed a faster but sustained release from porous nanoparticles. Porous nanoparticles offered better release behavior owing to their increased surface area and better flow of fluid through leaky structures [226, 227]. Generally, reports show that larger particles show lower drug release rate when compared to smaller particles because the length of diffusion pathway is higher for larger particles and drug concentration gradient is smaller [122]. Here, porous nanoparticles were larger in size but exhibited high release rate than smaller particles. This clearly stemmed from the porosity. As the porosity increased, the % cumulative drug release also increased [123]. Moreover drug release from porous particles would also depend on the pore characteristics and the nature of host guest interactions [228]. Therefore, this approach shows nanoparticles that are not only larger but also have higher release of drug. The rapid and cost-effective synthesis can be easily applied to other drug models.

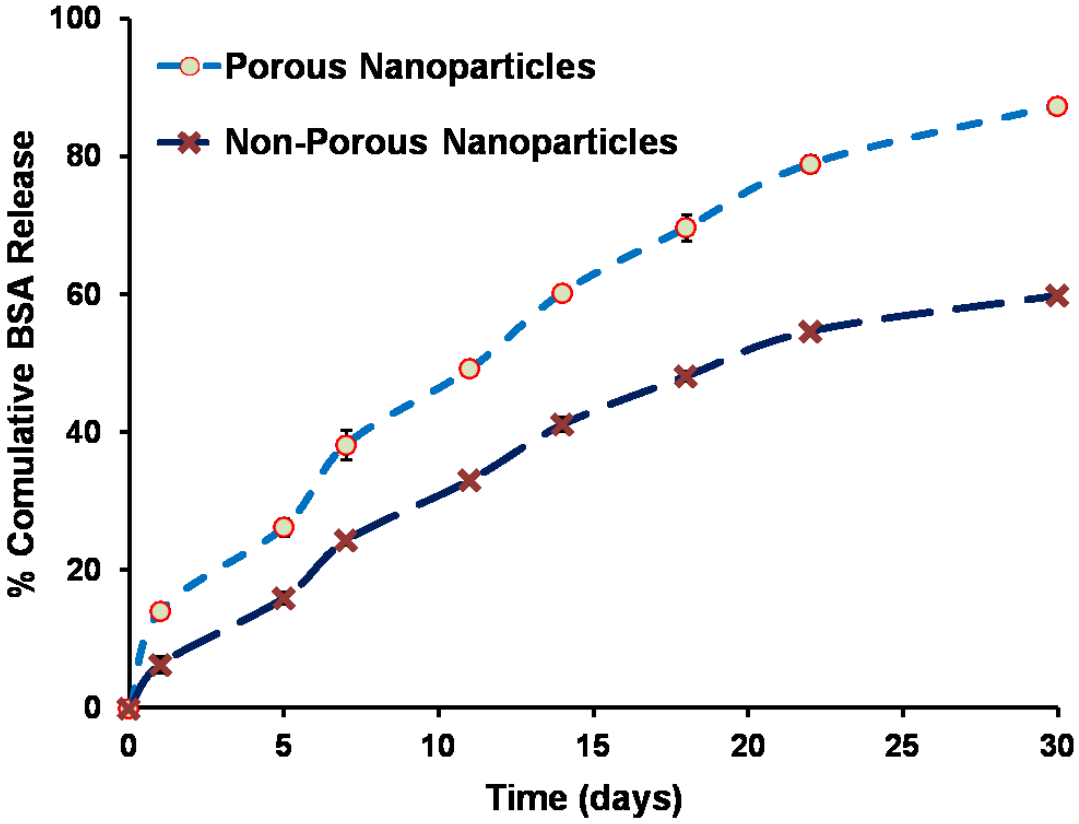

Figure 6.5 Comparison of drug release for BSA loaded Porous and non-porous PLGA nanoparticles demonstrate a better release behavior of porous nanoparticles. Error bars represent the standard deviation in the percentage protein release (n=3)

The drug release studies showed a sustained release which was reflected by a good amount of BSA up to 30 days. A burst release for the first few days was observed which stemmed from the release of drug adsorbed on or near to the surface of nanospheres and thus ensured immediate availability of therapeutic drug. Although the PLGA nanoparticles are employed for oral and intravenous drug delivery systems but essentially, PLGA nanoparticles are not selective to specific cells. These can be made more selective to certain cells using different functional groups, antibodies and aptamers. The aptamers and antibodies specifically bind the target cells and functionalized PLGA nanoparticles can be used for targeted drug

delivery where probing aptamers immobilized on the nanoparticles make them selective to the target cells [229, 230]. e-beam defined nanogaps.

6.4 Conclusion

This study demonstrates that BSA loaded porous PLGA nanoparticles provide sustained and controlled drug release. The salt-leaching is a novel technique to synthesize porous nanoparticles where sodium bicarbonate is used as the porogen. The physical characterization shows that porous nanoparticles are larger in size compared to the non-porous nanoparticles. Moreover, non-porous nanoparticles are very uniform in their size distribution but porous nanoparticles show a larger distribution over a specific range, due to the trapped salts that lead to the pore formation after salt-leaching. Drug loading efficiency of non-porous nanoparticles is calculated to be higher than that of porous nanoparticles which is due to easy release through the features on the porous nanoparticles. The drug release behavior of both types of nanoparticles is monitored over a period of 30 days and porous nanoparticles, although larger in sizes, show faster sustained release. Owing to the enhanced surface area, better release behavior and their stability over varying temperatures, porous nanoparticles are thus recognized as much better drug carriers.

CHAPTER 7

FUTURE RESEARCH DIRECTIONS

7.1 Introduction

In this chapter, scope of future research that would complement/supplement the current research work will be discussed. We will also incorporate the potential use of developed biosensors for various other applications.

7.2 Diagnosis of Bladder Cancer from Human Urine Samples

Though biopsied samples provide the best samples for cancer diagnosis but open surgical biopsy, image-guided biopsy or percutaneous biopsy all involve invasive approach for sample collection. It also affects patient's compliance. We plan to collect bladder cancer cells from the urine of bladder cancer patients. It is an absolutely non-invasive approach of collecting samples and lack of markers in urine sample makes it very difficult to diagnose bladder cancer by processing urine samples only. Since our device doesn't depend upon any biomarker but the purely intrinsic properties of a cell so can potentially be used to discriminate cancerous cells based upon their biomechanical properties. The urine samples from patients with and without bladder cancer will be evaluated with our device. The cells will be collected by centrifuging the urine sample at 1200 rpm for 15 minutes and cells will isolated in the form of a pellet at the bottom of the centrifuging tube. The cells will be resuspended in the NaCl solution (0.85% w/v) and will be processed with our micropore device as explained in Figure 7.1. Different types of cells will give different pulse signals while translocating through the micropore. The cancer cells will provide a distinctive pulse signal owing to its specific biomechanical composition. The distribution of pulses on a scatter plot should show clear data clusters which should not found in case of healthy patients. A representation of the prospective results is shown in Figure 7.2.

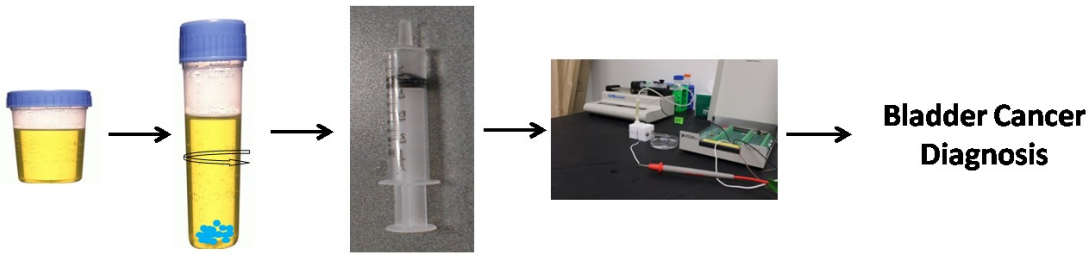

Figure 7.1 Shows the schematic representation of bladder cancer diagnosis from urine samples using our micropore based detection system

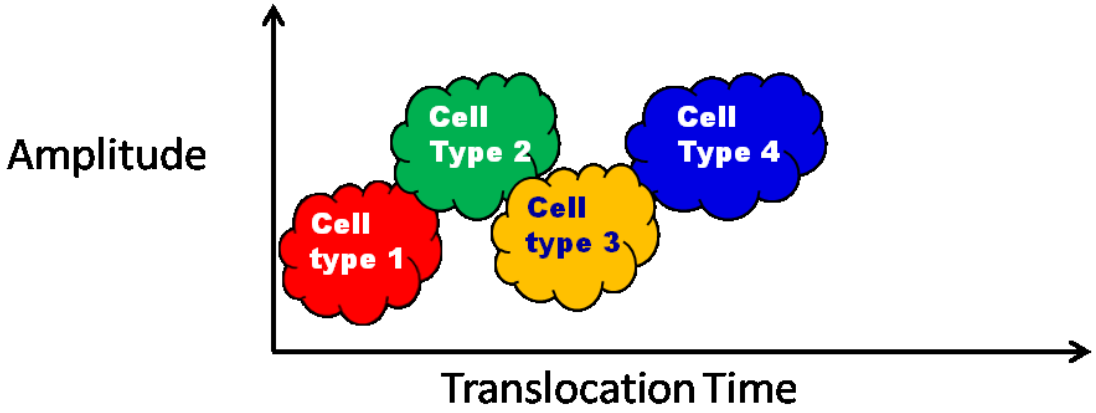

Figure 7.2 demonstrates the schematic sketch of the pulse distribution to show data clusters for different cells types. Cancer cells will give a characteristic pulse signal and particular data cluster will represent cancerous cells.

7.3 Enhanced Selectivity of Tumor Cells by Functionalizing the Micropore Periphery

The translocation profile (residence time, peak amplitude) of the translocating cell provide cell biophysical properties and is used for correlated determination of cancer cells. The methodology for screening cancerous cells from mixed cell suspension doesn't require chemical or dye-based labeling. Instead, cell sorting between normal and diseased cell types is based on the mechanical stiffness of the cells with the knowledge that the cancerous cells are more flexible than normal, healthy cells. As mentioned above, bladder cancer cells show a huge difference in their biophysical properties when compared to their normal counterpart so were

easily identifiable from healthy cells. Yet, the pulse distributions for cancerous and healthy cells may have some overlapped regions mainly due to size distribution of the cells. This may affect the sensitivity of the device. Since the translocation profile of the cells squeezed through the micropore varies significantly with the cell size so size variations among cells may lead to this possible concern. A large and soft cell might have the same translocation time as a small and rigid one. This scenario may lead to overlapped distributions, and result into wrong findings. To enhance the discrimination of cancerous cells by reducing the probability of overlapped regions in pulse distribution between cancerous and healthy cells, chemical modification of the micropore walls can be a direction for future research. Specific ligands for the receptors that over-express on cancer cell membranes (EGFR, prostate-specific membrane antigen, Urokinase plasminogen activator, etc.) [231-234] can be anchored to the inner periphery of the micropores for enhanced discrimination of cancerous cells from healthy ones as shown in Figure 7.3.

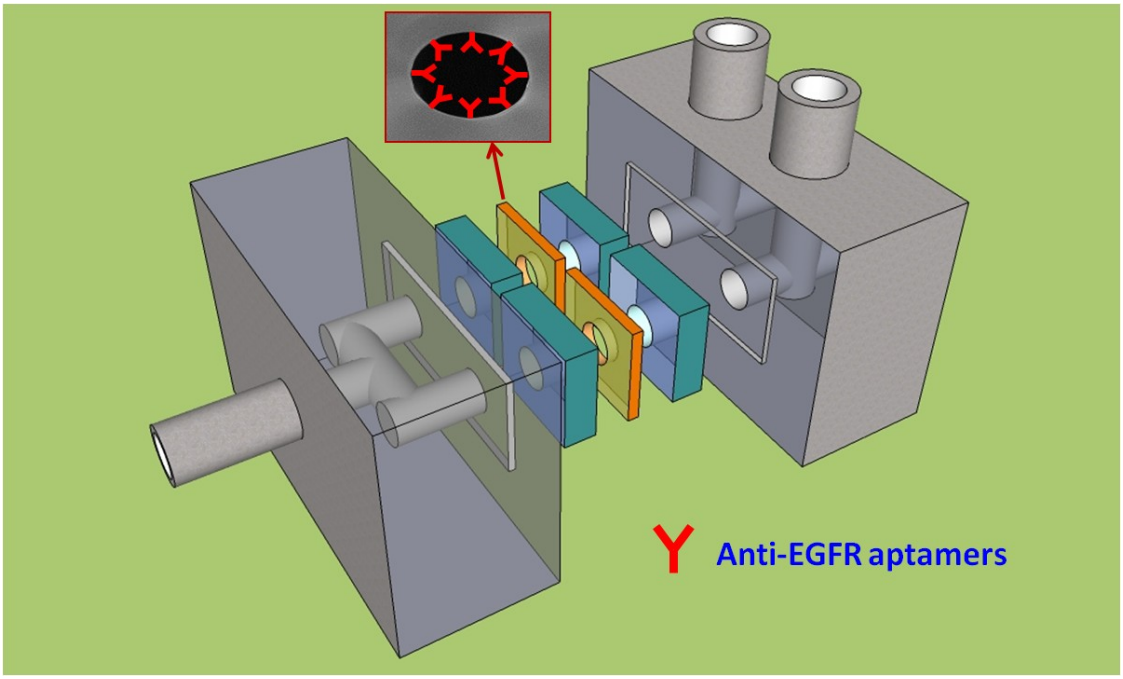

Figure 7.3 Schematic representation for system modificaiotn where the micropore is chemically activated with anti-EGFR aptamers for enhanced discrimination of cancer cells

These ligands will selectively bind to the cancerous cells, and thus can specifically slow down the passage of cells which exhibit overexpression. The retardations will lengthen translocation times, and result in the shift of the data cluster for cancer cells to make it completely isolated from other cell types. Thus, a combination of biomechanical and immunological sensing with functionalized micropores will provide a highly sensitive and selective system for electrophysiological analysis of cells for cancer diagnosis. The micropore walls can be chemically modified by immobilization of anti-EGFR aptamers which will selectively arrest the cells with EGFR overexpression on its membrane and will serve the purpose of selectively retarding the cancerous cells. Figure 7.4 shows the anticipated effect of chemically engineered micropore on cancer cell translocation behavior when compared to bare micropore. It would consequently shift the distribution of pulses for cancer cells and diminish the overlapped regions as illustrated in Figure 7.5. Hence, micropore functionalized with anti-EGFR aptamers might improve the discrimination of cancerous cells by making our micropore-bases biosensor selective to tumor cells.

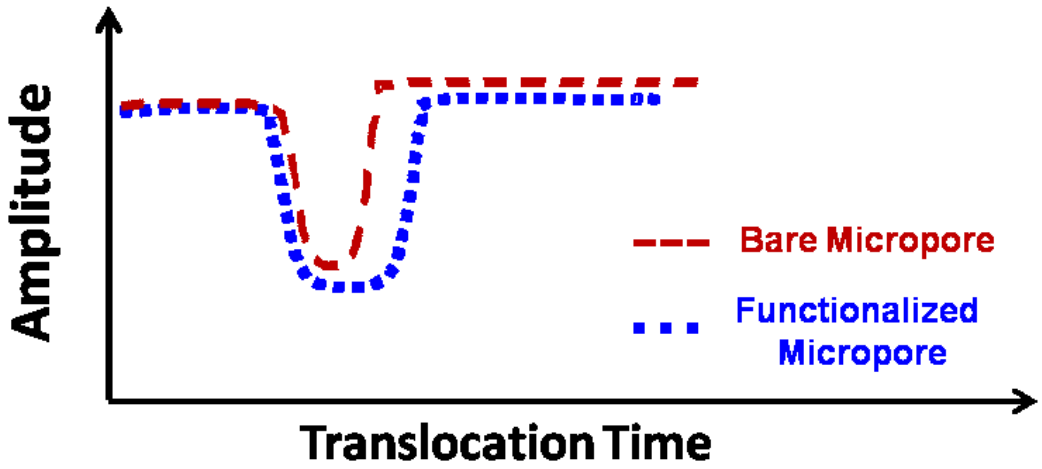

Figure 7.4 demonstrates the expected current-time trace comparison for cancer cells processed through similar sized bared micropore and chemically modified micropore. The solid-state micropore with anti-EGFR aptamers hold back the cancer cells and offer more hindrance to passage.

.

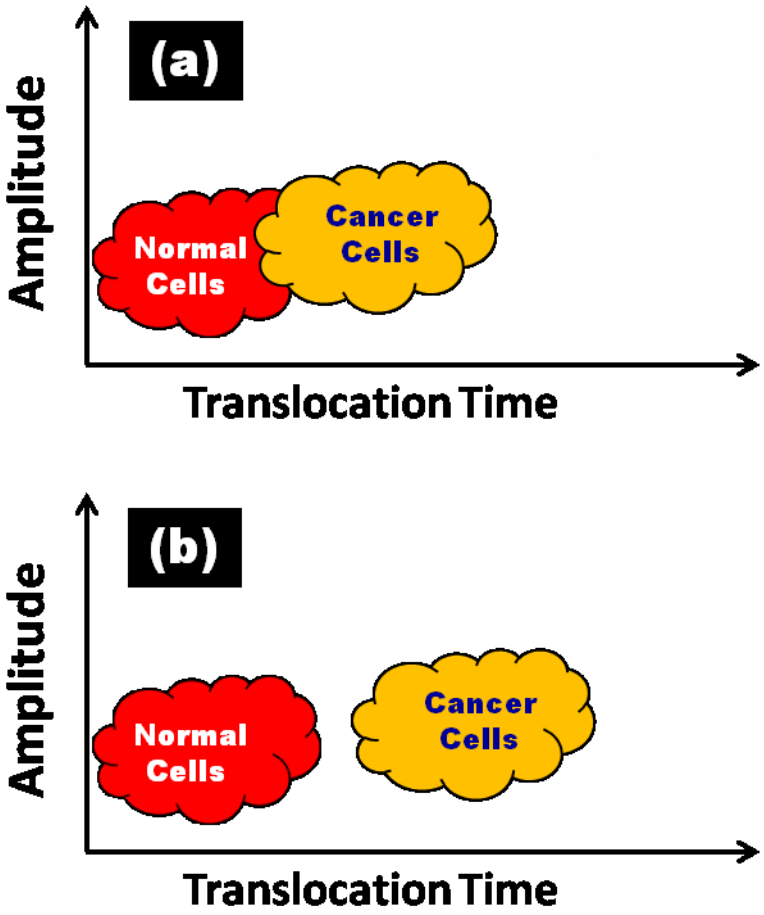

Figure 7.5 The distribution of pulses for normal cells and cancerous cells processed separately have been shown for (a) bare micropore (b) functionalized micropore. Selective arrest of cancer cells by anti-EGFR aptamers amplify the translocation time and shift the distribution of pulses toward higher translocation region which alleviates the cancer cell identificaiton

7.4 Metastatic vs Non-metastatic Tumor Cell Analysis

Cancer cells are known for rapid cell proliferation, tumor formation and invasion to surrounding cells. Cancer cells can migrate from the primary tumor to distant organs in the body and form a secondary tumor. This process of spreading the cancer cells to other body parts to grow a secondary tumor is called metastasis which is the major cause for deaths for cancer patients. Figure 7.6 shows a schematic representation for metastasis where tumor cells detach from primary tumor, enter the circulatory system and establish a metastatic colony.

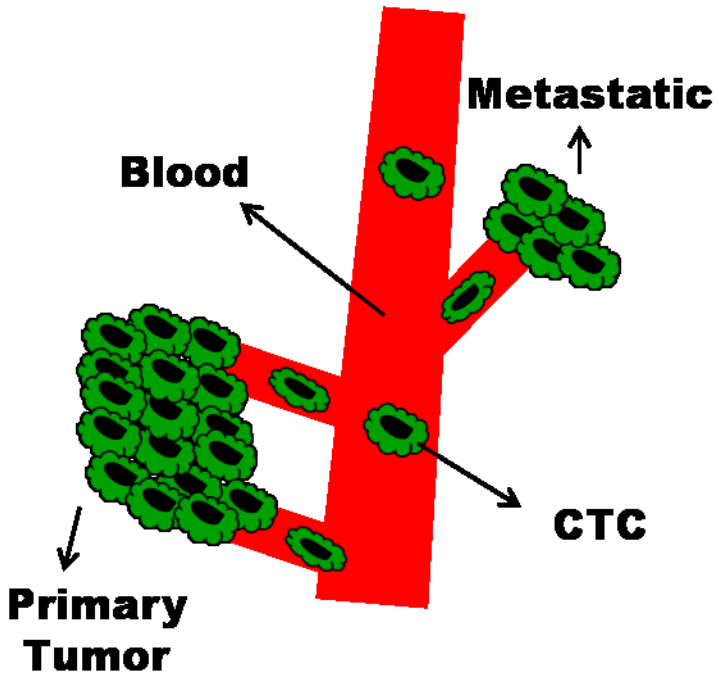

Figure 7.6 Schematics to represent the metastasis which involves shredding of primary tumor cells and establishment of a secondary tumor in distant body organ

Metastasis doesn't occur overnight but goes through a series of complex tumor-host interactions. The metastatic cancer cells have to diffuse through the surrounding tissues in order to enter the blood stream so that they move to other parts of the body to establish a metastatic colony. For this, they undergo several transformations including epithelial to mesenchymal cell transition (EMT). All these transformation make the metastatic tumor cells soft and flexible in order to facilitate them easy diffusion through tissues. Different studies have reported that metastatic cancer cells are much softer than primary (non-metastatic) cancer cells [30, 173]. Our micropore base sensor can discriminate between two cell types with different viscoelastic properties. Since metastatic cancer cells are more flexible so should offer much less impediment while passing through the micropore as compared to non-metastatic ones. Hence our solid-state based biosensor is potentially able to differentiate between metastatic and non-metastatic cancer cells. As mentioned above, metastatic cancer cells gradually transform

from stiffer to softer structure metastasis can be sensed beforehand by studying cell's tendency to get softer in nature by using our device. This would have a great impact in scientific community and can dramatically reduce the causalities of cancer patients.

7.5 High Frequency Multiplexer for Micropore Array Assembly

We have developed a micropore based detection scheme for simultaneous fingerprinting of cells passing through parallel micropores as explained in Chapter 5. The measuring setup involves a Labview algorithm to collect current samples and record it on the computer. The physical blockage of the micropore changes the ionic current flow across the micropore and current values are read by the National Instrument's data acquisition card (NI PXI 4071) which is pretty expensive part of the electrical setup. The developed multichannel micropore device has two channels where a dedicated data acquisition card (DAC) has been employed for each of the two parallel channels. In order to increase the number of channels for higher throughput, adding more cards would be much costly. We plan to develop a high frequency multiplexer which can help to record data from multiple channels using a single data acquisition card. Multiplexing is a method by which multiple analog or digital signals are combined into one signal over a shared medium. This phenomenon is commonly used in telecommunications.

A multiplexer (sometimes referred to as a MUX) is an electronic device that has several inputs and a single output. It selects the input signal at one of the input lines and transfers the selected signal to the output. The multiplexers are categorized depending upon the number of input lines like 2×1, 4×1, 8×1 and so on. A 4×1 multiplexer means it has four inputs and 1 output. The output from the multiplexer depends on the line that is selected. The frequency/speed at which the multiplexer can switch from one input line to the next is called the switching frequency/speed. Switching frequency, although neglected at times, plays an important role in determining the efficiency of a design. The higher the switching frequency, the faster the select line can switch from one input line to another.

The high frequency multiplexer will be appended to data acquisition card to make up a micropore array assembly. The information is collected in terms of rapidly changing electrical signals. A high frequency multiplexer can switch the input signal from one channel to the next and that particular selected channel information is collected and recorded at the output. In this way, information for all parallel channels will be collected at the output after regular intervals and will be recorded on computer in their respective files. Since the information is rapidly changing, the multiplexer should be able to quickly switch from one channel to the other (ideally 2.5 µsec) so that we do not miss any significant event. Such a high frequency multiplexer can find its applications in many other systems where simultaneous recording of data from multiple channels is desired. Figure 7.7 shows design of electrical setup that utilizes 4×1 multiplexer to increase the number of micropore channels quadruple.

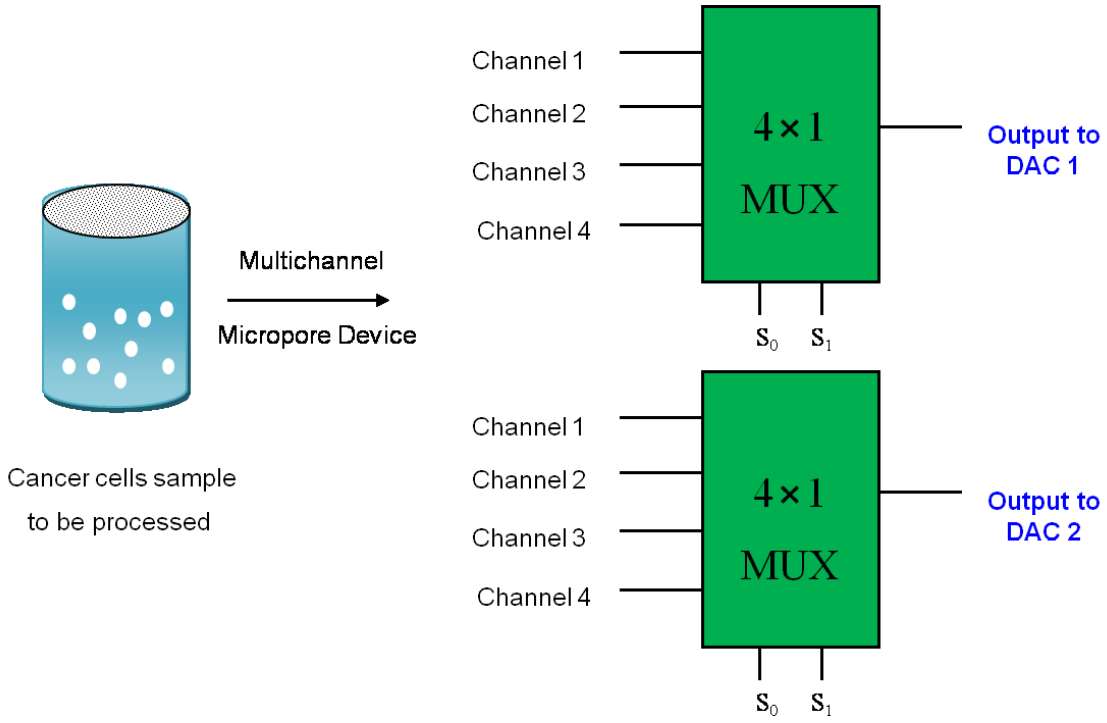

Figure 7.7 demonstrates the use of high speed multiplexer to increase the channels four times in the micropore array assembly

REFERENCES

[1] N. J. Tao, "Electron transport in molecular junctions," *Nature nanotechnology,* vol. 1, pp. 173-181, 2006.

[2] M. A. Reed, C. Zhou, C. J. Muller, T. P. Burgin, and J. M. Tour, "Conductance of a molecular junction," *Science,* vol. 278, pp. 252-254, 1997.

[3] F. Chen, J. Hihath, Z. Huang, X. Li, and N. J. Tao, "Measurement of single-molecule conductance," *Annu. Rev. Phys. Chem.,* vol. 58, pp. 535-564, 2007.

[4] M. A. Reed, C. Zhou, M. R. Deshpande, C. J. Muller, T. P. Burgin, L. Jones Ii, and J. M. Tour, "The electrical measurement of molecular junctions," *Annals of the New York Academy of Sciences,* vol. 852, pp. 133-144, 1998.

[5] T. Taychatanapat, K. I. Bolotin, F. Kuemmeth, and D. C. Ralph, "Imaging electromigration during the formation of break junctions," *Nano letters,* vol. 7, pp. 652-656, 2007.

[6] A. K. Mahapatro, S. Ghosh, and D. B. Janes, "Nanometer scale electrode separation (nanogap) using electromigration at room temperature," *Nanotechnology, IEEE Transactions on,* vol. 5, pp. 232-236, 2006.

[7] C. Zhou, C. J. Muller, M. R. Deshpande, J. W. Sleight, and M. A. Reed, "Microfabrication of a mechanically controllable break junction in silicon," *Applied physics letters,* vol. 67, p. 1160, 1995.

[8] S. M. Iqbal, G. Balasundaram, S. Ghosh, D. E. Bergstrom, and R. Bashir, "Direct current electrical characterization of ds-DNA in nanogap junctions," *Applied Physics Letters,* vol. 86, p. 153901, 2005.

[9] A. Bezryadin and C. Dekker, "Nanofabrication of electrodes with sub-5 nm spacing for transport experiments on single molecules and metal clusters," *Journal of Vacuum Science & Technology B: Microelectronics and Nanometer Structures,* vol. 15, p. 793, 1997.

[10] H. Park, A. K. L. Lim, A. P. Alivisatos, J. Park, and P. L. McEuen, "Fabrication of metallic electrodes with nanometer separation by electromigration," *Applied Physics Letters,* vol. 75, p. 301, 1999.

[11] R. Negishi, T. Hasegawa, K. Terabe, M. Aono, T. Ebihara, H. Tanaka, and T. Ogawa, "Fabrication of nanoscale gaps using a combination of self-assembled molecular and electron beam lithographic techniques," *Applied physics letters,* vol. 88, pp. 223111-223111-3, 2006.

[12] J. Choi, K. Lee, and D. B. Janes, "Nanometer scale gap made by conventional microscale fabrication: step junction," *Nano Letters,* vol. 4, pp. 1699-1703, 2004.

[13] P. P. Ramachandran, S. M. Christensen, and S. M. Iqbal, "Electronic detection of selective proteins using non antibody-based CMOS chip," in *IEEE/NIH Life Science Systems and Applications Workshop (LiSSA'09)*, Bethesda, MD, USA, 2009, pp. 1-4.

[14] D. H. J. Bunka and P. G. Stockley, "Aptamers come of age–at last," *Nature Reviews Microbiology,* vol. 4, pp. 588-596, 2006.

[15] R. Stoltenburg, C. Reinemann, and B. Strehlitz, "SELEX--a (r) evolutionary method to generate high-affinity nucleic acid ligands," *Biomolecular engineering,* vol. 24, pp. 381-403, 2007.

[16] S. Song, L. Wang, J. Li, C. Fan, and J. Zhao, "Aptamer-based biosensors," *TrAC Trends in Analytical Chemistry,* vol. 27, pp. 108-117, 2008.

[17] S. D. Jayasena, "Aptamers: an emerging class of molecules that rival antibodies in diagnostics," *Clinical chemistry,* vol. 45, pp. 1628-1650, 1999.

[18] Y. Xiao, A. A. Lubin, A. J. Heeger, and K. W. Plaxco, "Label-free electronic detection of thrombin in blood serum by using an aptamer-based sensor," *Angewandte Chemie,* vol. 44, pp. 5456-5459, 2005.

[19] S. Liu, X. Zhang, W. Luo, Z. Wang, X. Guo, M. L. Steigerwald, and X. Fang, "Single-Molecule Detection of Proteins Using Aptamer-Functionalized Molecular Electronic Devices," *Angewandte Chemie International Edition,* vol. 50, pp. 2496-2502, 2011.

[20] H. Lodish, A. Berk, C. A. Kaiser, M. Krieger, M. P. Scott, and P. Matsudaira, *Molecular cell biology*, 6th ed. New York: W.H. Freeman and Company, 2008.

[21] S.-C. Wu, C.-C. Liu, and W.-C. Lian, "Optimization of microcarrier cell culture process for the inactivated enterovirus type 71 vaccine development," *Vaccine,* vol. 22, pp. 3858-3864, 2004.

[22] J. Guck, S. Schinkinger, B. Lincoln, F. Wottawah, S. Ebert, M. Romeyke, D. Lenz, H. M. Erickson, R. Ananthakrishnan, and D. Mitchell, "Optical deformability as an inherent cell marker for testing malignant transformation and metastatic competence," *Biophysical journal,* vol. 88, pp. 3689-3698, 2005.

[23] P. A. Janmey, U. Euteneuer, P. Traub, and M. Schliwa, "Viscoelastic properties of vimentin compared with other filamentous biopolymer networks," *The Journal of cell biology,* vol. 113, pp. 155-160, 1991.

[24] A. Ben-Ze'ev, "The cytoskeleton in cancer cells," *Biochimica et Biophysica Acta (BBA)-Reviews on Cancer,* vol. 780, pp. 197-212, 1985.

[25] Y. Cheng, C. A. Hartemink, and J. H. Hartwig, "Three-dimensional reconstruction of the actin cytoskeleton from stereo images," *Journal of Biomechanics,* vol. 33, pp. 105-113, 2000.

[26] W. Bruening, J. Fontanarosa, K. Tipton, J. R. Treadwell, J. Launders, and K. Schoelles, "Systematic review: comparative effectiveness of core-needle and open surgical biopsy to diagnose breast lesions," *Annals of internal medicine,* vol. 152, pp. 238-246, 2010.

[27] J. B. Haun, C. M. Castro, R. Wang, V. M. Peterson, B. S. Marinelli, H. Lee, and R. Weissleder, "Micro-NMR for rapid molecular analysis of human tumor samples," *Science translational medicine,* vol. 3, p. 71ra16, 2011.

[28] L. Y. Joanne and J. W. Rak, "Inflammatory and immune cells in tumour angiogenesis and arteriogenesis," *Breast Cancer Res,* vol. 5, pp. 83-88, 2003.

[29] M. Lekka, P. Laidler, D. Gil, J. Lekki, Z. Stachura, and A. Z. Hrynkiewicz, "Elasticity of normal and cancerous human bladder cells studied by scanning force microscopy," *European Biophysics Journal,* vol. 28, pp. 312-316, 1999.

[30] J. B. Wyckoff, J. G. Jones, J. S. Condeelis, and J. E. Segall, "A critical step in metastasis: in vivo analysis of intravasation at the primary tumor," *Cancer research,* vol. 60, pp. 2504-2511, 2000.

[31] A. ul Haque, M. Zuberi, R. E. Diaz-Rivera, and D. Marshall Porterfield, "Electrical characterization of a single cell electroporation biochip with the 2-D scanning vibrating electrode technology," *Biomedical microdevices,* vol. 11, pp. 1239-1250, 2009.

[32] B. Matthews and J. W. Judy, "Design and fabrication of a micromachined planar patch-clamp substrate with integrated microfluidics for single-cell measurements," *Journal of Microelectromechanical Systems,* vol. 15, pp. 214-222, 2006.

[33] M. Kitta, H. Tanaka, and T. Kawai, "Rapid fabrication of Teflon micropores for artificial lipid bilayer formation," *Biosensors and Bioelectronics,* vol. 25, pp. 931-934, 2009.

[34] X. Niu and Z. Yan, "The expression of red blood cell deformability in micropore filtration tests," *Journal of Biomedical Engineering,* vol. 18, p. 615, 2001.

[35] H. Chang, A. Ikram, F. Kosari, G. Vasmatzis, A. Bhunia, and R. Bashir, "Electrical characterization of micro-organisms using microfabricated devices," *Journal of Vacuum Science & Technology B: Microelectronics and Nanometer Structures,* vol. 20, pp. 2058-2064, 2002.

[36] W. Asghar, Y. Wan, A. Ilyas, R. Bachoo, Y. Kim, and S. M. Iqbal, "Electrical fingerprinting, 3D profiling and detection of tumor cells with solid-state micropores," *Lab on a Chip,* vol. 12, pp. 2345-2352, 2012.

[37] E. Ogura, B. Kusumoputro, and T. Moriizumi, "Passage time measurement of individual and blood cells through arrayed micropores on Si_3N_4 membrane," *Journal of biomedical engineering,* vol. 13, pp. 503-506, 1991.
[38] R. Pantoja, J. M. Nagarah, D. M. Starace, N. A. Melosh, R. Blunck, F. Bezanilla, and J. R. Heath, "Silicon chip-based patch-clamp electrodes integrated with PDMS microfluidics," *Biosensors and Bioelectronics,* vol. 20, pp. 509-517, 2004.
[39] J. Li, M. Gershow, D. Stein, E. Brandin, and J. A. Golovchenko, "DNA molecules and configurations in a solid-state nanopore microscope," *Nature materials,* vol. 2, pp. 611-615, 2003.
[40] J. Li, D. Stein, C. McMullan, D. Branton, M. J. Aziz, and J. A. Golovchenko, "Ion-beam sculpting at nanometre length scales," *Nature,* vol. 412, pp. 166-169, 2001.
[41] H. Chang, S. M. Iqbal, E. A. Stach, A. H. King, N. J. Zaluzec, and R. Bashir, "Fabrication and characterization of solid-state nanopores using a field emission scanning electron microscope," *Applied physics letters,* vol. 88, pp. 103109-103109-3, 2006.
[42] A. J. Storm, J. H. Chen, X. S. Ling, H. W. Zandbergen, and C. Dekker, "Fabrication of solid-state nanopores with single-nanometre precision," *Nature materials,* vol. 2, pp. 537-540, 2003.
[43] M.-Y. Wu, D. Krapf, M. Zandbergen, H. Zandbergen, and P. E. Batson, "Formation of nanopores in a SiN/SiO membrane with an electron beam," *Applied Physics Letters,* vol. 87, p. 113106, 2005.
[44] J. T. L. Thong, W. K. Choi, and C. W. Chong, "TMAH etching of silicon and the interaction of etching parameters," *Sensors and Actuators A: Physical,* vol. 63, pp. 243-249, 1997.
[45] P.-H. Chen, H.-Y. Peng, C.-M. Hsieh, and M. K. Chyu, "The characteristic behavior of TMAH water solution for anisotropic etching on both Silicon substrate and SiO_2 layer," *Sensors and Actuators A: Physical,* vol. 93, pp. 132-137, 2001.
[46] K. B. Sundaram, A. Vijayakumar, and G. Subramanian, "Smooth etching of silicon using TMAH and isopropyl alcohol for MEMS applications," *Microelectronic Engineering,* vol. 77, pp. 230-241, 2005.
[47] I. Zubel and M. g. Kramkowska, "The effect of isopropyl alcohol on etching rate and roughness of (1 0 0) Si surface etched in KOH and TMAH solutions," *Sensors and Actuators A: Physical,* vol. 93, pp. 138-147, 2001.
[48] W. K. Choi, J. T. L. Thong, P. Luo, C. M. Tan, T. H. Chua, and Y. Bai, "Characterisation of pyramid formation arising from the TMAH etching of silicon," *Sensors and Actuators A: Physical,* vol. 71, pp. 238-243, 1998.
[49] M. Lopez-Lazaro, "A new view of carcinogenesis and an alternative approach to cancer therapy," *Molecular medicine,* vol. 16, pp. 144-153, 2010.
[50] M. Lopez-Lazaro, "The warburg effect: why and how do cancer cells activate glycolysis in the presence of oxygen?," *Anti-Cancer Agents in Medicinal Chemistry (Formerly Current Medicinal Chemistry-Anti-Cancer Agents),* vol. 8, pp. 305-312, 2008.
[51] P. Kovacic and J. D. Jacintho, "Mechanisms of carcinogenesis focus on oxidative stress and electron transfer," *Current medicinal chemistry,* vol. 8, pp. 773-796, 2001.
[52] R. W. Johnstone, A. A. Ruefli, and S. W. Lowe, "Apoptosis: a link between cancer genetics and chemotherapy," *Cell,* vol. 108, pp. 153-164, 2002.
[53] L. A. Liotta, M. L. Stracke, E. Kohn, S. Aznavoorian, and U. M. Wewer, "Tumor invasion and metastases: biochemical mechanisms," in *New Directions in Cancer Treatment*: Springer, 1989, pp. 381-398.
[54] L. Kopfstein and G. Christofori, "Metastasis: cell-autonomous mechanisms versus contributions by the tumor microenvironment," *Cellular and Molecular Life Sciences CMLS,* vol. 63, pp. 449-468, 2006.

[55] L. A. Liotta, "Tumor invasion and metastases--role of the extracellular matrix: Rhoads Memorial Award lecture," *Cancer Research,* vol. 46, pp. 1-7, 1986.
[56] J. J. Christiansen and A. K. Rajasekaran, "Reassessing epithelial to mesenchymal transition as a prerequisite for carcinoma invasion and metastasis," *Cancer research,* vol. 66, pp. 8319-8326, 2006.
[57] J. Yang, S. A. Mani, and R. A. Weinberg, "Exploring a new twist on tumor metastasis," *Cancer research,* vol. 66, pp. 4549-4552, 2006.
[58] M. Cristofanilli, D. F. Hayes, G. T. Budd, M. J. Ellis, A. Stopeck, J. M. Reuben, G. V. Doyle, J. Matera, W. J. Allard, and M. C. Miller, "Circulating tumor cells: a novel prognostic factor for newly diagnosed metastatic breast cancer," *Journal of Clinical Oncology,* vol. 23, pp. 1420-1430, 2005.
[59] T. R. Ashworth, "A case of cancer in which cells similar to those in the tumours were seen in the blood after death," *Aust Med J,* vol. 14, pp. 146-149, 1869.
[60] R. W. Carey, P. D. Taft, J. M. Bennett, and S. Kaufman, "Carcinocythemia (carcinoma cell leukemia): An acute leukemia-like picture due to metastatic carcinoma cells," *The American journal of medicine,* vol. 60, pp. 273-278, 1976.
[61] M. Cristofanilli, G. T. Budd, M. J. Ellis, A. Stopeck, J. Matera, M. C. Miller, J. M. Reuben, G. V. Doyle, W. J. Allard, and L. W. M. M. Terstappen, "Circulating tumor cells, disease progression, and survival in metastatic breast cancer," *New England Journal of Medicine,* vol. 351, pp. 781-791, 2004.
[62] G. T. Budd, M. Cristofanilli, M. J. Ellis, A. Stopeck, E. Borden, M. C. Miller, J. Matera, M. Repollet, G. V. Doyle, and L. W. M. M. Terstappen, "Circulating tumor cells versus imaging-predicting overall survival in metastatic breast cancer," *Clinical cancer research,* vol. 12, pp. 6403-6409, 2006.
[63] S. Riethdorf, H. Fritsche, V. MÃ¼ller, T. Rau, C. Schindlbeck, B. Rack, W. Janni, C. Coith, K. Beck, and F. JÃ¤nicke, "Detection of circulating tumor cells in peripheral blood of patients with metastatic breast cancer: a validation study of the CellSearch system," *Clinical cancer research,* vol. 13, pp. 920-928, 2007.
[64] D. F. Hayes, M. Cristofanilli, G. T. Budd, M. J. Ellis, A. Stopeck, M. C. Miller, J. Matera, W. J. Allard, G. V. Doyle, and L. W. W. M. Terstappen, "Circulating tumor cells at each follow-up time point during therapy of metastatic breast cancer patients predict progression-free and overall survival," *Clinical Cancer Research,* vol. 12, pp. 4218-4224, 2006.
[65] J. S. De Bono, H. I. Scher, R. B. Montgomery, C. Parker, M. C. Miller, H. Tissing, G. V. Doyle, L. W. W. M. Terstappen, K. J. Pienta, and D. Raghavan, "Circulating tumor cells predict survival benefit from treatment in metastatic castration-resistant prostate cancer," *Clinical Cancer Research,* vol. 14, pp. 6302-6309, 2008.
[66] D. Olmos, H. T. Arkenau, J. E. Ang, I. Ledaki, G. Attard, C. P. Carden, A. H. M. Reid, R. A'Hern, P. C. Fong, and N. B. Oomen, "Circulating tumour cell (CTC) counts as intermediate end points in castration-resistant prostate cancer (CRPC): a single-centre experience," *Annals of oncology,* vol. 20, p. 27, 2009.
[67] S. J. Cohen, C. J. A. Punt, N. Iannotti, B. H. Saidman, K. D. Sabbath, N. Y. Gabrail, J. Picus, M. Morse, E. Mitchell, and M. C. Miller, "Relationship of circulating tumor cells to tumor response, progression-free survival, and overall survival in patients with metastatic colorectal cancer," *Journal of clinical oncology,* vol. 26, pp. 3213-3221, 2008.
[68] J. Tol, M. Koopman, M. C. Miller, A. Tibbe, A. Cats, G. J. M. Creemers, A. H. Vos, I. D. Nagtegaal, L. Terstappen, and C. J. A. Punt, "Circulating tumour cells early predict progression-free and overall survival in advanced colorectal cancer patients treated with chemotherapy and targeted agents," *Annals of Oncology,* vol. 21, p. 1006, 2010.
[69] P. Paterlini-Brechot and N. L. Benali, "Circulating tumor cells (CTC) detection: clinical impact and future directions," *Cancer letters,* vol. 253, pp. 180-204, 2007.

[70] R. A. Ghossein, S. Bhattacharya, and J. Rosai, "Molecular detection of micrometastases and circulating tumor cells in solid tumors," *Clinical cancer research,* vol. 5, pp. 1950-1960, 1999.
[71] H. Zhou, J.-M. Guo, Y.-R. Lou, X.-J. Zhang, F.-D. Zhong, Z. Jiang, J. Cheng, and B.-X. Xiao, "Detection of circulating tumor cells in peripheral blood from patients with gastric cancer using microRNA as a marker," *Journal of Molecular Medicine,* vol. 88, pp. 709-717, 2010.
[72] P. A. Futreal, L. Coin, M. Marshall, T. Down, T. Hubbard, R. Wooster, N. Rahman, and M. R. Stratton, "A census of human cancer genes," *Nature Reviews Cancer,* vol. 4, pp. 177-183, 2004.
[73] M. Yu, S. Stott, M. Toner, S. Maheswaran, and D. A. Haber, "Circulating tumor cells: approaches to isolation and characterization," *The Journal of cell biology,* vol. 192, pp. 373-382, 2011.
[74] H. J. Kahn, A. Presta, L. Y. Yang, J. Blondal, M. Trudeau, L. Lickley, C. Holloway, D. R. McCready, D. Maclean, and A. Marks, "Enumeration of circulating tumor cells in the blood of breast cancer patients after filtration enrichment: correlation with disease stage," *Breast cancer research and treatment,* vol. 86, pp. 237-247, 2004.
[75] T. J. Pelkey, H. F. Frierson Jr, and D. E. Bruns, "Molecular and immunological detection of circulating tumor cells and micrometastases from solid tumors," *Clinical chemistry,* vol. 42, p. 1369, 1996.
[76] A. Rolle, R. Günzel, U. Pachmann, B. Willen, K. Höffken, and K. Pachmann, "Increase in number of circulating disseminated epithelial cells after surgery for non-small cell lung cancer monitored by MAINTRAC® is a predictor for relapse: a preliminary report," *World Journal of Surgical Oncology,* vol. 3, p. 18, 2005.
[77] V. Zieglschmid, C. Hollmann, and O. Böcher, "Detection of disseminated tumor cells in peripheral blood," *Critical Reviews in Clinical Laboratory Sciences,* vol. 42, pp. 155-196, 2005.
[78] R. T. Krivacic, A. Ladanyi, D. N. Curry, H. B. Hsieh, P. Kuhn, D. E. Bergsrud, J. F. Kepros, T. Barbera, M. Y. Ho, and L. B. Chen, "A rare-cell detector for cancer," *Proceedings of the National Academy of Sciences of the United States of America,* vol. 101, p. 10501, 2004.
[79] E. Racila, D. Euhus, A. J. Weiss, C. Rao, J. McConnell, L. Terstappen, and J. W. Uhr, "Detection and characterization of carcinoma cells in the blood," *Proceedings of the National Academy of Sciences,* vol. 95, p. 4589, 1998.
[80] C. Alix-Panabieres, S. Riethdorf, and K. Pantel, "Circulating tumor cells and bone marrow micrometastasis," *Clinical cancer research,* vol. 14, pp. 5013-5021, 2008.
[81] M. Yu, S. Stott, M. Toner, S. Maheswaran, and D. A. Haber, "Circulating tumor cells: approaches to isolation and characterization," *The Journal of Cell Biology,* vol. 192, p. 373, 2011.
[82] J. E. Hardingham, D. Kotasek, B. Farmer, R. N. Butler, J. X. Mi, R. E. Sage, and A. Dobrovic, "Immunobead-PCR: a technique for the detection of circulating tumor cells using immunomagnetic beads and the polymerase chain reaction," *Cancer research,* vol. 53, p. 3455, 1993.
[83] T. E. Witzig, B. Bossy, T. Kimlinger, P. C. Roche, J. N. Ingle, C. Grant, J. Donohue, V. J. Suman, D. Harrington, and J. Torre-Bueno, "Detection of circulating cytokeratin-positive cells in the blood of breast cancer patients using immunomagnetic enrichment and digital microscopy," *Clinical cancer research,* vol. 8, pp. 1085-1091, 2002.
[84] L. R. Gauthier, C. Granotier, J. C. Soria, S. Faivre, V. Boige, E. Raymond, and F. D. Boussin, "Detection of circulating carcinoma cells by telomerase activity," *British journal of cancer,* vol. 84, p. 631, 2001.

[85] J. E. Hardingham, D. Kotasek, B. Farmer, R. N. Butler, J.-X. Mi, R. E. Sage, and A. Dobrovic, "Immunobead-PCR: a technique for the detection of circulating tumor cells using immunomagnetic beads and the polymerase chain reaction," *Cancer research,* vol. 53, pp. 3455-3458, 1993.

[86] W. J. Allard, J. Matera, M. C. Miller, M. Repollet, M. C. Connelly, C. Rao, A. G. J. Tibbe, J. W. Uhr, and L. W. M. M. Terstappen, "Tumor cells circulate in the peripheral blood of all major carcinomas but not in healthy subjects or patients with nonmalignant diseases," *Clinical Cancer Research,* vol. 10, pp. 6897-6904, 2004.

[87] S. Riethdorf, H. Fritsche, V. Muller, T. Rau, C. Schindlbeck, B. Rack, W. Janni, C. Coith, K. Beck, and F. Janicke, "Detection of circulating tumor cells in peripheral blood of patients with metastatic breast cancer: a validation study of the CellSearch system," *Clinical Cancer Research,* vol. 13, pp. 920-928, 2007.

[88] M. Balic, N. Dandachi, G. Hofmann, H. Samonigg, H. Loibner, A. Obwaller, A. van der Kooi, A. G. J. Tibbe, G. V. Doyle, and L. Terstappen, "Comparison of two methods for enumerating circulating tumor cells in carcinoma patients," *Cytometry Part B: Clinical Cytometry,* vol. 68, pp. 25-30, 2005.

[89] M. A. Nandedkar, J. Palazzo, S. L. Abbondanzo, J. Lasota, and M. Miettinen, "CD45 (leukocyte common antigen) immunoreactivity in metastatic undifferentiated and neuroendocrine carcinoma: a potential diagnostic pitfall," *Modern pathology: an official journal of the United States and Canadian Academy of Pathology, Inc,* vol. 11, p. 1204, 1998.

[90] V. Zieglschmid, C. Hollmann, and O. BÃ¶cher, "Detection of disseminated tumor cells in peripheral blood," *Critical reviews in clinical laboratory sciences,* vol. 42, pp. 155-196, 2005.

[91] F. Schuler and G. Dolken, "Detection and monitoring of minimal residual disease by quantitative real-time PCR," *Clinica chimica acta,* vol. 363, pp. 147-156, 2006.

[92] L. Zabaglo, M. G. Ormerod, M. Parton, A. Ring, I. E. Smith, and M. Dowsett, "Cell filtration-laser scanning cytometry for the characterisation of circulating breast cancer cells," *Cytometry Part A,* vol. 55, pp. 102-108, 2003.

[93] G. Vona, A. Sabile, M. Louha, V. Sitruk, S. Romana, K. Schutze, F. Capron, D. Franco, M. Pazzagli, and M. Vekemans, "Isolation by size of epithelial tumor cells: a new method for the immunomorphological and molecular characterization of circulating tumor cells," *The American journal of pathology,* vol. 156, pp. 57-63, 2000.

[94] S. Meng, D. Tripathy, E. P. Frenkel, S. Shete, E. Z. Naftalis, J. F. Huth, P. D. Beitsch, M. Leitch, S. Hoover, and D. Euhus, "Circulating tumor cells in patients with breast cancer dormancy," *Clinical cancer research,* vol. 10, pp. 8152-8162, 2004.

[95] S. Nagrath, L. V. Sequist, S. Maheswaran, D. W. Bell, D. Irimia, L. Ulkus, M. R. Smith, E. L. Kwak, S. Digumarthy, and A. Muzikansky, "Isolation of rare circulating tumour cells in cancer patients by microchip technology," *Nature,* vol. 450, pp. 1235-1239, 2007.

[96] L. Brannon-Peppas and J. O. Blanchette, "Nanoparticle and targeted systems for cancer therapy," *Advanced drug delivery reviews,* vol. 64, pp. 206-212, 2012.

[97] S.-S. Feng and S. Chien, "Chemotherapeutic engineering: application and further development of chemical engineering principles for chemotherapy of cancer and other diseases," *Chemical Engineering Science,* vol. 58, pp. 4087-4114, 2003.

[98] K. E. Uhrich, S. M. Cannizzaro, R. S. Langer, and K. M. Shakesheff, "Polymeric systems for controlled drug release," *Chemical Reviews,* vol. 99, pp. 3181-3198, 1999.

[99] C. S. Brazel and N. A. Peppas, "Temperature-and pH-sensitive hydrogels for controlled release of antithrombotic agents," in *MRS Proceedings*, 1994, pp. 211-216.

[100] X. Huang and C. S. Brazel, "On the importance and mechanisms of burst release in matrix-controlled drug delivery systems," *Journal of Controlled Release,* vol. 73, pp. 121-136, 2001.

[101] C. Gomez-Gaete, N. Tsapis, M. Besnard, A. Bochot, and E. Fattal, "Encapsulation of dexamethasone into biodegradable polymeric nanoparticles," *International journal of pharmaceutics,* vol. 331, pp. 153-159, 2007.
[102] A. Budhian, S. J. Siegel, and K. I. Winey, "Production of haloperidol-loaded PLGA nanoparticles for extended controlled drug release of haloperidol," *Journal of microencapsulation,* vol. 22, pp. 773-785, 2005.
[103] Q. Cheng, J. Feng, J. Chen, X. Zhu, and F. Li, "Brain transport of neurotoxin-I with PLA nanoparticles through intranasal administration in rats: a microdialysis study," *Biopharmaceutics & drug disposition,* vol. 29, pp. 431-439, 2008.
[104] L. Mu and S. S. Feng, "A novel controlled release formulation for the anticancer drug paclitaxel (Taxol): PLGA nanoparticles containing vitamin E TPGS," *Journal of controlled release,* vol. 86, pp. 33-48, 2003.
[105] L. E. van Vlerken, T. K. Vyas, and M. M. Amiji, "Poly (ethylene glycol)-modified nanocarriers for tumor-targeted and intracellular delivery," *Pharmaceutical research,* vol. 24, pp. 1405-1414, 2007.
[106] S.-S. Feng, "Nanoparticles of biodegradable polymers for new-concept chemotherapy," *Expert review of medical devices,* vol. 1, pp. 115-125, 2004.
[107] M. F. Zambaux, F. Bonneaux, R. Gref, E. Dellacherie, and C. Vigneron, "Preparation and characterization of protein C-loaded PLA nanoparticles," *Journal of controlled release,* vol. 60, pp. 179-188, 1999.
[108] J. Panyam and V. Labhasetwar, "Biodegradable nanoparticles for drug and gene delivery to cells and tissue," *Advanced drug delivery reviews,* vol. 55, pp. 329-347, 200.
[109] W. Tiyaboonchai, "Chitosan nanoparticles: a promising system for drug delivery," *Naresuan University Journal,* vol. 11, pp. 51-66, 2003.
[110] A. Kumari, S. K. Yadav, and S. C. Yadav, "Biodegradable polymeric nanoparticles based drug delivery systems," *Colloids and Surfaces B: Biointerfaces,* vol. 75, pp. 1-18, 2010.
[111] K. S. Soppimath, T. M. Aminabhavi, A. R. Kulkarni, and W. E. Rudzinski, "Biodegradable polymeric nanoparticles as drug delivery devices," *Journal of controlled release,* vol. 70, pp. 1-20, 2001.
[112] J. Panyam, W.-Z. Zhou, S. Prabha, S. K. Sahoo, and V. Labhasetwar, "Rapid endo-lysosomal escape of poly (DL-lactide-co-glycolide) nanoparticles: implications for drug and gene delivery," *The FASEB Journal,* vol. 16, pp. 1217-1226, 2002.
[113] L. Nobs, F. Buchegger, R. Gurny, and E. AllÃ©mann, "Poly (lactic acid) nanoparticles labeled with biologically active Neutravidinâ„¢ for active targeting," *European journal of pharmaceutics and biopharmaceutics,* vol. 58, pp. 483-490, 2004.
[114] D. K. Sahana, G. Mittal, V. Bhardwaj, and M. N. V. Kumar, "PLGA nanoparticles for oral delivery of hydrophobic drugs: Influence of organic solvent on nanoparticle formation and release behavior in vitro and in vivo using estradiol as a model drug," *Journal of pharmaceutical sciences,* vol. 97, pp. 1530-1542, 2008.
[115] J. M. Barichello, M. Morishita, K. Takayama, and T. Nagai, "Encapsulation of hydrophilic and lipophilic drugs in PLGA nanoparticles by the nanoprecipitation method," *Drug development and industrial pharmacy,* vol. 25, pp. 471-476, 1999.
[116] C. Pinto Reis, R. J. Neufeld, A. n. J. Ribeiro, and F. Veiga, "Nanoencapsulation I. Methods for preparation of drug-loaded polymeric nanoparticles," *Nanomedicine: Nanotechnology, Biology and Medicine,* vol. 2, pp. 8-21, 2006.
[117] L. Li and S. P. Schwendeman, "Mapping neutral microclimate pH in PLGA microspheres," *Journal of controlled release,* vol. 101, pp. 163-173, 2005.
[118] J. Siepmann, K. Elkharraz, F. Siepmann, and D. Klose, "How autocatalysis accelerates drug release from PLGA-based microparticles: a quantitative treatment," *Biomacromolecules,* vol. 6, pp. 2312-2319, 2005.

[119] L. Fan and S. K. Singh, *Controlled release: A quantitative treatment*: Springer-Verlag Berlin, 1989.
[120] J. Heeren, T. Grewal, A. Laatsch, D. Rottke, F. Rinninger, R. K. Murray, D. K. Granner, P. A. Mayes, and V. W. Rodwell, "POROUS NANOPARTICLES IN DRUG DELIVERY SYSTEMS," *Pak. J. Pharm. Sci,* vol. 19, pp. 155-158, 2006.
[121] D. L. French, D. A. Edwards, and R. W. Niven, "The influence of formulation on emission, deaggregation and deposition of dry powders for inhalation," *Journal of aerosol science,* vol. 27, pp. 769-783, 1996.
[122] D. Klose, F. Siepmann, K. Elkharraz, S. Krenzlin, and J. Siepmann, "How porosity and size affect the drug release mechanisms from PLGA-based microparticles," *International journal of pharmaceutics,* vol. 314, pp. 198-206, 2006.
[123] Y. J. Oh, J. Lee, J. Y. Seo, T. Rhim, S. H. Kim, H. J. Yoon, and K. Y. Lee, "Preparation of budesonide-loaded porous PLGA microparticles and their therapeutic efficacy in a murine asthma model," *Journal of Controlled Release,* vol. 150, pp. 56-62, 2011.
[124] J. A. Straub, D. E. Chickering, C. C. Church, B. Shah, T. Hanlon, and H. Bernstein, "Porous PLGA microparticles: AI-700, an intravenously administered ultrasound contrast agent for use in echocardiography," *Journal of controlled release,* vol. 108, pp. 21-32, 2005.
[125] G. Zhao, T. Ishizaka, H. Kasai, H. Oikawa, and H. Nakanishi, "Fabrication of unique porous polyimide nanoparticles using a reprecipitation method," *Chemistry of materials,* vol. 19, pp. 1901-1905, 2007.
[126] H. K. Kim, H. J. Chung, and T. G. Park, "Biodegradable polymeric microspheres with "open/closed" pores for sustained release of human growth hormone," *Journal of Controlled Release,* vol. 112, pp. 167-174, 2006.
[127] J. G. M. Klijn, P. Berns, P. I. M. Schmitz, and J. A. Foekens, "The clinical significance of epidermal growth factor receptor (EGF-R) in human breast cancer: a review on 5232 patients," *Endocrine reviews,* vol. 13, p. 3, 1992.
[128] T. J. Lynch, D. W. Bell, R. Sordella, S. Gurubhagavatula, R. A. Okimoto, B. W. Brannigan, P. L. Harris, S. M. Haserlat, J. G. Supko, and F. G. Haluska, "Activating mutations in the epidermal growth factor receptor underlying responsiveness of non-small-cell lung cancer to gefitinib," *The New England journal of medicine,* vol. 350, p. 2129, 2004.
[129] A. M. F. Kersemaekers, G. J. Fleuren, G. G. Kenter, L. Van den Broek, S. M. Uljee, J. Hermans, and M. J. Van de Vijver, "Oncogene alterations in carcinomas of the uterine cervix: overexpression of the epidermal growth factor receptor is associated with poor prognosis," *Clinical Cancer Research,* vol. 5, p. 577, 1999.
[130] K. Mellon, C. Wright, P. Kelly, C. H. Horne, and D. E. Neal, "Original Articles: Bladder Cancer: Long-Term Outcome Related to Epidermal Growth Factor Receptor Status in Bladder Cancer," *The Journal of urology,* vol. 153, pp. 919-925, 1995.
[131] S. Inada, T. Koto, K. Futami, S. Arima, and A. Iwashita, "Evaluation of malignancy and the prognosis of esophageal cancer based on an immunohistochemical study (p53, E-cadherin, epidermal growth factor receptor)," *Surgery today,* vol. 29, pp. 493-503, 1999.
[132] J. Fischer-Colbrie, A. Witt, H. Heinzl, P. Speiser, K. Czerwenka, P. Sevelda, and R. Zeillinger, "EGFR and steroid receptors in ovarian carcinoma: comparison with prognostic parameters and outcome of patients," *Anticancer research,* vol. 17, pp. 613-619, 1997.
[133] W. S. Dalton and S. H. Friend, "Cancer biomarkers--an invitation to the table," *Science,* vol. 312, pp. 1165-1168, 2006.
[134] D. Atkins, K. A. Reiffen, C. L. Tegtmeier, H. Winther, M. S. Bonato, and S. Storkel, "Immunohistochemical detection of EGFR in paraffin-embedded tumor tissues: variation

in staining intensity due to choice of fixative and storage time of tissue sections," *Journal of Histochemistry and Cytochemistry,* vol. 52, p. 893, 2004.

[135] G. Brockhoff, F. Hofstaedter, and R. Knuechel, "Flow cytometric detection and quantitation of the epidermal growth factor receptor in comparison to Scatchard analysis in human bladder carcinoma cell lines," *Cytometry Part A,* vol. 17, pp. 75-83, 1994.

[136] K. W. Lee, K. H. Hwang, C. S. Kim, K. Han, Y. B. Chung, J. S. Park, Y. M. Lee, and D. C. Moon, "Determination of Recombinant human epidermal growth factor (rhEGF) in a pharmaceutical formulation by high performance liquid chromatography with electrochemical detection," *Archives of Pharmacal Research,* vol. 24, pp. 355-359, 2001.

[137] S. Kippenberger, S. Loitsch, M. Guschel, J. Müller, Y. Knies, R. Kaufmann, and A. Bernd, "Mechanical stretch stimulates protein kinase B/Akt phosphorylation in epidermal cells via angiotensin II type 1 receptor and epidermal growth factor receptor," *Journal of Biological Chemistry,* vol. 280, p. 3060, 2005.

[138] Y. Sako, S. Minoghchi, and T. Yanagida, "Single-molecule imaging of EGFR signalling on the surface of living cells," *Nature cell biology,* vol. 2, pp. 168-172, 2000.

[139] A. Sorkin, M. McClure, F. Huang, and R. Carter, "Interaction of EGF receptor and grb2 in living cells visualized by fluorescence resonance energy transfer (FRET) microscopy," *Current Biology,* vol. 10, pp. 1395-1398, 2000.

[140] D. J. Wold and C. D. Frisbie, "Fabrication and Characterization of Metal- Molecule-Metal Junctions by Conducting Probe Atomic Force Microscopy," *J. Am. Chem. Soc,* vol. 123, pp. 5549-5556, 2001.

[141] J. G. Kushmerick, D. B. Holt, J. C. Yang, J. Naciri, M. H. Moore, and R. Shashidhar, "Metal-molecule contacts and charge transport across monomolecular layers: Measurement and theory," *Physical review letters,* vol. 89, p. 86802, 2002.

[142] S. Datta, W. Tian, S. Hong, R. Reifenberger, J. I. Henderson, and C. P. Kubiak, "Current-voltage characteristics of self-assembled monolayers by scanning tunneling microscopy," *Physical Review Letters,* vol. 79, pp. 2530-2533, 1997.

[143] K. Liu, P. Avouris, J. Bucchignano, R. Martel, S. Sun, and J. Michl, "Simple fabrication scheme for sub-10 nm electrode gaps using electron-beam lithography," *Applied Physics Letters,* vol. 80, p. 865, 2002.

[144] C. Z. Li, H. X. He, and N. J. Tao, "Quantized tunneling current in the metallic nanogaps formed by electrodeposition and etching," *Applied Physics Letters,* vol. 77, p. 3995, 2000.

[145] D. R. Strachan, D. E. Smith, D. E. Johnston, T. H. Park, M. J. Therien, D. A. Bonnell, and A. T. Johnson, "Controlled fabrication of nanogaps in ambient environment for molecular electronics," *Applied Physics Letters,* vol. 86, p. 043109, 2005.

[146] W. Asghar, P. P. Ramachandran, A. Adewumi, M. R. Noor, and S. M. Iqbal, "Rapid Nanomanufacturing of Metallic Break Junctions Using Focused Ion Beam Scratching and Electromigration," *Journal of Manufacturing Science and Engineering,* vol. 132, p. 030911, 2010.

[147] S. M. Christensen, P. P. Ramachandran, and S. M. Iqbal, "Electronic Detection of Selective Proteins using Non Antibody-Based CMOS Chip," *DNA,* vol. 10, p. 391.4.

[148] H. Zhang, Z. Wang, X. F. Li, and X. C. Le, "Ultrasensitive detection of proteins by amplification of affinity aptamers," *Angewandte Chemie,* vol. 118, pp. 1606-1610, 2006.

[149] H. Sasaki, H. Yukiue, K. Mizuno, A. Sekimura, A. Konishi, M. Yano, M. Kaji, M. Kiriyama, I. Fukai, and Y. Yamakawa, "Elevated serum epidermal growth factor receptor level is correlated with lymph node metastasis in lung cancer," *International Journal of Clinical Oncology,* vol. 8, pp. 79-82, 2003.

[150] W. P. Carney, M. Burrell, L. D. Morris, and P. J. Hamer, "Normal levels of serum EGFr and decreases in several cancers," in *Proceddings AACR vol. 43*, 2002.
[151] W. Asghar, P. P. Ramachandran, A. Adewumi, M. R. Noor, and S. M. Iqbal, "Rapid Nanomanufacturing of Metallic Break Junctions using Focused Ion Beam Scratching and Electromigration," *Journal of Manufacturing Science and Engineering,* vol. 132, p. 030911, 2010.
[152] A. D. Ellington and J. W. Szostak, "In vitro selection of RNA molecules that bind specific ligands," *Nature,* vol. 346, pp. 818-822, 1990.
[153] N. Li, J. N. Ebright, G. M. Stovall, X. Chen, H. H. Nguyen, A. Singh, A. Syrett, and A. D. Ellington, "Technical and biological issues relevant to cell typing with aptamers," *Journal of proteome research,* vol. 8, pp. 2438-2448, 2009.
[154] N. Li, H. H. Nguyen, M. Byrom, and A. D. Ellington, "Inhibition of cell proliferation by an anti-EGFR aptamer," *PLoS One,* vol. 6, p. e20299, 2011.
[155] W. Wang, T. Lee, and M. A. Reed, "Mechanism of electron conduction in self-assembled alkanethiol monolayer devices," *Physical Review B,* vol. 68, p. 35416, 2003.
[156] G. K. McMaster and G. G. Carmichael, "Analysis of single-and double-stranded nucleic acids on polyacrylamide and agarose gels by using glyoxal and acridine orange," *Proceedings of the National Academy of Sciences of the United States of America,* vol. 74, p. 4835, 1977.
[157] F. Traganos, Z. Darzynkiewicz, T. Sharpless, and M. R. Melamed, "Simultaneous staining of ribonucleic and deoxyribonucleic acids in unfixed cells using acridine orange in a flow cytofluorometric system," *Journal of Histochemistry and Cytochemistry,* vol. 25, p. 46, 1977.
[158] M. F. Lopez, K. Berggren, E. Chernokalskaya, A. Lazarev, M. Robinson, and W. F. Patton, "A comparison of silver stain and SYPRO Ruby Protein Gel Stain with respect to protein detection in two-dimensional gels and identification by peptide mass profiling," *Electrophoresis,* vol. 21, pp. 3673-3683, 2000.
[159] T. P. J. Garrett, N. M. McKern, M. Lou, T. C. Elleman, T. E. Adams, G. O. Lovrecz, H.-J. Zhu, F. Walker, M. J. Frenkel, P. A. Hoyne, R. N. Jorissen, E. C. Nice, A. W. Burgess, and C. W. Ward, "Crystal Structure of a Truncated Epidermal Growth Factor Receptor Extracellular Domain Bound to Transforming Growth Factor α," *Cell,* vol. 110, pp. 763-773, 09/20 2002.
[160] A. Ilyas, W. Asghar, J. A. Billo, E. A. Q. Syed, and S. M. Iqbal, "From Molecular Electronics to Proteonics: Break Junctions for Biomarker Detection," in *IEEE/NIH Life Science Systems and Applications Workshop (LiSSA'11)* Bethesda, MD, USA, 2011, pp. 79-82.
[161] B. J. Hicke and A. W. Stephens, "Escort aptamers: a delivery service for diagnosis and therapy," *Journal of Clinical Investigation,* vol. 106, pp. 923-928, 2000.
[162] Y. Wan, J. Tan, W. Asghar, Y.-t. Kim, Y. Liu, and S. M. Iqbal, "Velocity effect on aptamer-based circulating tumor cell isolation in microfluidic devices," *The Journal of Physical Chemistry B,* vol. 115, pp. 13891-13896, 2011.
[163] Y. Wan, Y. Kim, N. Li, S. K. Cho, R. Bachoo, A. D. Ellington, and S. M. Iqbal, "Surface-immobilized aptamers for cancer cell isolation and microscopic cytology," *Cancer research,* vol. 70, pp. 9371-9380, 2010.
[164] P. R. Nair and M. A. Alam, "Performance limits of nanobiosensors," *Appl. Phys. Lett.,* vol. 88, pp. 233120-3, 2006.
[165] R. G. Sheiman, C. Fey, M. McNicholas, and V. Raptopoulos, "Possible causes of inconclusive results on CT-guided thoracic and abdominal core biopsies," *AJR. American journal of roentgenology,* vol. 170, pp. 1603-1607, 1998.

[166] V. Jeevanandam, M. R. Treat, and K. A. Forde, "A comparison of direct brush cytology and biopsy in the diagnosis of colorectal cancer," *Gastrointestinal endoscopy,* vol. 33, pp. 370-371, 1987.
[167] J. Melrose, S. Smith, and P. Ghosh, "Histological and immunohistological studies on cartilage," in *Cartilage and Osteoarthritis*: Springer, 2004, pp. 39-63.
[168] E. L. Elson, "Cellular mechanics as an indicator of cytoskeletal structure and function," *Annual review of biophysics and biophysical chemistry,* vol. 17, pp. 397-430, 1988.
[169] H. Lodish, A. Berk, S. L. Zipursky, P. Matsudaira, D. Baltimore, and J. Darnell, *Molecular cell biology*, 4th ed. New York: W. H. Freeman, 1999.
[170] P. Janmey, "Cell membranes and the cytoskeleton," *Handbook of Biological Physics,* vol. 1, pp. 805-849, 1995.
[171] H. Yamaguchi and J. Condeelis, "Regulation of the actin cytoskeleton in cancer cell migration and invasion," *Biochimica et Biophysica Acta (BBA)-Molecular Cell Research,* vol. 1773, pp. 642-652, 2007.
[172] M. Yilmaz and G. Christofori, "EMT, the cytoskeleton, and cancer cell invasion," *Cancer and Metastasis Reviews,* vol. 28, pp. 15-33, 2009.
[173] K. A. Ward, W. I. Li, S. Zimmer, and T. Davis, "Viscoelastic properties of transformed cells: role in tumor cell progression and metastasis formation," *Biorheology,* vol. 28, p. 301, 1991.
[174] M. Radmacher, "Measuring the elastic properties of living cells by the atomic force microscope," *Methods in cell biology,* vol. 68, pp. 67-90, 2002.
[175] J. Sleep, D. Wilson, R. Simmons, and W. Gratzer, "Elasticity of the red cell membrane and its relation to hemolytic disorders: an optical tweezers study," *Biophysical journal,* vol. 77, pp. 3085-3095, 1999.
[176] O. Thoumine and A. Ott, "Comparison of the mechanical properties of normal and transformed fibroblasts," *Biorheology,* vol. 34, pp. 309-326, 1997.
[177] T. Kundu, J. Bereiter-Hahn, and I. Karl, "Cell property determination from the acoustic microscope generated voltage versus frequency curves," *Biophysical Journal,* vol. 78, pp. 2270-2279, 2000.
[178] W. Asghar, A. Ilyas, J. A. Billo, and S. M. Iqbal, "Shrinking of Solid-state Nanopores by Direct Thermal Heating," *Nanoscale research letters,* vol. 6, pp. 1-6, 2011.
[179] W. Asghar, A. Ilyas, R. R. Deshmukh, S. Sumitsawan, R. B. Timmons, and S. M. Iqbal, "Pulsed plasma polymerization for controlling shrinkage and surface composition of nanopores," *Nanotechnology,* vol. 22, p. 285304, 2011.
[180] J. B. Heng, A. Aksimentiev, C. Ho, P. Marks, Y. V. Grinkova, S. Sligar, K. Schulten, and G. Timp, "Stretching DNA using the electric field in a synthetic nanopore," *Nano letters,* vol. 5, pp. 1883-1888, 2005.
[181] L. G. Collste, M. Devonec, Z. Darzynkiewicz, F. Traganos, T. K. Sharpless, W. F. Whitmore, and M. R. Melamed, "Bladder cancer diagnosis by flow cytometry. Correlation between cell samples from biopsy and bladder irrigation fluid," *Cancer,* vol. 45, pp. 2389-2394, 1980.
[182] T. Tansatit, S. Sahaphong, S. Riengrojpitak, V. Viyanant, and P. Sobhon, "Immunolocalization of cytoskeletal components in the tegument of the 3-week-old juvenile and adult *Fasciola gigantica*," *Veterinary Parasitology,* vol. 135, pp. 269-278, 2006.
[183] P. Chen, J. Gu, E. Brandin, Y. R. Kim, Q. Wang, and D. Branton, "Probing single DNA molecule transport using fabricated nanopores," *Nano Letters,* vol. 4, pp. 2293-2298, 2004.
[184] E. C. Kohn and L. A. Liotta, "Molecular insights into cancer invasion: strategies for prevention and intervention," *Cancer Research,* vol. 55, pp. 1856-1862, 1995.

[185] S. Paget, "The distribution of secondary growths in cancer of the breast," *The Lancet,* vol. 133, pp. 571-573, 1889.
[186] L. W. Terstappen, C. Rao, S. Gross, and A. J. Weiss, "Peripheral blood tumor cell load reflects the clinical activity of the disease in patients with carcinoma of the breast," *International journal of oncology,* vol. 17, pp. 573-581, 2000.
[187] J.-C. Soria, L. Morat, C. Durdux, M. Housset, A. Cortez, R. Blaise, and L. Sabatier, "The molecular detection of circulating tumor cells in bladder cancer using telomerase activity," *The Journal of urology,* vol. 167, pp. 352-356, 2002.
[188] R. D. Loberg, Y. Fridman, B. A. Pienta, E. T. Keller, L. K. McCauley, R. S. Taichman, and K. J. Pienta, "Detection and isolation of circulating tumor cells in urologic cancers: a review," *Neoplasia (New York, NY),* vol. 6, p. 302, 2004.
[189] E. S. Lianidou and A. Markou, "Circulating tumor cells in breast cancer: detection systems, molecular characterization, and future challenges," *Clinical chemistry,* vol. 57, pp. 1242-1255, 2011.
[190] S. L. Stott, R. J. Lee, S. Nagrath, M. Yu, D. T. Miyamoto, L. Ulkus, E. J. Inserra, M. Ulman, S. Springer, and Z. Nakamura, "Isolation and characterization of circulating tumor cells from patients with localized and metastatic prostate cancer," *Science translational medicine,* vol. 2, pp. 25-23, 2010.
[191] H. J. Kahn, A. Presta, L.-Y. Yang, J. Blondal, M. Trudeau, L. Lickley, C. Holloway, D. R. McCready, D. Maclean, and A. Marks, "Enumeration of circulating tumor cells in the blood of breast cancer patients after filtration enrichment: correlation with disease stage," *Breast cancer research and treatment,* vol. 86, pp. 237-247, 2004.
[192] R. T. Krivacic, A. Ladanyi, D. N. Curry, H. B. Hsieh, P. Kuhn, D. E. Bergsrud, J. F. Kepros, T. Barbera, M. Y. Ho, and L. B. Chen, "A rare-cell detector for cancer," *Proceedings of the National Academy of Sciences of the United States of America,* vol. 101, pp. 10501-10504, 2004.
[193] A. Rolle, R. Gunzel, U. Pachmann, B. Willen, K. Hoffken, and K. Pachmann, "Increase in number of circulating disseminated epithelial cells after surgery for non-small cell lung cancer monitored by MAINTRAC® is a predictor for relapse: A preliminary report," *World journal of surgical oncology,* vol. 3, p. 18, 2005.
[194] G. Vona, A. Sabile, M. Louha, V. Sitruk, S. Romana, K. SchÃ¼tze, F. d. r. Capron, D. Franco, M. Pazzagli, and M. Vekemans, "Isolation by size of epithelial tumor cells: a new method for the immunomorphological and molecular characterization of circulating tumor cells," *The American journal of pathology,* vol. 156, pp. 57-63, 2000.
[195] A. Y. Fu, C. Spence, A. Scherer, F. H. Arnold, and S. R. Quake, "A microfabricated fluorescence-activated cell sorter," *Nature biotechnology,* vol. 17, pp. 1109-1111, 1999.
[196] A. A. Adams, P. I. Okagbare, J. Feng, M. L. Hupert, D. Patterson, J. GoÌˆttert, R. L. McCarley, D. Nikitopoulos, M. C. Murphy, and S. A. Soper, "Highly efficient circulating tumor cell isolation from whole blood and label-free enumeration using polymer-based microfluidics with an integrated conductivity sensor," *Journal of the American Chemical Society,* vol. 130, pp. 8633-8641, 2008.
[197] M. Balic, N. Dandachi, G. n. Hofmann, H. Samonigg, H. Loibner, A. Obwaller, A. van der Kooi, A. G. J. Tibbe, G. V. Doyle, and L. W. M. M. Terstappen, "Comparison of two methods for enumerating circulating tumor cells in carcinoma patients," *Cytometry Part B: Clinical Cytometry,* vol. 68, pp. 25-30, 2005.
[198] J. J. Storhoff, S. S. Marla, P. Bao, S. Hagenow, H. Mehta, A. Lucas, V. Garimella, T. Patno, W. Buckingham, and W. Cork, "Gold nanoparticle-based detection of genomic DNA targets on microarrays using a novel optical detection system," *Biosensors and Bioelectronics,* vol. 19, pp. 875-883, 2004.

[199] H. B. Hsieh, D. Marrinucci, K. Bethel, D. N. Curry, M. Humphrey, R. T. Krivacic, J. Kroener, L. Kroener, A. Ladanyi, and N. Lazarus, "High speed detection of circulating tumor cells," *Biosensors and Bioelectronics,* vol. 21, pp. 1893-1899, 2006.
[200] N. Watkins, B. M. Venkatesan, M. Toner, W. Rodriguez, and R. Bashir, "A robust electrical microcytometer with 3-dimensional hydrofocusing," *Lab on a Chip,* vol. 9, pp. 3177-3184, 2009.
[201] S. M. Iqbal, D. Akin, and R. Bashir, "Solid-state nanopore channels with DNA selectivity," *Nature nanotechnology,* vol. 2, pp. 243-248, 2007.
[202] K. Healy, B. Schiedt, and A. P. Morrison, "Solid-state nanopore technologies for nanopore-based DNA analysis," *Nanomedicine,* vol. 2, pp. 875-897, 2007.
[203] B. Matthews and J. W. Judy, "Design and fabrication of a micromachined planar patch-clamp substrate with integrated microfluidics for single-cell measurements," *Microelectromechanical Systems, Journal of,* vol. 15, pp. 214-222, 2006.
[204] A. ul Haque, M. Zuberi, R. E. Diaz-Rivera, and D. M. Porterfield, "Electrical characterization of a single cell electroporation biochip with the 2-D scanning vibrating electrode technology," *Biomedical microdevices,* vol. 11, pp. 1239-1250, 2009.
[205] I. Marin- Valencia, S. K. Cho, D. Rakheja, K. J. Hatanpaa, P. Kapur, T. Mashimo, A. Jindal, V. Vemireddy, L. B. Good, and J. Raisanen, "Glucose metabolism via the pentose phosphate pathway, glycolysis and Krebs cycle in an orthotopic mouse model of human brain tumors," *NMR in Biomedicine,* vol. 25, pp. 1177-1186.
[206] P. Chen, J. Gu, E. Brandin, Y.-R. Kim, Q. Wang, and D. Branton, "Probing single DNA molecule transport using fabricated nanopores," *Nano Letters,* vol. 4, pp. 2293-2298, 2004.
[207] Y. Parajo, I. d' Angelo, A. Horvath, T. Vantus, K. Gyorgy, A. Welle, M. Garcia-Fuentes, and M. J. Alonso, "PLGA: poloxamer blend micro-and nanoparticles as controlled release systems for synthetic proangiogenic factors," *European Journal of Pharmaceutical Sciences,* vol. 41, pp. 644-649, 2010.
[208] S. Gelperina, O. Maksimenko, A. Khalansky, L. Vanchugova, E. Shipulo, K. Abbasova, R. Berdiev, S. Wohlfart, N. Chepurnova, and J. Kreuter, "Drug delivery to the brain using surfactant-coated poly (lactide-co-glycolide) nanoparticles: influence of the formulation parameters," *European Journal of Pharmaceutics and Biopharmaceutics,* vol. 74, pp. 157-163, 2009.
[209] B. J. Boyd, "Past and future evolution in colloidal drug delivery systems," *Expert Opinion on Drug Delivery,* vol. 5, pp. 69-85, 2008.
[210] S. Bennis, C. Chapey, J. Robert, and P. Couvreur, "Enhanced cytotoxicity of doxorubicin encapsulated in polyisohexylcyanoacrylate nanospheres against multidrug-resistant tumour cells in culture," *European Journal of Cancer,* vol. 30, pp. 89-93, 1994.
[211] W. Asghar, M. Islam, A. S. Wadajkar, Y. Wan, A. Ilyas, K. T. Nguyen, and S. M. Iqbal, "PLGA Micro-and Nanoparticles Loaded Into Gelatin Scaffold for Controlled Drug Release," *Nanotechnology, IEEE Transactions on,* vol. 11, pp. 546-553, 2012.
[212] B. Magenheim and S. Benita, "Nanoparticle characterization: a comprehensive physicochemical approach," *STP Pharma Sci.,* vol. 4, pp. 221-241, 1991.
[213] R. Jalil and J. R. Nixon, "Biodegradable poly (lactic acid) and poly (lactide-co-glycolide) microcapsules: problems associated with preparative techniques and release properties," *Journal of microencapsulation,* vol. 7, pp. 297-325, 1990.
[214] D. H. Lewis, "Controlled release of bioactive agents from lactide/glycolide polymers," *Drugs and the pharmaceutical sciences,* vol. 45, pp. 1-41, 1990.
[215] D. Klose, F. Siepmann, K. Elkharraz, and J. Siepmann, "PLGA-based drug delivery systems: Importance of the type of drug and device geometry," *International journal of pharmaceutics,* vol. 354, pp. 95-103, 2008.

[216] J. M. Lu, X. Wang, C. Marin-Muller, H. Wang, P. H. Lin, Q. Yao, and C. Chen, "Current advances in research and clinical applications of PLGA-based nanotechnology," *Expert review of molecular diagnostics,* vol. 9, pp. 325-341, 2009.

[217] K. Pays, J. Giermanska-Kahn, B. Pouligny, J. Bibette, and F. Leal-Calderon, "Double emulsions: how does release occur?," *Journal of controlled release,* vol. 79, pp. 193-205, 2002.

[218] F. Tewes, E. Munnier, B. Antoon, L. Ngaboni Okassa, S. Cohen-Jonathan, H. Marchais, L. Douziech-Eyrolles, M. Souce, P. Dubois, and I. Chourpa, "Comparative study of doxorubicin-loaded poly (lactide-co-glycolide) nanoparticles prepared by single and double emulsion methods," *European journal of pharmaceutics and biopharmaceutics,* vol. 66, pp. 488-492, 2007.

[219] D. C. Carter and J. X. Ho, "Structure of serum albumin," *Advances in protein chemistry,* vol. 45, pp. 153-204, 1994.

[220] F. Boury, H. Marchais, J. E. Proust, and J. P. Benoit, "Bovine serum albumin release from poly (Î±-hydroxy acid) microspheres: effects of polymer molecular weight and surface properties," *Journal of controlled release,* vol. 45, pp. 75-86, 1997.

[221] F. He, R. X. Zhuo, L. J. Liu, D. B. Jin, J. Feng, and X. L. Wang, "Immobilized lipase on porous silica beads: preparation and application for enzymatic ring-opening polymerization of cyclic phosphate," *Reactive and Functional Polymers,* vol. 47, pp. 153-158, 2001.

[222] H. J. Chung, H. K. Kim, J. J. Yoon, and T. G. Park, "Heparin immobilized porous PLGA microspheres for angiogenic growth factor delivery," *Pharmaceutical research,* vol. 23, pp. 1835-1841, 2006.

[223] M. Nidhin, R. Indumathy, K. J. Sreeram, and B. U. Nair, "Synthesis of iron oxide nanoparticles of narrow size distribution on polysaccharide templates," *Bulletin of Materials Science,* vol. 31, pp. 93-96, 2008.

[224] P. Couvreur, G. Barratt, E. Fattal, P. Legrand, and C. Vauthier, "Nanocapsule technology: a review," *Critical reviews in therapeutic drug carrier systems,* vol. 19, pp. 99-134, 2002.

[225] K. Yoshioka, E. Sakai, M. Daimon, and A. Kitahara, "Role of steric hindrance in the performance of superplasticizers for concrete," *Journal of the American Ceramic Society,* vol. 80, pp. 2667-2671, 1997.

[226] J. F. Chen, H. M. Ding, J. X. Wang, and L. Shao, "Preparation and characterization of porous hollow silica nanoparticles for drug delivery application," *Biomaterials,* vol. 25, pp. 723-727, 2004.

[227] M. S. Arayne and N. Sultana, "Porous nanoparticles in drug delivery systems," *Pakistan journal of pharmaceutical sciences,* vol. 19, pp. 158-169, 2006.

[228] C. Y. Sun, C. Qin, C. G. Wang, Z. M. Su, S. Wang, X. L. Wang, G. S. Yang, K. Z. Shao, Y. Q. Lan, and E. B. Wang, "Chiral Nanoporous Metal-Organic Frameworks with High Porosity as Materials for Drug Delivery," *Advanced Materials,* vol. 23, pp. 5629-5632, 2011.

[229] J. Cheng, B. A. Teply, I. Sherifi, J. Sung, G. Luther, F. X. Gu, E. Levy-Nissenbaum, A. F. Radovic-Moreno, R. Langer, and O. C. Farokhzad, "Formulation of functionalized PLGA-PEG nanoparticles for in vivo targeted drug delivery," *Biomaterials,* vol. 28, pp. 869-876, 2007.

[230] S. Dhar, F. X. Gu, R. Langer, O. C. Farokhzad, and S. J. Lippard, "Targeted delivery of cisplatin to prostate cancer cells by aptamer functionalized Pt (IV) prodrug-PLGA-PEG nanoparticles," *Proceedings of the National Academy of Sciences,* vol. 105, pp. 17356-17361, 2008.

[231] P. J. Russell, S. Bennett, and P. Stricker, "Growth factor involvement in progression of prostate cancer," *Clinical Chemistry,* vol. 44, pp. 705-723, 1998.

[232] T. Schlomm, P. Kirstein, L. Iwers, B. Daniel, T. Steuber, J. Walz, F. H. K. Chun, A. Haese, J. Kollermann, and M. Graefen, "Clinical significance of epidermal growth factor receptor protein overexpression and gene copy number gains in prostate cancer," *Clinical Cancer Research,* vol. 13, p. 6579, 2007.
[233] S. E. Lupold, B. J. Hicke, Y. Lin, and D. S. Coffey, "Identification and Characterization of Nuclease-stabilized RNA Molecules That Bind Human Prostate Cancer Cells via the Prostate-specific Membrane Antigen 1." vol. 62: AACR, 2002, pp. 4029-4033.
[234] A. Ilyas, W. Asghar, P. B. Allen, H. Duhon, A. D. Ellington, and S. M. Iqbal, "Electrical detection of cancer biomarker using aptamers with nanogap break-junctions," *Nanotechnology,* vol. 23, p. 275502, 2012.

BIOGRAPHICAL INFORMATION

Azhar Ilyas was born in Haroonabad, Punjab, Pakistan in 1985. He received the Bachelor's degree in Electrical Engineering from University of Engineering and Technology, Lahore, Pakistan in September 2007. After completion of his degree, he joined Faculty of Engineering at University of Central Punjab Lahore as lecturer from 2007 to 2009. He moved to Arlington, Texas for his Ph.D. He is a doctoral candidate under the supervision of Dr. Samir M. Iqbal in the Department of Electrical Engineering at the University of Texas at Arlington (UT-Arlington), Texas, USA since September 2009. His research has focused on a number of research themes including break junctions, micropore, surface functionalization and nanoparticles. He was awarded with several prestigious fellowships, grants and awards. He was selected as the winner for "N. M. Stelmakh Award" for being the best graduate student researcher in EE department for 2013. He was also awarded *Charles Desoer LiSSA Attendance Grant* on selection of his work as the Best Paper presented at *5th IEEE/NIH 2011 Life Science Systems and Applications Workshop* on NIH campus at Bethesda, MD. He was also awarded "I-Engage Mentoring Fellowship" on approval of his proposal for mentoring an undergraduate student with his research work. He was also awarded CONTACT student travel grant for getting his research proposal selected for external funding. He has published more than 20 peer reviewed journal and conference publications. His areas of interest include nanoscale biosensors, solid-state micropores for cellular level diagnosis, silicon chip fabrication, VLSI device design, drug release systems, proteomics and molecular cell biology.